STUDY OF CARBON NANOTUBE BASED TERAHERTZ DETECTORS

By

Xianbo Yang

A THESIS

Submitted to
Michigan State University
in partial fulfillment of the requirements
for the degree of

MASTER OF SCIENCE

Electrical Engineering

2012

ABSTRACT

STUDY OF CARBNON NANOTUBE BASED
TERAHERTZ DETECTORS

BY

Xianbo Yang

Terahertz (0.3~10THz) technologies have been proven to be useful in many areas. There is significant push in miniaturization of THz systems and components especially detectors since they are the key components. However, low-cost large-area compatible detector fabrication is difficult to achieve.

In this thesis, a CNTs Schottky diode THz detector featured with low-cost large area compatibility is simulated and fabricated.

Simulations are carried out that considers critical parameters. To overcome huge impedance mismatch between antenna and CNT Schottky diode, multi-CNTs aligned devices were simulated and analyzed. The simulation results show that NEP of approximately 5.5pW/Hz$^{0.5}$ or better can be achieved.

For realizing low-cost large area processing of such device, organic polymer substrates were studied and down selected. Furthermore, an effective novel nano-fabrication process was first developed to avoid using e-beam lithography. Device critical gap sizes of 1μm or smaller have been demonstrated using this process.

Measurements results showed strong non-linear rectifying behavior and NEP of 61.3 and 111pW/Hz$^{0.5}$ at 18GHz and 1THz. Those can be decreased by using higher quality and optimized numbers of CNTs in a single device.

ACKNOWLEDGEMENTS

This thesis would not have been possible without the help and supports from lots of people; I would like to express my gratitude and appreciation to all of them.

First of all, I am heartily thankful to my advisor Dr. Prem Chahal for his academic advices, economical supports and moral encouragements from the beginning to the concluding of this subject, without his help and guidance, it is impossible to accomplish this work.

I am also grateful to Dr. Donnie Reinhard and Dr. Lixin Dong for providing me advises, materials and resources which helped me pass through many critical barriers during the research.

I also would like to express my thanks to Hongzhi Chen, Ruiguo Yang, Shannon Demlow and Collin Meierbachtol for providing advice and helping me with the device measurements.

It is also a pleasure to thank members of EM group especially our TESLA group: Jose Hejase , Kyoung Youl Park, Nophadon Wiwatcharagoses, Josh Meyer, for their supports and help.

I also offer my regards and blessings to all the people working related to ERC cleanroom for their support and understanding in completion of this work.

During the whole research time through my graduate study, my family and friends provides me huge economical support and heartful understanding upon my research life. It is their support and love help and encourage me to overcome difficulties and pass through every crucial moment. I would like to express my special thanks to all of them.

Table of Contents

LIST OF TABLES

LIST OF FIGURES

Chapter 1 Introduction

1. Terahertz

1.1. Properties and Applications

Electromagnetic waves whose frequencies fall into the 0.3~10THz spectrum region is called terahertz waves. This spectral region has also been called sub millimeter waves due to their wavelength ranging from 100 to 1mm.THz lies between infrared and microwave bands (Figure 1.1) [1]. However, although such EM waves' wavelengths are identical to those of microwaves, people often use the term terahertz in order to specify the researches and applications in THz time domain spectroscopy.

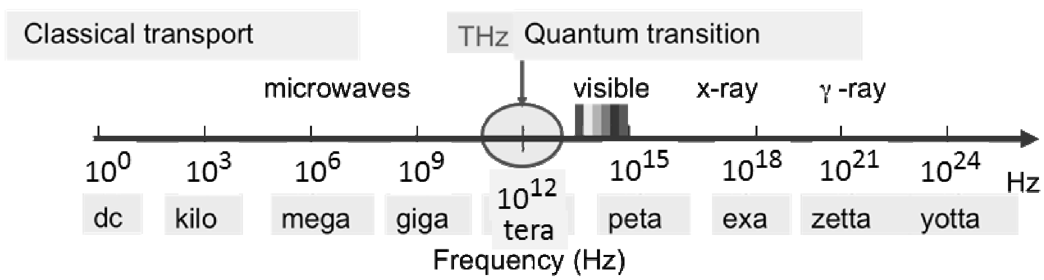

Figure 1.1 THz Lies between Infrared and Microwave bands

The earliest researches on THz can be dated back to the first two decades of 20^{th} century, people were trying to close the gap between infrared and electric wave (microwave). In that first development region of Terahertz, more than 1500 publications were published before 1975, and there were countless paper related to this topic in the next 25 years. The developments of digital computers which design for Fourier Transform and THz detectors even increase the number of publications [2].

Unlike its neighbor infrared and microwave, THz wave has many unique properties which also result in variety of applications. Those properties can be categorized as follow [3]:

(1) Penetration: THz waves can penetrate non-conducting thin layers such as clothes, paper, envelopes and regular packaging materials. However, it cannot travel a long distance as infrared and radio waves do in the air due to strong absorption by moisture.

(2) Spectroscopy: THz is part of the black body radiation, thus all the materials are giving off certain spectral of THz waves. Those THz waves vary due to the properties of different materials. So there is a positive signal showing that THz can be applied for material characterization.

(3) Short Wavelength: sub millimeter waves provide high resolution imaging sensing with lower scattering if using longer wavelength in THz region.

(4) Non Ionizing: The low power radiation of THz can stays around microwatts and is safer to use than X-rays, and finds applications in biomedical imaging and diagnostics.

Those unique properties of THz waves open a big window for researchers to study with and develop related applications:

(1) High resolution image sensing: the non-ionizing penetrating THz waves can be applied to medical imaging for detecting tumors and examining tissues in bodies while not destroying the normal ones, as shown in figure 1.2 (a) [4]. It also can be applied to “see through” the paintings to their underneath without destroy the surface.

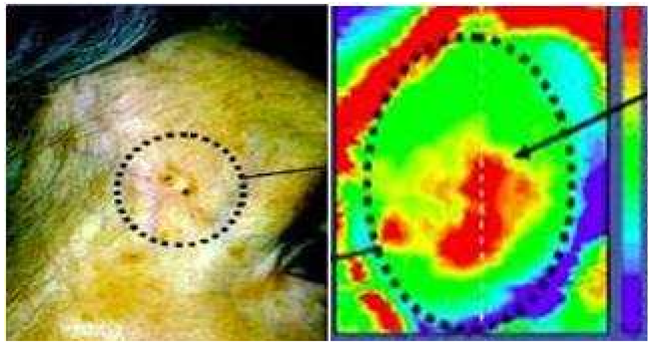

Figure 1.2 (a) Medical imaging of a tumor under the skin [4]

(b) Detecting a knife covered by the newspaper [4]

(2) Scientific spectroscopy: Researchers have already developed THz time domain spectroscopy to observe objects which are not transparent to visible light and infrared. It also can assist to obtain novel information in the realm of chemistry and biochemistry. Because many materials have different THz spectral features, securities are able to identify specific items deep in the luggage or covered by other materials, shown in figure 1.2 (b) [4]. Many materials (such as clothing) is transparent in THz spectral region, thus it is now implemented as body scanners.

(3) Communication: Although THz waves have high attenuation in air, one can apply it for telecommunication in the upper layer of atmosphere where there is low concentration of

scattering and absorption materials. One possibility is to apply THz communication between satellites in place of lasers when the satellites are not in direct line of contact. Furthermore, THz has been proposed for short range communications within a room between computers to carry information at high-bandwidth.

1.2. THz Sources and Detectors

1.2.1. THz Sources

Although THz waves lies between infrared and microwave bands, neither of these two source generators can easily be adapted for generation of THz waves. From optical side of view, most of the laser diodes are based on recombination of electron hole pairs in the semiconductor bandgap. For generating THz or even mid infrared waves, the direct bandgap approach for generation of THz is not practical as the bandgap required is too narrow for operation at room temperatures [5]. So a more practical approach is the down conversion of optical frequencies. From the other side, microwave point of view, it is possible to fabricate up to 1000GHz solid state generators through the use of multiplier chains. However, fabrication tolerances for THz operation are stringent and can be cost prohibitive. Before 2004, some of the laser devices were able to cover mid and far-infrared waves and go up to the edge of THz region, but for lower frequency, other techniques and devices are required.

Recently, researchers have found that the concepts of quantum cascades basing on semiconductor GaAs/AlGaAs heterojunction which uses for generating laser can be applied for generating THz waves. Unlike generating by recombination, quantum cascade devices generates photons through applying of intersubband transisions in repeated stack of one dimensional heterojunction thin layers, which can be refered as stack of quantum wells. When an electron excites one photon in the first layer, this photon immediately goes into the second layer and generates another photon. Typically there are 25 to 75 active heterojunction layers and each layer has a slightly lower energy than the one prior to it. Thus 25 to 75 photons can be generated for one electron. The quantum cascade can successfully operates between 1.9~4.8THz with the output power around 90mW. Current THz quantum cascade lasers operate at cyro-temperature and also produce very narrow spectral signals. Another high power THz generator is IMPATT diode, which is also a powerful solid state THz source [6]. This wide-bandgap 4H-SiC based double drift IMPATT diode can generate waves at low THz frequency region of ~ 0.7 THz, but the output power can reach up to 2.5×10^{11} Wm^{-2}.

Besides those semiconductor based solid direct state sources, researchers have also demonstrated the generation of THz signals through optical methods, such as Optically Pumped Terahertz Laser (OPTL). A carbon dioxide pump laser and a FIR gas cell are mounted in a laser resonating cavity. This device can create several discrete frequencies ranging from 300GHz to 10THz in time domain THz spectroscopy [3].

Another method to generate THz is coherent THz generation. Ultra short (10–200fs) visible laser or near infrared pulse is directly focused on the GaAs semiconductor THz source and the recombination of electron hole pairs generate THz pulse [5]. Moreover, instead of using optical excitation, electric field pulse with THz frequency can also be induced onto the semiconductor crystal surface for THz generation due to the second order nonlinear susceptibility [5].

Recently, the development of THz sources is focusing on the minimization of the devices operating with low power consumption. In mid-2007, researchers in Japan grew a novel crystal material having high temperature superconducting properties. Those crystal layers stack to perform the Josephson Effect: when voltage is applied across those junctions, a reverse current will flow in the opposite direction and create a THz frequency pulse on each layer. After finely tuning the thickness of each layer to achieve phase buildup, a uniform THz source is then achieved and the frequency can be tuned by the external bias [7]. The voltage required for this device can be provided by battery and is portable for everyday use.

Last year (2009), some researchers observed THz pulse around 2THz when peeling off the adhesive tapes. They claimed this is because of the trobocharging and the subsequent discharging effects [8].

1.2.2. THz Detectors

As discussed above, THz waves are easy to attenuate while travelling in air. It also tends to be scattered by the ambient molecules and thus limiting long distance propagation. Thus, high sensitivity THz detectors are under development in order to meet the need in scientific research, communications as well as homeland security. Detectors can be divided into direct detectors and indirect detectors (also called hetrodyne detectors). One of the key requirements of detectors is high sensitivity, in other words, low Noise equivalent Power (NEP) values are desirable. In direct detection approach, the phase information is lost and frequency can be measured through the use of filters. . On the other hand, indirect detectors are more applied for cosmic research for observing the background radiation of the universe. The THz wave’s frequency is down converted to intermediate frequency (IF) while preserving the amplitude and phase for higher resolution spectroscopy measurements. In some circumstance, direct THz detectors are used where sensitivity is more important in broadband region. Some common THz detection approaches are discussed below:

(1) Photoconductive THz detector

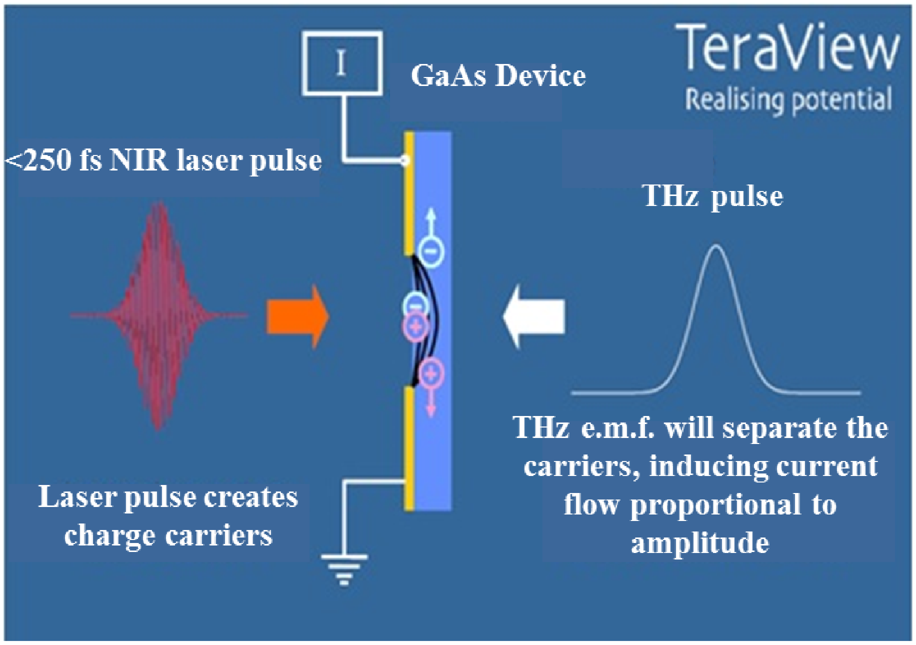

Figure 1.3 Schematic of photoconductive THz detector [9]

As shown in Figure 1.3, a photoconductive based THz detector is the most frequently used detector in THz time domain spectroscopy. . There are three key components associated with the functioning of this detector. First a short near field infrared laser pulse directly incidence on the low temperature grown GaAs based semiconductor device. Due to the excitation, electrons and holes pairs are created in the conduction and valence bands. THz pulse then is illuminated on the GaAs surface, separating the charge carriers, creating the current signal whose value is proportional the power of the THz pulse. Basically speaking, this method is the reverse way of generating THz pulse basing on the coherent THz generation. The time domain signal $I(\tau)$ can be defined by equation 1.1[10]. *E(t)* is the electric field of the THz pulse, *D(t)* is the detector response, τ is the delay time.

$$I(\tau)=\frac{1}{T}\int_0^T E(t)D(t-\tau)dt \qquad 1.1$$

Although its principles are easy to understand and operate, the setup of the whole system requires relatively large space due the existence of the laser generation system as well as optical components mounting and aligning.

(2) Thermal THz detectors

The thermal THz detector family consist a numbers of different detectors, including: bolometer, pyroelectric detector and Golay cell. The basic concept of THz detecting is by changing their resistance (bolometer) or bias voltage (pyroelectric detector) due to the absorption of incidence energy which is converted to heat. For example, a thin-film pyroelectric detector (figure 1.4), based on ferroelectric materials such as TGS or Lithium Tantalate, exhibits large electric polarization in the active crystal respective to the changing of temperature. It generates transient bias across high impedance crystal when THz waves impinges upon the detector and increases the temperature. Figure 1.5 shows that the voltage signal can be picked up by a FET and converted into digital signal. The sensitivity of such devices could vary according to the temperature of operation. In most of the case, pyroelectric detector are required to work around 4K in order to provide lower NEP, which is around 0.1pW/Hz$^{0.5}$. Even lower NEP ~ 10^{-13}W/Hz$^{0.5}$ for broadband can be achieved by continuing lowering the temperature to hundreds of mK. However, at room temperature it only shows low sensitivity with NEP value of approximately 10^{-9}W/Hz$^{0.5}$ [12]. What's more, most of these devices also require high quality materials which are expensive, thus the cost is another limitation for large area THz imaging for commercial market.

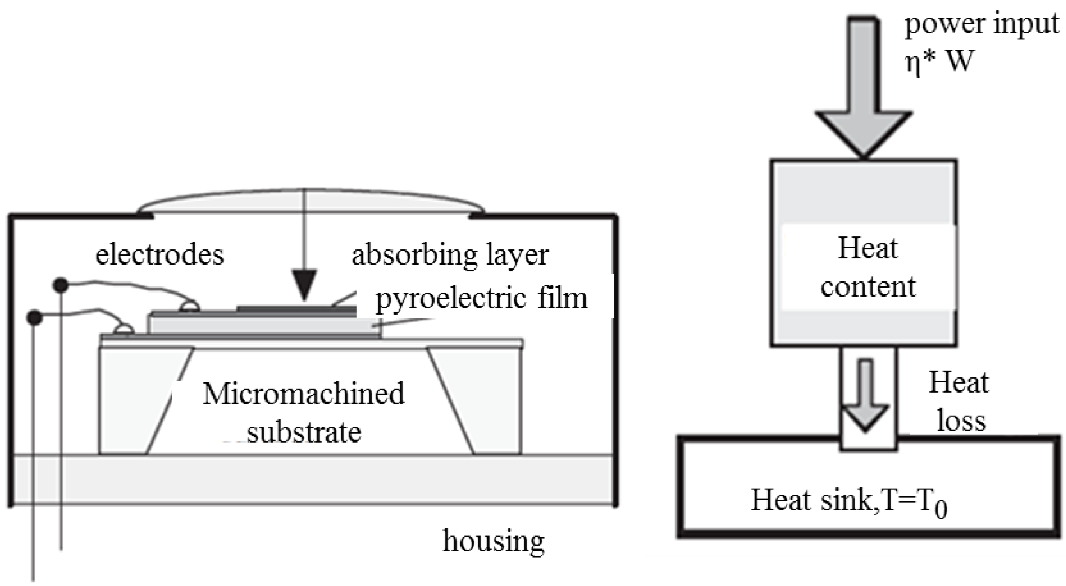

Figure 1.4 Strucutre of a thin-film pyroelectric detector (left) and thermal operation element (right) [11]

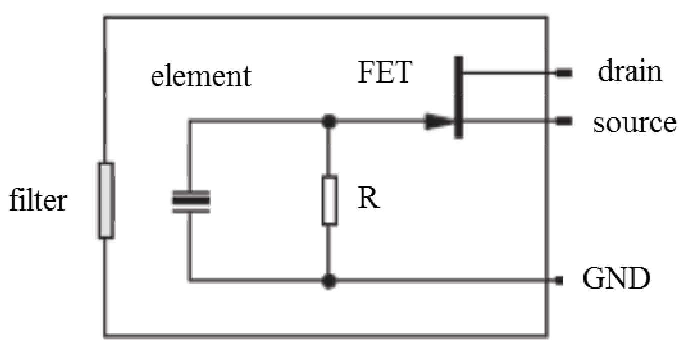

Figure 1.5 Schematic of pyroelectric THz detector setup circuit[12]

Like pyroelectric THz detectors, bolometers are also responded to the change in temperature of the film due to the absorption of THz radiation. The only difference is that these detectors show a change resistance variation instead of generation transient voltage due to absorption of THz radiation. The basic setup of the bolometer is shown in figure 1.6 [12]. The constant time can be calculated by

$$\tau = \frac{C}{G} \qquad 1.2$$

Where C is the heat capacity of the material, G is the thermal conductance from the material to the heat sink. The temperature difference between the absence and existence of THz can be derived from equation 1.3, where ΔP is the power delivered by the incident THz wave.

$$\Delta T = \frac{\Delta P}{G\sqrt{1+\omega^2 (C/G)^2}} \qquad 1.3$$

Equation 1.3 clearly shows that in order to obtain large temperature difference and shorter constant time, materials with small heat capacity and large thermal conductance are required. But there is a trade-off between sensitivity and response time for uncooled bolometer. In Ref. [10], for a 20ms constant time bolometer, the NEP is around 10^{-13}W/Hz$^{0.5}$, while if one wants to decrease the NEP to 10^{-19}W/Hz$^{0.5}$, the response time is around 3.5×10^{4}s. For a cooled bolometer, the response time and sensitivity can both be tuned at a certain low value. However, the low temperature limits its application to laboratory setups.

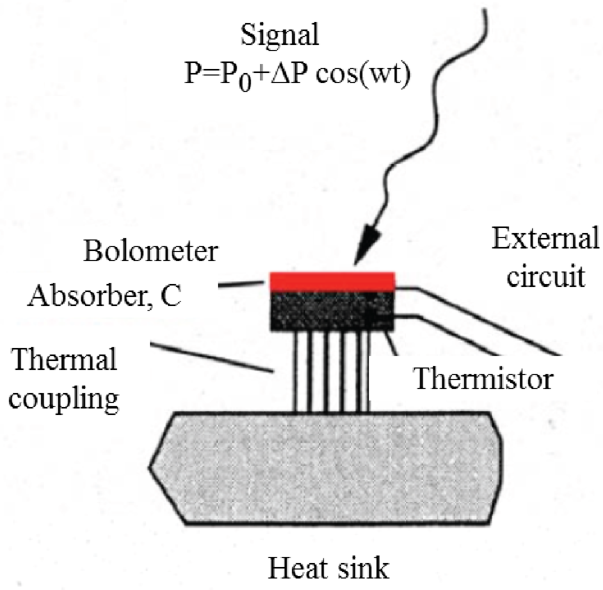

Figure 1.6 Schematic of a simple bolometer [12]

(3) Schottky Barrier Diode THz detector.

The Schottky barrier diodes are among the basic devices in THz technologies. The detection capability is based on its nonlinear I-V characteristics and the rectification behavior. Figure 1.7 shows a simple explanation of how it works respect to the inducing RF waves. The incoming RF signal is rectified and this signal is readout across a capacitor as a DC signal. The higher the sensitivity the higher the rectified signal for the input power. . Detailed calculations for the Schottky diode THz detector will be carried out in the Simulation part of Chapter 2. The most common used semiconductor material for planar Schottky diode detectors is GaAs. This is because there is a satisfying balance between carrier mobility and the bandgap, which are two core elements during the study of rectification mechanism. Other III-V materials are also being studied and show positive results as well. Diodes built using Si have low cut-off frequencies and thus not used in THz applications.

Apart from the semiconductor material, other challenges are that the device required to operate at THz frequencies need to have low parasitic. This requires devices that are small (< 1μm×1μm). Furthermore, for more practical applications in THz imaging and sensing, a large array (100×100 elements may be required) of detectors coupled with antenna elements is required. In most instances, a significant area is occupied by the antenna element on the wafer. With the use of III-V semiconductor technology, where the wafer size is significantly small compared to CMOS technology, only few detectors can be fabricated per wafer. Thus, it will be desirable to be able to develop a process that is large area compatible while meeting the needs for THz operation. Thus, new devices with novel materials and detecting mechanism are under development.

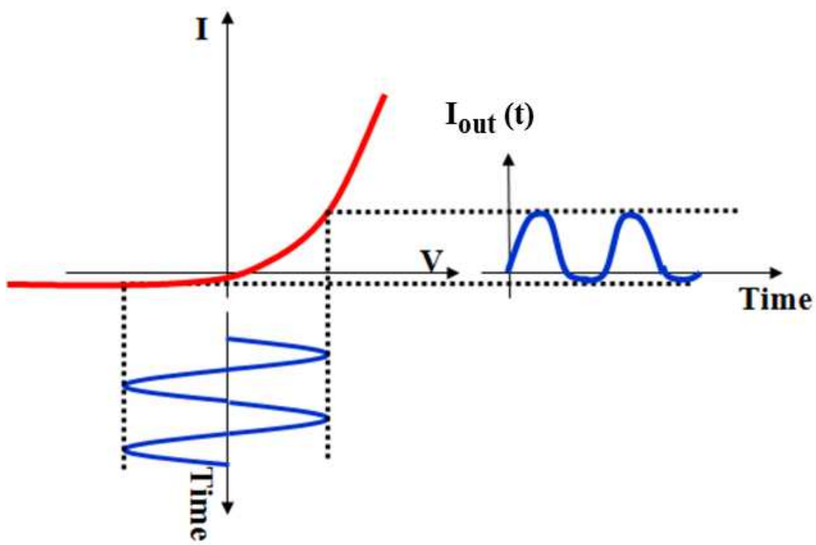

Figure 1.7 Rectification behavior of a Schottky Diode coupled with an incident RF wave at zero bias

(4) Novel THz detectors

The word novel here represents the meaning that those detectors applied new materials and detecting mechanism. Carbon Nanotubes (CNTs) are one of those materials which draw the attention of the whole research world, as well as in the THz detector region. Researchers have already applied metallic CNTs between antennas performing as a bolometer device, but it still requires low operating temperature for higher sensitivity. What's more, semiconducting CNTs have also been applied for Schottky diode THz Detectors contacting with source and drain metals. Further simulation results claims in [36] that for 2.5THz, the NEP can reach $0.7pW/Hz^{0.5}$ at room temperature

1.3. Goals of this research

THz imaging devices can be realized by forming THz Focal Plane Array (FPA) using numbers of THz detector cells. A CNT Schottky diode THz detector based THz imager is shown in Figure 1.8. Each detector cell is a single THz detector and performs as one pixel. When a source generated THz radiation, it is first focused by a array of micro-lens, which helps to converge the EM wave onto each high sensitivity detector cell, the detected signal such as voltage or current variation is then converted from analog to digital, which is then plotted to images by computer and software, this is the basic method to get the THz images in Figure 1.2 for medical treatment and security inspection. As illustrated in Figure 1.8, for getting a good image of THz signal, this imaging device requires large fabrication area, small detector unit, and high sensitivity of each detector cell as well as operating at room temperature. However, since conventional THz detectors such as pyroelectric and GaAs based devices are bulk in size and requires complicated small area semiconducting fabrication process which is quite costly, the integration of those detectors is hard to realize high resolution imaging. Moreover, the NEP values are relatively large for some of them at room temperature, which also indicates high sensitivity imaging cannot be effectively achieved. Table 1.1 [12] [36] summarizes NEP values as well as other features for several THz detectors.

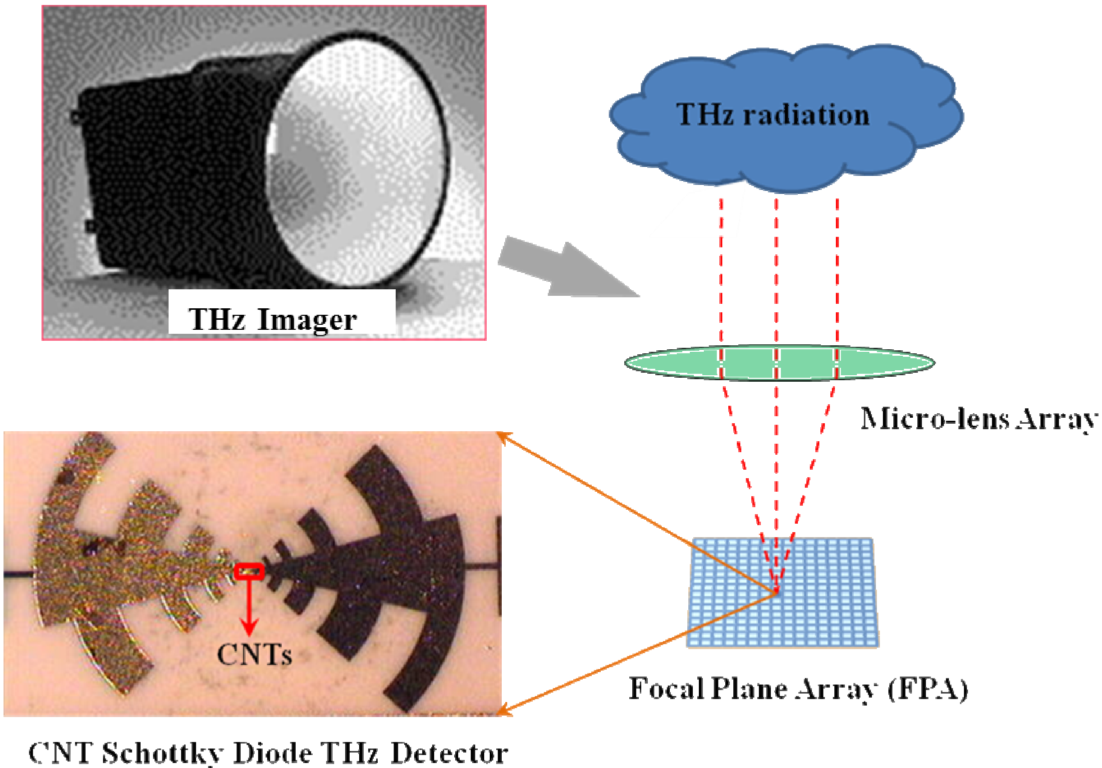

Figure 1.8 Focal plane array THz imager basing on CNT Schottky diode detectors

Table 1.1 Specifications of several THz detectors [12]

	Pyroelectric THz detector	GaAs Schottky diode THz detector	Golay cell THz detector	Bolometer	CNT Schottky diode THz detector (simulation w/wo matching)
Operating Temperature (K)	300	300	300	4.2	300
NEP ($pW/Hz^{0.5}$)	250~1000	100	100~120	0.1	5.5 / 0.7
Effective Size(mm)	2	0.5×0.2	2×9	---	0.1×0.1

This table clearly shows that CNT Schottky diode THz detectors have advantages over others in the sensitivity and device size. However, although some simulations shows that applying multi numbers of CNTs will decrease the contact resistance then decrease NEP to 0.7pW/Hz$^{0.5}$, the impedance mismatch was not taken into consideration. Furthermore, the fabrication processes for making such devices are mostly based on expensive high end techniques such as e-beam lithography and costly materials like quartz and sapphire. Those disadvantages limit the development of large area THz imaging.

However, the use of CNT in the fabrication of THz detector is an attractive approach. Since CNT Schottky diode detector has small device size, and allows for the separate fabrication of CNT material from the substrate material. It motivates us to find proper ways to realize the THz imaging challenges. But the NEP value is difficult to decrease using single CNT since contact and series resistance is around hundreds of kΩ, which not only increase the thermal noise but also bring in a huge impedance mismatch between the antenna element and CNT device at room temperature. Although some simulations shows that applying multi numbers of CNTs will decrease the contact resistance that in turn allows for decrease in NEP to 0.7pW/Hz$^{0.5}$, but the impedance mismatch was not taken into consideration. [36]. Furthermore, the fabrication processes for making such devices are mostly based on expensive high end techniques such as e-beam lithography and costly materials like quartz and sapphire. Those disadvantages limit the development of large area THz imaging.

Thus the goal of this research is to develop an efficient, room temperature operated, CNTs compatible but low cost large area compatible fabrication process and high sensitivity THz imaging devices, by applying flexible, low loss and cheap polymer substrates.

2. Carbon Nanotubes

After Iijima discovered multi-walled carbon nanotubes (CNTs) in 1991 at NEC, Japan [13] (Figure 1.9), people started talking about those hollow tubes and began doing research on those nano scale carbon material. Gradually, researchers found that CNTs not only perform a special shape on geometry, but also shows unique properties in mechanics, electric, optics and chemistry realms, they opened one possible path toward the nanostructure and nanoworld as well. Research in the area of CNTs is focused towards finding new applications, efficient growth, and approach to integration and self-assembly on surrogate substrate, and in further understanding of their fundamental properties. In this research work, CNTs are used as a Schottky Diode for THz wave detection.

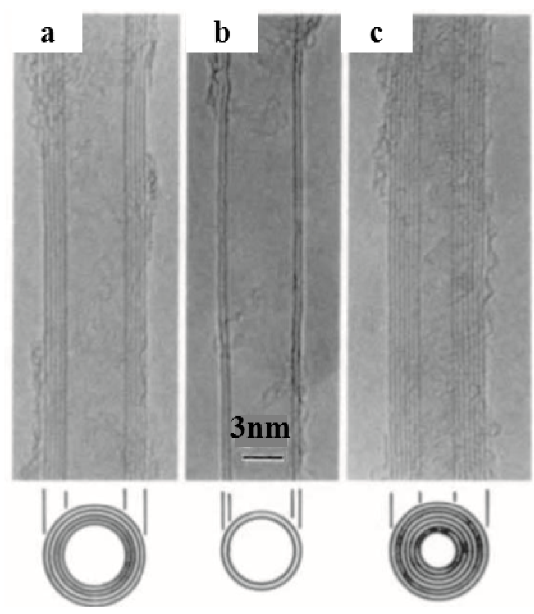

Figure 1.9 Multi-wall carbon nanotubes discovered by Iijima [13]

2.1. Geometry of CNTs

Carbon nanotubes are hollow structures, which can have single or multi walls, see Figure 1.9. CNTs can be attained from graphene, Figure 1.10 [14], layers, where the layers rollup to form hollow tubes, shown in Figure 1.11 [15]. Most of single wall CNTs have the diameter around 1 nanometer, multi wall CNTs can have larger diameter ranging from several nm to 100 nm. The distance between two walls remains the same due to the certain chirality of forming a specific CNT. There is no confinement of the length of CNTs, it can ranges from several nanometers to micrometers or even longer. Recently researchers have synthesized single wall CNT with the length of 4cm [16]. Synthesis of longer CNTs is under study to meet the needs for light weight high strength fibers.

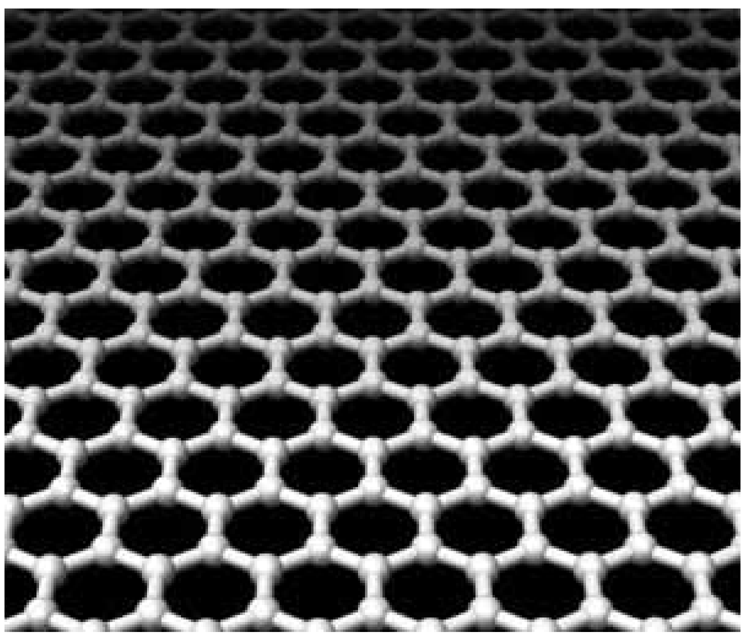

Figure 1.10 One layer of graphene [14]

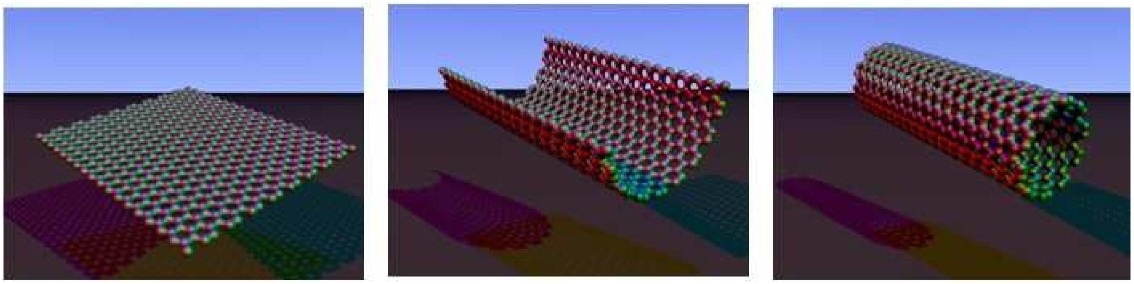

Figure 1.11 Rolling a graphene sheet to form a single wall CNT [15]

The rolling of graphene to form a closed cylinder is called chirality, which determines not only the structure of CNTs but also their properties. In order to understand this better, quantitative analysis is carried out by the assistance of figure 1.12 [17], which illustrates several chiralities to form one single wall CNT. Two basic vectors define the graphene lattice: $a_1 = d\left(\sqrt{3},0\right)$ and $a_2 = d\left(\sqrt{3}/2,3/2\right)$, where d=0.142nm is the length of the C-C bond. The rolling direction $\vec{C}$ is defined as $\vec{C} = n\overrightarrow{a_1} + m\overrightarrow{a_2}$, (n,m) is called the chirality of the CNT. The radius of the rolled up single wall CNT can be calculated by equation 1.4

$$R = \frac{C}{2\pi} = \left(\frac{\sqrt{3}}{2\pi}\right) d\sqrt{n^2 + nm + m^2} \qquad 1.4$$

For most of the cases, CNTs are randomly rolled to form so called chiral CNTs and n and m could be any value, including (0, 0), which is considered as a quantum dot in some research works. However, there are also two special situations which draw most of the research attention. One is that m=0, shown in figure 1.12(a), the graphene is rolled along a_1 direction, which is called zigzag CNT; another is n=m, shown in figure 1.12(b), the graphene is rolled up with same index of a_1 and a_2, this is called armchair CNT. Others are called chiral CNTs, showing in figure 1.12(c). From the property point of view, zigzag CNTs are semiconductors, armchair CNTs have metallic property. Also, if n-m is a multiple of 3, such single wall CNTs are metallic CNTs, otherwise are semiconducting CNTs. This is because although for a planar graphene sheet, the C-C bonds for one atom are equivalent, those bonds slightly changed due to creating the angles when it rolls up. Details can be found in Ref. [17]. In some circumstances, CNTs are not like a uniform cylinder or shape; they could bent at some points or even have some other structures on their bodies, Figure 1.13 shows a bent CNT and a nanobud joint on the wall of CNT. The CNTs in this research are semiconducting single-wall CNTs the m, n values also determine the semiconducting properties such as energy gap, which will be shown several sections later

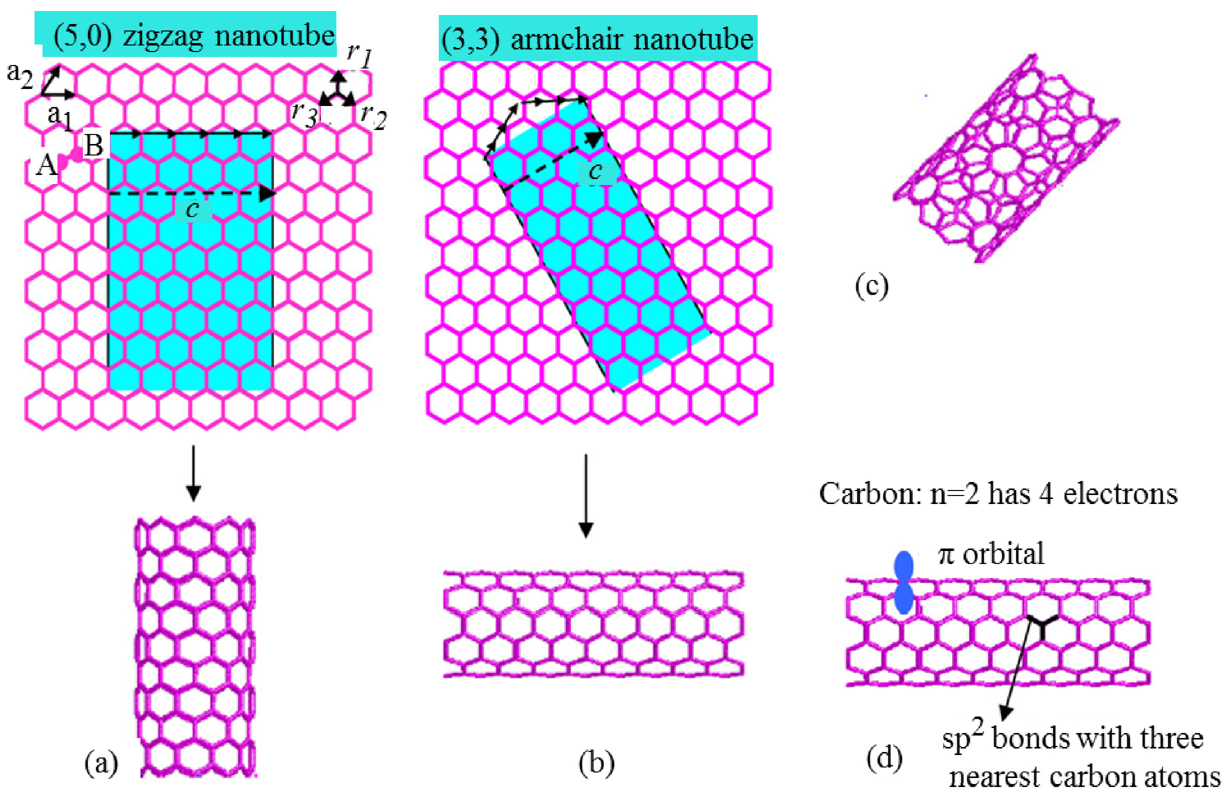

Figure 1.12 Different chiralities of CNTs, (a) zigzag CNTs, (b) Armchair CNTs, (c) Chiral CNTs, (d) Strong sp^2 bonds within three nearest carbon atoms [17]

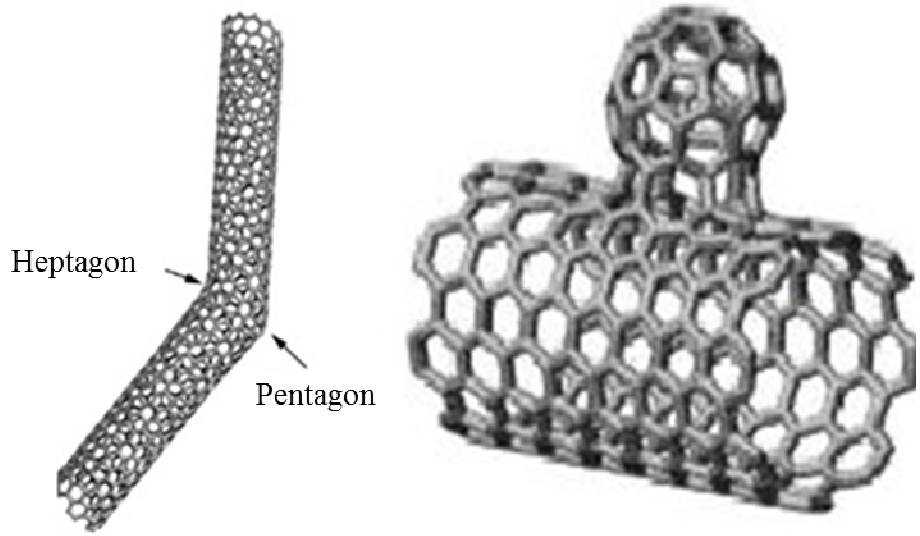

Figure 1.13 (Left) a bent CNT with pentagons at the turning point. (Right) a nanobud joint on the wall of the CNT [17]

2.2. Synthesis of Carbon Nanotubes.

Carbon nanotubes can be grown by laser ablation, arc discharge, and CVD process.

2.2.1. Laser ablation

Showing in Figure 1.14[38] in particular, a high power laser beam is focused on a bulk graphite target, which is located inside a furnace with temperature of 1200°C in Ar ambient. CNTs are collected by a Cu-cooled water trap. The advantage for this method is that single wall CNTs can be synthesized quite readily. However, the system requires high power laser source, and the yield is low, and the cost is prohibitive.

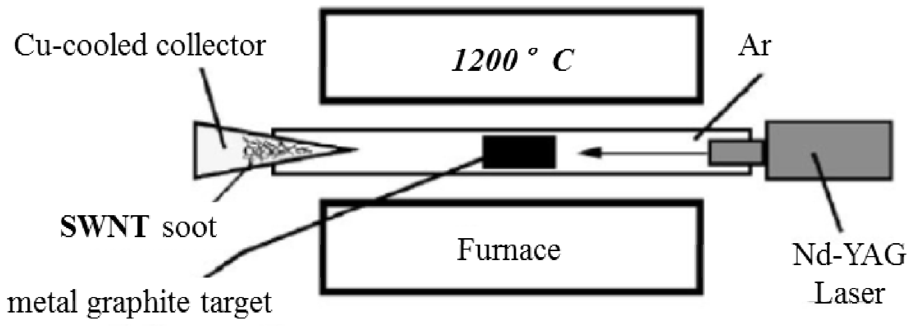

Figure 1.14 Experimental setup of laser ablation for CNT growth [38]

2.2.2. Arc discharge

CNTs discovered by Iijima were synthesized by this method, shown in Figure 1.15 [38]. This technique involves the passage of a direct current (80-100A) through two high-purity graphite electrodes separated by 1-2mm, in a He atmosphere. During arcing, a deposit forms at a rate of 1mm/min on the cathode, while at the same time, anode which has Fe catalyst is consumed. Although this method could produce both single wall and multi wall CNTs, the diameters of CNTs is difficult to control. Also, the cost of this process is still high associated with the use of pure material and the need for post purification process.

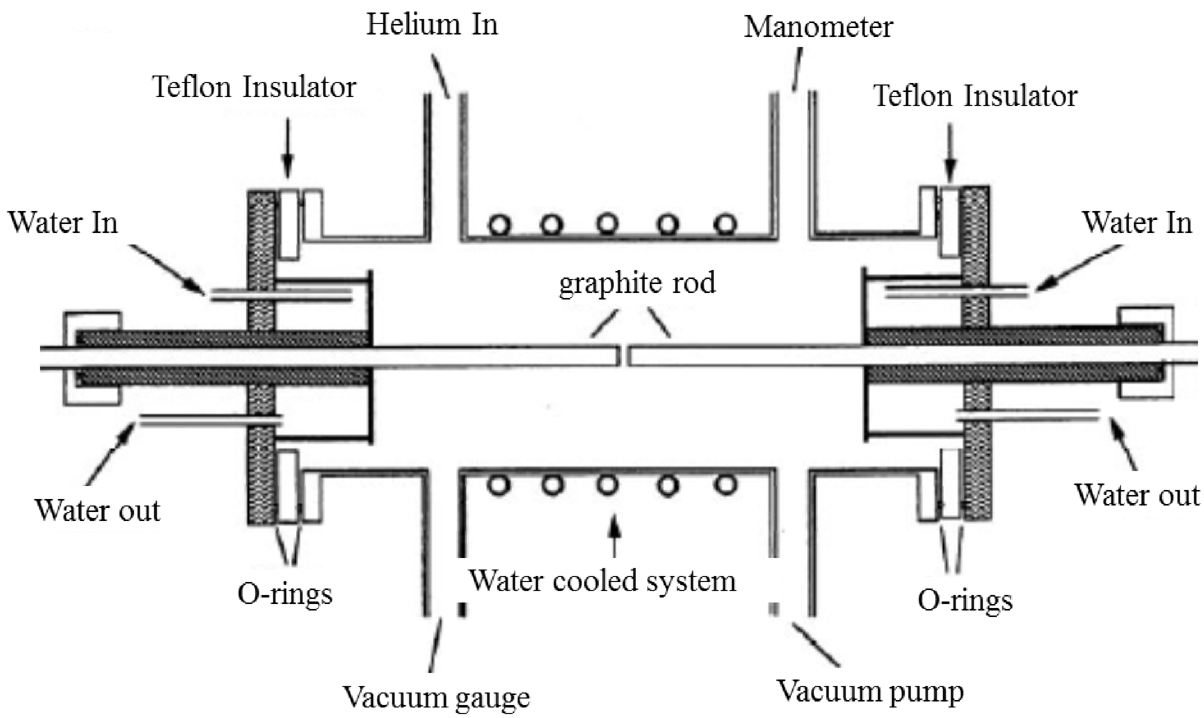

Figure 1.15 Schematic of an arc discharge system [38]

2.2.3. Chemical Vapor Deposition (CVD) process

CVD process can be divided into two categories: thermal CVD and microwave plasma enhance CVD. Both of these methods work on similar principles: deposit certain metal catalysts on the substrates for further growth. In a thermal CVD process, the substrate with catalysts is placed in a hot tube shape furnace (above 1000°C), precursor gas such as CO, methane and ethylene are flowed into the tube with Ar. The growth rate and the CNT diameter can be controlled by the concentration of the precursor gas and the selection of the catalysts. Using a catalyst, metallic or semiconducting CNTs can be easily grown. . Microwave plasma CVD has almost the same growth mechanism except that microwave is used to generate the heat that in turn decomposes the precursor gas. In comparison to other growth methods, the CVD method is more efficient and cheaper. Moreover, by patterning the catalysts on the substrate, CNTs can grow vertically (Figure

1.16) [15] and form CNT array for further applications. However, the purification is still need to be done since the catalysts are always with those CNT forests and there is high possibility that they will influence the properties of CNTs in some applications.

Since CVD method is cheaper than the other two methods, if has been commercialized by many companies. In this research, semiconducting single-wall CNTs are made by CVD and bought from NanoIntegris Inc. With certain purification process, catalysts are eliminated and high concentration semiconducting CNTs can be filtered out for further scientific research.

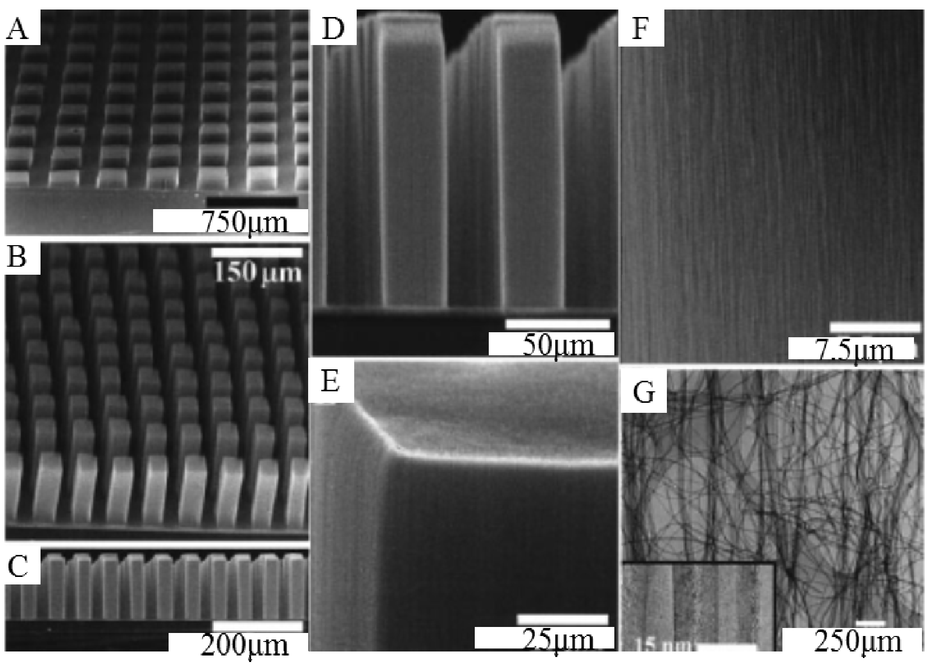

Figure 1.16 (A-D) vertically grown CNT array, (E, F) Zoom in image of the one block, (G) TEM image of CNTs in A through F [15]

2.3. Properties and applications of carbon nanotubes

2.3.1. Mechanical properties and applications

The physical structure of high aspect ratio of CNTs and strong C-C sp^2 bond provide amazing mechanical properties comparing to other materials. Table 1.2 shows some properties of CNTs comparing with others. As it cleared shown here, both MWNT and SWNT have higher values on strength such as Young's modulus. The value of tensile strength (13-53 GPa) of CNTs is also way higher than that of steel (0.38-1.55) [15]. Diamond is believed as the hardest material in the world, however, people found that bulk SWNT composite can have even higher value of hardness around 462-546GPa, comparing of 420GPa of diamond [18]. Moreover, the density of CNTs is around 0.7-1.4 g/cm^3, it is believed the lightest material which also performs strong strength and high melting point.

With those advantages that CNTs have, the material industry and research institutions start to study and apply those great properties in our daily life. Due to the high value of strength and small density, researchers at MIT are studying to apply CNTs on body armor for military usage [19]. Also, CNTs can be integrated onto common clothes fibers to enhance the strength of them in order to meet the needs in extreme environments, as shown in figure 1.17. Moreover, CNTs are able to increase the strength of the sports equipments basing on their hardness and lightness. Nanoscale probe tips can be fabricated by small diameter but long CNTs. It is also possible to fabricate nano syringe by CNTs with the hollow cylinder as the container. Another promising application is using CNTs to fabricate micro even nano bearings and gears for NEMS (Nano Electro-Mechanical System), as shown in figure 1.18 [20].

As discussed above, CNTs superior mechanical properties such as large Young's modules and tensile stength could let CNTs stay firmly on the devices and rigidly keep the geometry unchanged. This could put the fabrication process in this research on the safe side, since there is no need to worried about the deformation of the CNT structure due the side effects of fabrication such as accumulation of stress during metal deposition

Table 1.2 Comparison of mechanical properties of CNTs to others

Material (*Single-Crystal)	Young's Modulus (GPa)	Melting Point (°C)
Multi-Walled Carbon Nanotube	1280~4150	750(air)-2800(vacuum)
Single-Walled Carbon Nanotube	1000~1250	
Diamond*	1035	3527
SiC*	700	2827
Al_2O_3*	530	2052
TiC*	497	3140
W	410	3422
Si_3N_4*	385	1975
Mo	343	2623
Steel (Maximum Strength)	210	1539
Stainless Steel	200	1539
Iron*	196	1539
Si*	190	1414
SiO_2(Fiber)	73	1710
Al	70	660

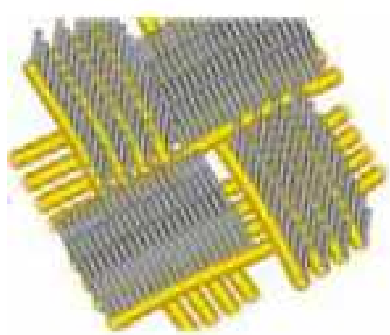

Figure 1.17 CNTs (grey) entangled with clothes fibers (yellow) to increase the strength of the clothes (RPI and University of Hawaii)

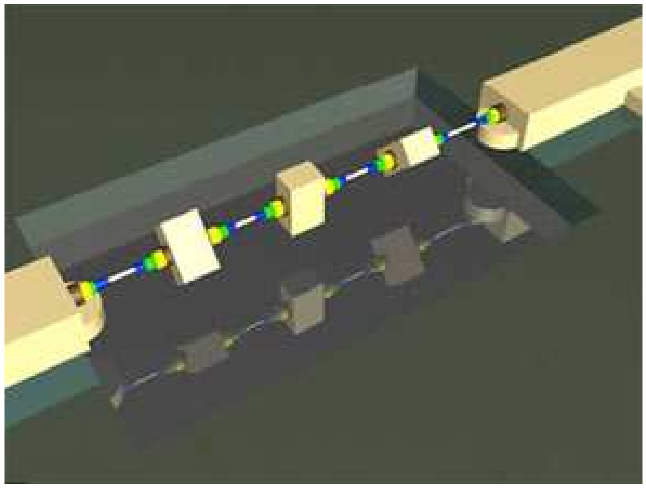

Figure 1.18 CNT bearing blocks [20]

2.3.2. Electronic properties and applications

As discussed above, the chirality of CNTs determines the conducting property of CNTs, i.e. either metallic or semiconducting. This is due to the slightly change of C-C bond when rolling up the graphene sheet.

Metallic CNTs are well known for its capability of carrying high value of current without breakdown. It has shown that metallic CNTs can stand for 10^{13}A/cm^{2} while copper is around 10^{8}A/cm^{2}. What's more, the thermal conductivity of CNTs is quite high which means heat generated by the current can dissipate fast. Researchers also measure the conductance of CNTs. Due the nanoscale of CNTs, the electron transportation in CNT is one dimensional, which is only along the axis of the nanotube. Also, CNT-metal contacts behaves quantum conductance, which indicates that electrons are more likely to "move" in one certain conduction band instead of "jumping" up and down to other energy band. One quantum conductance stage is denoted as G_0 and it equals to 77mS at room temperature. For even lower temperature, such value could be doubled and the quantum resistance goes down to 6.5KΩ. Furthermore, since the length of CNTs is in micro or even nano range, electrons can transport only obeying Newton's Secondary Law in such short distance without being scattered by defects, only interacting with phonons, this is called ballistic transportation.

Metallic CNTs have many applications. Due to the high current bearing, one can use metallic CNTs as the interconnection between metal wires in nanoscale integrated circuits, as shown in figure 1.19. The electron ballistic transportation in CNTs provides non-resistive current in a short distance. Also, with multiple CNTs parallel connected, the contact resistance could also reduce from $1/G_0$ to $1/(nG_0)$ (n is the number of CNTs). However, there are still problems need to be solve: the contact resistance is not easy to reach $1/G_0$ due to the defects of CNTs and bad contact with metal; also, such small devices require nanoscale fabrication, which are always too expensive to put onto the market. Another application for metallic CNT is combining its high aspect ratio with high current density, CNT based field effect display (CNT FED). Figure 1.20 shows a simple schematic structure of the CNT FED. High electric field is generated between cathode and gate electrodes, high current can be generated in CNTs. When the current is high enough, some of the electrons will tunnel though the barrier at the top of the CNTs and continue travelling to the anode and hit fluorescent on the glass. The brightness of such display is comparable with current LCD display, while consuming less power.

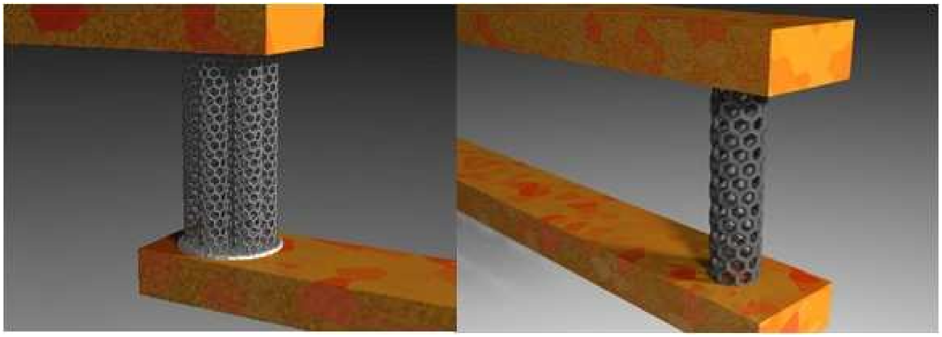

Figure 1.19 Metallic CNTs act as interconnection between metal wires (courtesy of Infineon Technologies)

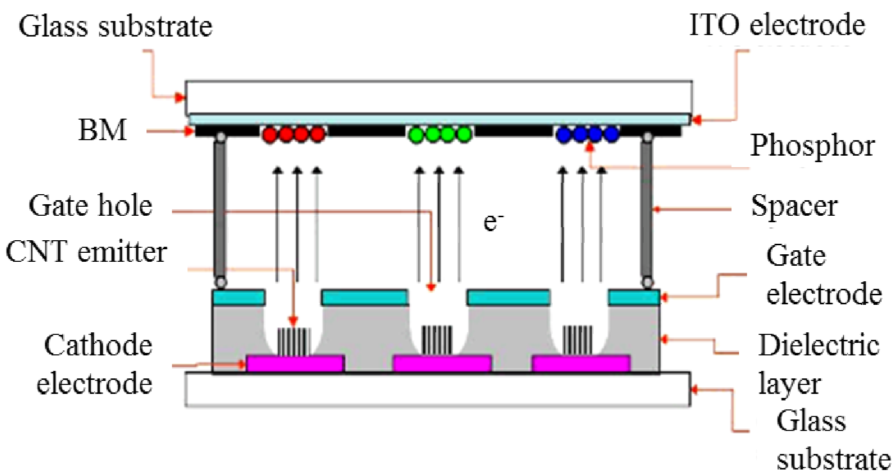

Figure 1.20 CNT FED structure (Teco Nanotech Co.Ltd)

Semiconducting CNTs only have single wall. This is because the smaller the diameter of the CNTs, the larger the bandgap it has. For a certain value of diameter, the bandgap tends to diminish and CNT turns out to be metallic. This means that all the multi-wall CNTs are metallic. The bandgap E_g can also be calculated by equation 1.5, where $V_{pp\pi}$=2.97eV is the nearest neighbor interaction parameter, d is the length of C-C bond and R is the radius of the CNT. Combining with equation 1.4, one can calculate the bandgap for CNTs with certain chiralies.

$$E_g = V_{pp\pi} \times d / R \qquad 1.5$$

For an intrinsic semiconducting CNT, the band diagram is shown in figure 1.21 [21], it shows the fact that the conduction and valance bands are symmetric with each other, which also means the effective mass of electrons and holes are almost the same. However, in reality, most of those semiconducting CNTs perform p-type behavior. This is because CNTs are very likely to be oxidized in air and oxygen molecules act as a source for dope to increase the concentration of holes, which in turn shows p-type in a larger view. It is also possible to reverse this phenomenon and turn p-type CNTs back to n-type. Some of the researches tried to dope CNT with alkali, or anneal the CNT in a vacuum oven around 800°C or in an inert gas environment [17].

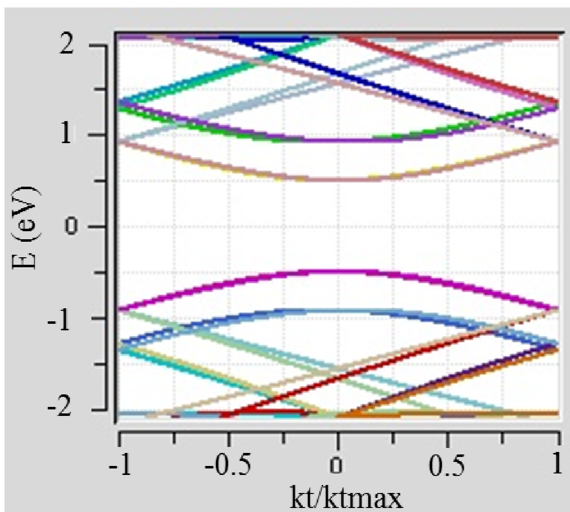

Figure 1.21 Band diagram of semiconducting CNT with chirality (10, 2) [21]

People has already applied semiconducting CNTs to fabricate CNT based Field Effect Transistors (CNTFET). CNTs here replace the n wells and make the devices size smaller comparing to conventional MOSFETs. Moreover, the fabrication process can be simplified. Researchers have already fabricated a CNTFET based inverter, which is shown in figure 1.22 [22]. CNTs are first deposited on a SiO_2 and Potassium is then deposited by e-beam lithography. In order to form the n-type FET, the device was put into vacuum oven to anneal about 10h, at 200°C. Then a polymer is covered on n-FET to prevent CNTs turning back to p-type, finally the whole device is shined with O_2 plasma to form a better p-FET. The results were promising and the gain is great than 1. Later, CNT logic gate array have been developed in order to realize large area batch fabrication [23]. Many CNT FET researches are being studied currently, and more and more results are being carried out.

Semiconducting CNTs can be used to fabricate Schottky diode devices by contacting CNTs with metals which have smaller work function than CNTs do. Our research is among one of those applications. Conventional Schottky diodes use bulk materials as the electrodes and oxidation layer for the fabrication, while CNTs are one dimensional material contacting with 3D electrodes. Researchers showed that the metal CNT junction plays an important role of the whole device. It is necessary to fundamentally understand the basic of the metal-CNT junctions.

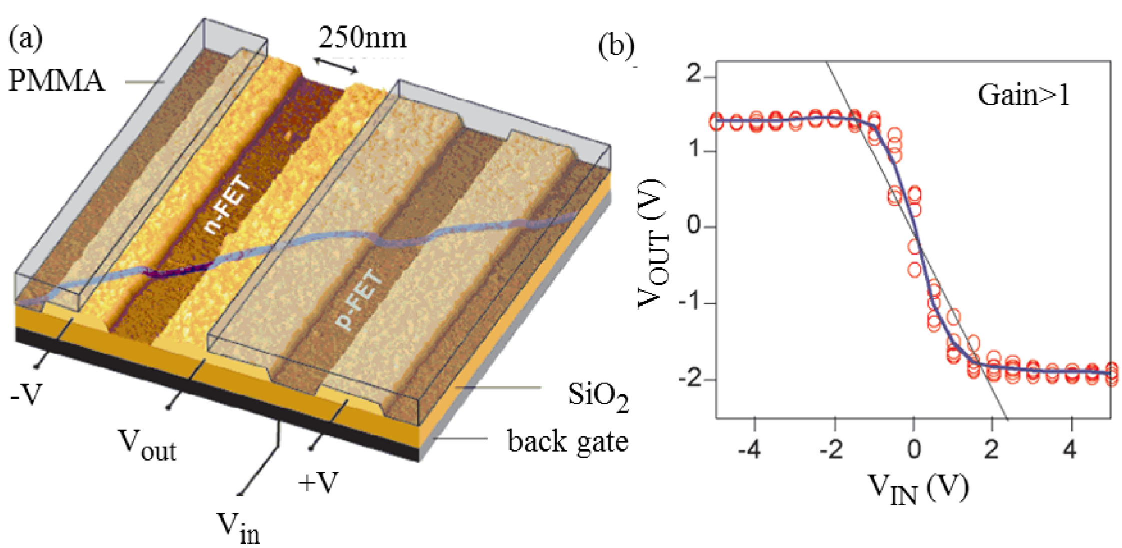

Figure 1.22 AFM picture of CNT inverter (a), I-V curve of this inverter (b) [22]

Functionalized CNTs, which decorated by some specific molecules on their walls by certain chemical reactions, can also be used as sensors for detecting biological signals and chemical materials by changing the conductance due to those molecules attaching on their surface. One can also use CNTs in gas chromatography for absorption and desorption, due to their high aspect ratio and the ability that desorbing gas molecules those absorbed on their walls when heated

3. Metal-CNT junction

As mentioned above, due to the different dimension of two materials, CNTs and metal contact will perform different behavior comparing with that of 3D materials. It is also a key role governing the performance of the CNT devices. The selected metal for contacting must first meet the requirements of the devices such as Schottky barrier height, and the fabrication compatibility. Even one kind of metal has a better contact with CNTs but is not compatible with the fabrication, the research will more or less goes to a struggling and no ending situation for finding the best material. In Chapter 2, we will explain what metals are suitable to form Schottky contact and ohmic contact basing on the band diagram, here we only discuss which way and metal could provide a better contact with relatively small contact resistance and large binding energy. Although we could find a better metal for fabricating the devices, a clear understanding of metal-CNT contact is still elusive and requires more effort on such research.

3.1. Metal contact formation

The CNT-metal contacting has three forms: side contact, end contact and buried contact. Side contact means CNTs lie on the top of the metal electrodes and only contact with their side. End contact represents the contact is only at the end of CNTs and the metal, which also means less atoms are connected between CNTs and metal. Buried contact means CNTs are buried by the metal at the contact part. Figure 1.23 shows the structures of side contact and buried contact. The surface area contact is desirable to achieve low contact resistance values. This translated to atom scale means more atoms are connected and more" channels" are opened for electron transportation. It has been clearly established that buried metal-CNT contact has lower contact resistance compared to side and end contacts [25]. In [25], although the experiments were based on multi-wall CNTs, it still holds for single-wall CNTs as the electron transportation only happens on the outer wall. The only difference is for buried contact: the inner layers of multi-wall CNTs also provide conductive path between the pads thus the series resistance is much lower than that of single wall CNT. Thus, in order to achieve low contact resistance, buried structure was chosen in this research. Moreover, the deeper the CNT extended into the metal, the lower the resistance it will has [26].

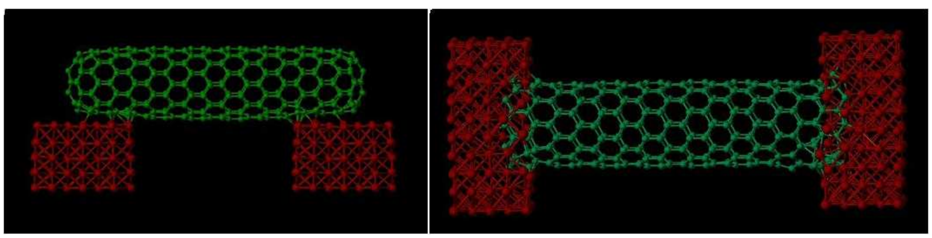

Figure 1.23 CNT-metal side contact (left) and buried contact (right) [24]

3.2. Atom binding energy and binding diagram

The firmer the binding between C and metal atoms, the more stable the contact. So studying the binding energy of metal-CNT junction is another aspect to understanding the working mechanism. Ref [27] applied psedupotantial plane wave method within local density approximation to study the binding energy of 5 atom layers. Table 1.3 shows the binding energy between Au, Pd and Pt at the equilibrium binding distance. It is clearly shown that Pd has higher binding energy in comparison to Au and Pt. This could possibly be due to the electron orbit difference between those three metals. Complete understanding of the actual mechanism is not clear. Binding diagram has been carried out in [28] and is shown in figure 1.24. It shows that for Au-CNT contact, only one atom is connected with Carbon atom, while Pd has 6 atoms having bonds with CNT. This can explain the reason that Pd has a higher conductance (77mS) than Au does at room temperature, and why most of the CNTFET use Pd as the contact metal.

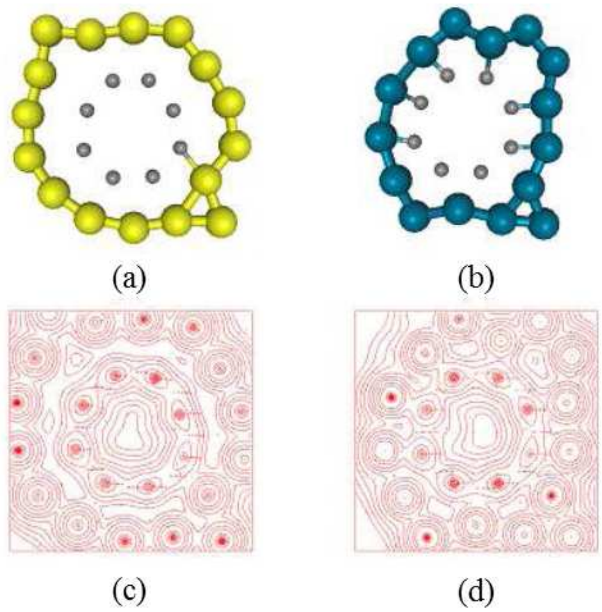

Figure 1.24 Atomic cross section of the metal CNT interface for Au (a) and Pd (b), Contour density plot for Au (c) and Pd (d) [28]

Table 1.3 Binding energy at equilibrium binding distance [27]

Metal (Orientation)	Equilibrium binding distance (A)	Binding energy (eV)
Au (111)	2.91	0.61
Au (100)	2.40	0.74
Pd (111)	2.12	2.00
Pd (100)	2.04	2.70
Pt (111)	2.12	1.69
Pt (100)	2.10	2.30

Au, Pd and Pt are the metals whose work functions (above 5.0eV) are higher than that of CNTs (4.9eV). These metals can be used to make Ohmic contacts with semiconducting CNTs. This will be further discussed in Chapter 2. In order to form Schottky contact, metals with work functions lower than that of CNTs are required. Typically, those metals could be Cu, Ti, Al, Sc, Cr and Ag. From fabrication point of view, although some researchers have demonstrated good results, Sc and Cr are not very compatible with regular fabrication process as well as our low cost flexible substrate. Cu is commonly used metal in microfabrication but its work function (4.65eV) is close to CNT's and the nonlinear property will be weak. Al can be a good candidate since it has been already widely used in CNTFET fabrication, and showed good results. Ti is also a promising metal because it has good adhesion to most surfaces and it is quite possible that Ti could have a better binding with CNTs as well.

3.3. Post Treatment for Metal-CNT Junction

It has been said that Rapid Thermal Annealing (RTA) could help in lowering the resistance by changing the formation of carbide at the interface. Figure 1.25 shows the conductance variation for different RTA temperature [29]. The higher the annealing temperature the higher the conductance of the device will have. Some researchers have also applied higher voltages between the two electrodes in order to heat the metal contacts. This is called current-induced heating joule techniques [30]. The results are promising but it still has the chance of burning down the CNT, especially 2μs for 7V cannot be controlled precisely.

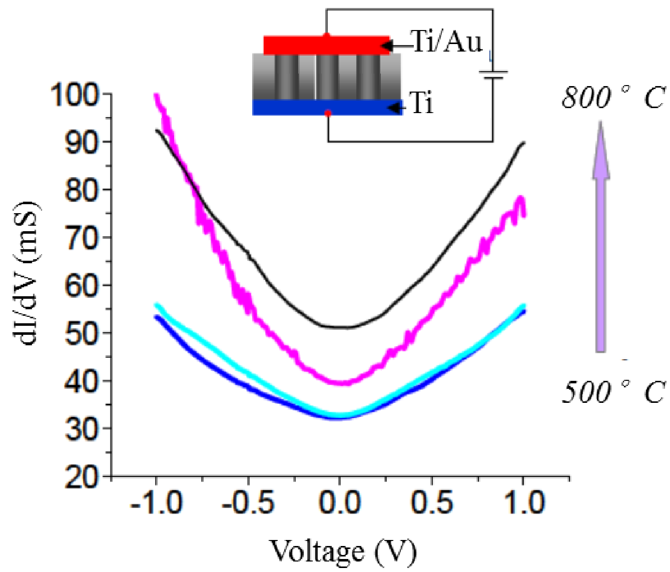

Figure 1.25 Conductance of rapid thermal annealed CNT as a function of annealing temperature [29]

Basing on the discussion above, one could select Pd as one end of contact and Al or Ti for the other end. Moreover, Au could also be tried since Pd is not very compatible with regular fabrication process especially for etching. Also, annealing is necessary for reducing the contact resistance if applicable. Simulation of those metal-CNT contacts will be carried out in Chapter 2. Chapter 3 will mainly focus on the fabrication process of the proposed device.

4. Polymer based substrates

Polymers are defined as a type of materials who have large molecules repeats that are connected by covalent chemical bonds, shown in figure 1.26. These are also commonly known as plastics. There are a large number of naturally and artificially synthesized materials with variety of properties [31].

The cost for synthesizing polymer materials is quite low, which also allows for large area manufacturing. . One of the most popular polymers being used in our daily life is Polyethylene terephthalate, or called PET, PETE, which is a thermoplastic and widely used in food packaging, beverage containers and houseware manufacturing due to its chemically inert and low moisture absorbing properties.

In the scientific engineering research, such as biological, chemical, material and electrical engineering, polymers have also gained significant interest [32][34]. Silicone for plastic surgery and body implanting research is a good example. In electrical engineering, especially in the micro fabrication process, Photoresists such as S1813 and AZ series for lithography are the core materials of the whole process. Moreover, new polymers, like PMMA, SU-8 and PDMS (Polydimethylsiloxane) have been introduced in to create novel fabrication process and micro devices. By shining UV light on SU-8 and O_2 plasma treatment on PDMS, the crosslinks between the macromolecules change their property and by applying further operations, one can create any structures he want basing on polymer manipulation[32][33]. However, although polymers are widely applied in micro and nano fabrication, they always use conventional materials as the substrate, such as silicon, silicon dioxide and silicon nitride. For high frequency (microwave and THz) operating devices, low loss materials like sapphire and quartz are preferred, but the high cost of those materials limits their fabrication process to a large area and limits their applications. From the view of high frequency device packaging, substitute materials with low cost are urgently required to replace conventional substrates. In order to solve this problem, our research group, recently systematically and quantitatively studied several polymer materials for THz substrate applications [35], as shown in Figure 1.27. HDPE, Zeonor, PTFE and Propylene have low loss characteristics over a wide frequency band. Some of these materials can be used over a narrow band where the dielectric loss is low. For example, PET is low loss below 500 GHz [35].

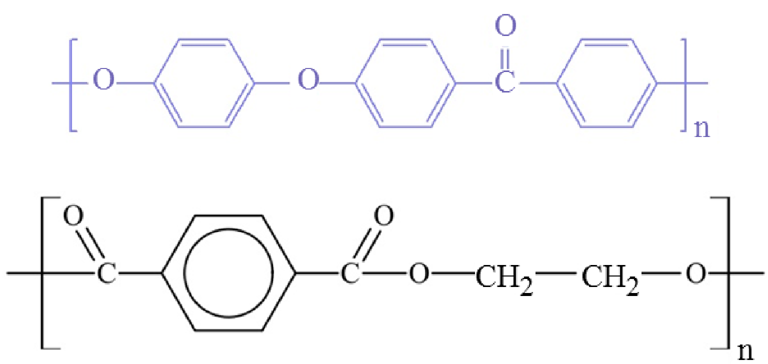

Figure 1.26 Chemical Structures of Polyether ether ketone (PEEK) (upper) and Polyethylene terephthalate (PET) (lower)

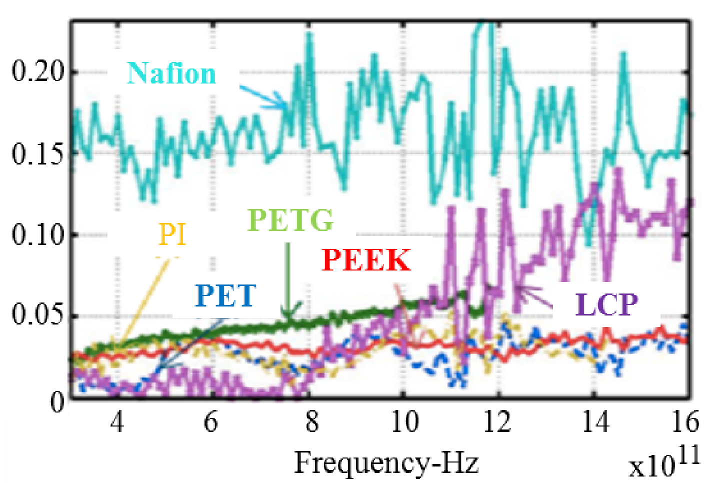

Figure 1.27 Loss tangents of some polymer materials [35]

Another pre-requisite of applying those polymers is the compatibility with regular micro fabrication process. Some of the plastics, like Polystyrene can react with cleanroom chemicals like acetone and isopropanal. Other materials such as PET, PEEK and Polyimide are chemically inert to most of these chemicals, and also to HF. Melting point, glass temperature and other thermal parameters are also needed to be taken into consideration. Table 1.4 [37] shows some values of thermal properties for three polymer candidates. In most of the micro fabrication process, high temperature will occur during the bake process of the lithography and metal deposition period. Polymers glass temperature should higher than the maximum value during the whole process, otherwise the polymer will become brittle or will warp. In our research, metal electrodes are deposited by e-beam PVD system where the temperature on the substrate could reach as high as 80- 100°C during the process. Thus PET would be not able to stand for long time. Thermal conductivity provides the ability that transferring the heat to the environment, the higher the value, the more suitable for fabrication since the stress on the surface will be lower and the cracks will be less.

Table 1.4 Thermal properties of PET, PEEK and Polyimide [37]

	Melting Point (°C)	Glass Transition Temperature (°C)	Thermal Expansion Coefficient (K^{-1}) (Linear)	Thermal Conductivity ($Wm^{-1}K^{-1}$)
PET	>250	75	3.9×10^{-5}	0.15-0.24
PEEK	~343	143	2.6×10^{-5}	0.25
Polyimide	---	>400	5.5×10^{-5}	0.52

Chapter 2 Simulation of CNTs Schottky Diode THz Detector

1. Metal-Semiconductor Contact

When a metal and a semiconductor are brought together to form the contact, due to the different Fermi energy levels in metal and semiconductor, electrons in one material with higher energy tend to flow towards the other one with lower electron energy. This results in some amount of energy band bending at the contact region (depletion region). As we know for the p-n junction, electrical charges at depletion region in p and n type semiconductors have opposite signs having same absolute values, the width depends on the charge densities of the two materials. However, because metal has much higher charge density than semiconductor, the depletion width in metal can be ignored, and the electric field and band bending only exist inside the semiconductor part. The amount of band bending and electrical properties such as electric field, potential distribution and flow of electrons depend on metal and semiconductor work functions, electron affinity and doped type of the semiconductor. Details will be discussed as below:

1.1 Conventional Metal-Semiconductor Contact

Conventional bulk metal- semiconductor contacts can be used to demonstrate the basic contact concepts. What's more, depending on whether there is a depletion region or not, M-S contacts can be grouped into two forms of contacts: Schottky Contact and an Ohmic Contact. There are several parameters which are used to analyze these two different contacts:

Work function Φ: The energy difference between the Fermi energy and the vacuum level;

Electron affinity χ: The energy required to extract one electron from the conduction band of the semiconductor into the vacuum, which is given by the difference between the bottom of the conduction band and the vacuum level.

1.1.1 Schottky Contact

A Schottky Contact (Schottky barrier) is also called rectifying contact. One type of Schottky Contact is formed by an n-type semiconductor contacting with metal whose work function Φm is larger than that of semiconductor Φ_{ns} (Φ_m-Φ_{ns} >0). Another Schottky Contact is formed by smaller work function metal contacting with a larger work function p-type semiconductor (Φ_m-Φ_{ps} <0). For the first case with an n-type semiconductor whose Fermi Level is near the conduction band, the Fermi Levels on both sides become equal at the junction region, resulting from the electrons moved from the semiconductor to the metal leaving minority carriers behind and form a depletion region, which is simply shown in Figure 2.1 (a) [56]. In the second case with a p-type semiconductor in which Fermi Level is close to the valence band, the Fermi Levels also tend to get equal at both sides during the electrons move from the metal to the semiconductor creating minority carriers on both sides and form the depletion region, as shown in Figure 2.1(b). Due to the existence of the depletion region in both cases, Schottky Contact has an I-V curve with rectification behavior and used as rectifying devices. The current-voltage relation is shown in Eq. (2.1):

$$J = J_0\left(e^{\frac{qV}{nk_bT}} - 1\right) \tag{2.1}$$

Where, J_0 is the reverse saturation current density and is related to the Schottky Barrier Height

Φ_B :

$$J_0 = A^* T^2 e^{\left(-\frac{\phi_B}{n k_b T}\right)} \qquad 2.2$$

1.1.2 Ohmic Contact

An Ohmic contact is formed by contacting a metal and an n-type semiconductor with Φ_m-Φ_s <0 or a p-type semiconductor with Φ_m-Φ_s >0. If one metal contacts with an n-type semiconductor and Φ_m-Φ_s <0, Fermi Levels on both sides also pin to the same level due to electrons moving from metal to the semiconductor, although positive charges are formed on the metal side near the junction, the majority carrier on the semiconductor side are electrons and accumulating which cannot form the depletion region. This also happens in the situation of metal contacting a p-type semiconductor with Φ_m-Φ_s >0, except that majority carriers holes accumulates on the semiconductor side. Figure 2.2 (a) and (b) [56] shows these two cases. If applying bias on the junction, the I-V characteristic shows resistive behavior, which obeys the Ohm's Law.

Table 2.1 shows a summary of Schottky and Ohmic contact related to the work functions of metals and semiconductors.

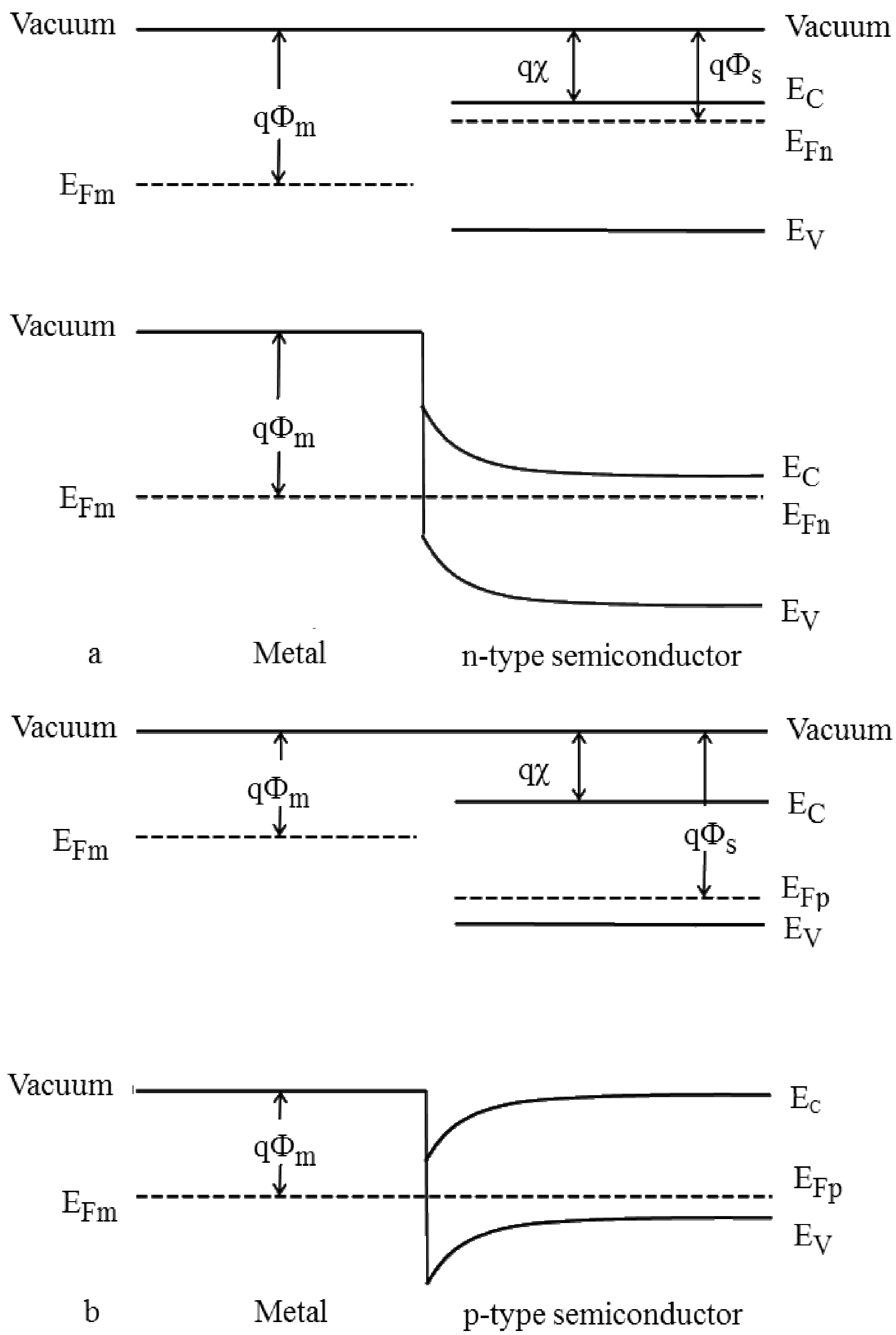

Figure 2.1 Forming Schottky contact basing on (a) n-type semicondutor and (b) p-type semiconductor and their rectifying I-V behavior. (next page) [56]

Figure 2.1 (cont’d)

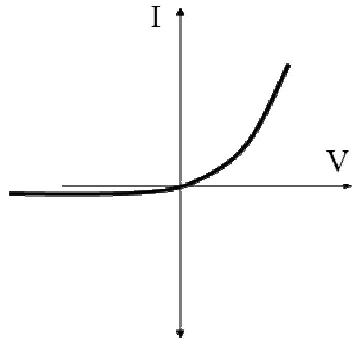

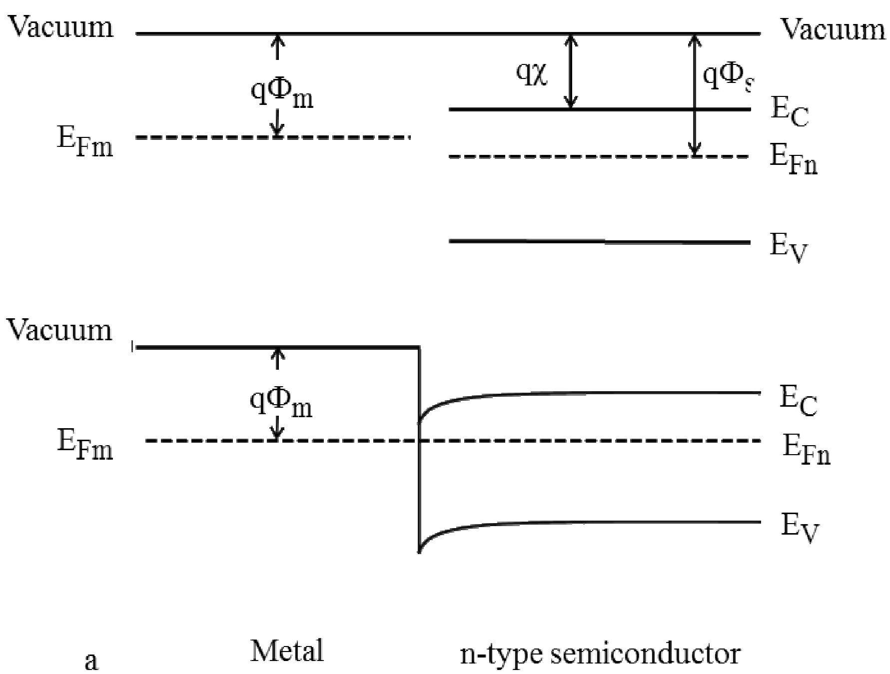

Figure 2.2 Forming Ohmic contact basing on (a) n-type semicondutor and (b) p-type semiconductor and their resistive I-V behavior.[56]

Figure 2.2 (cont'd)

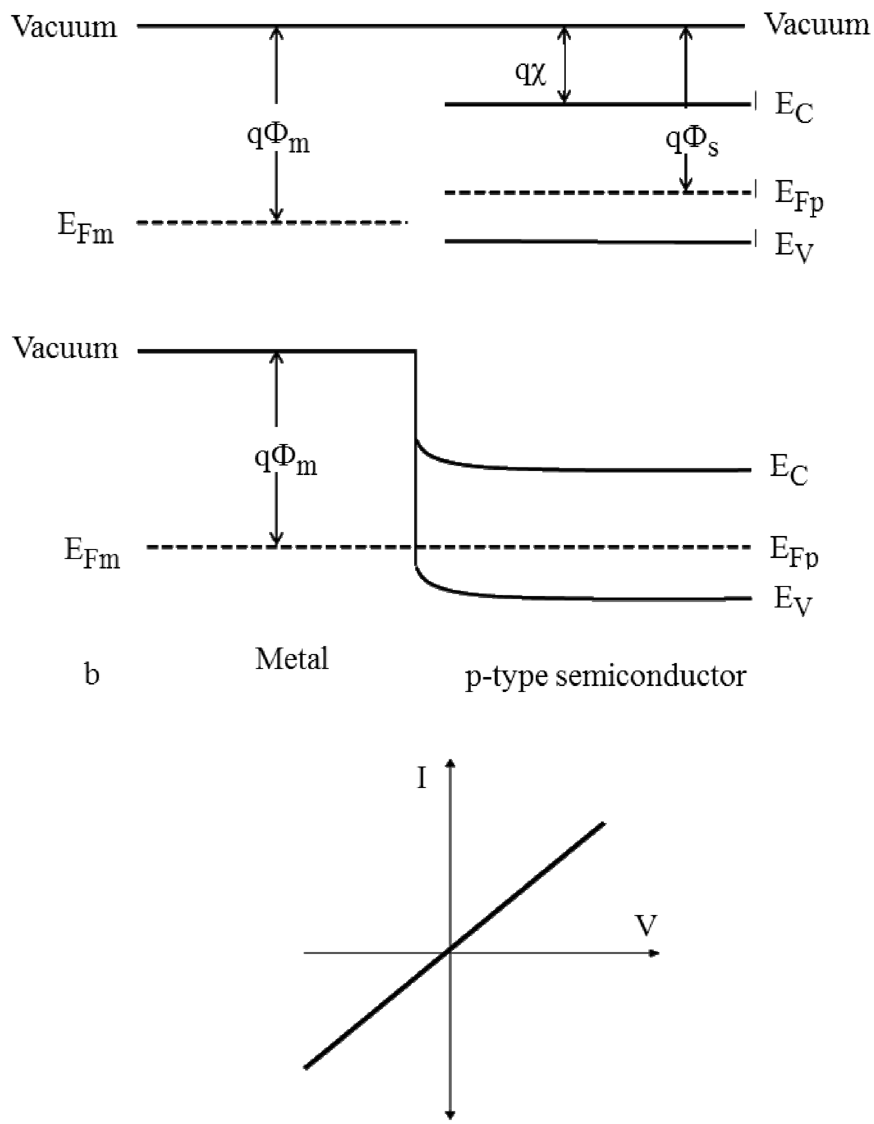

Table 2.1 Summary of forming Schottky and Ohmic contacts [56]

	p-type semiconductor	n-type semiconductor
$\Phi_m<\Phi_s$	Schottky Contact	Ohmic Contact
$\Phi_m>\Phi_s$	Ohmic Contact	Schottky Contact

1.2 Metal-CNTs Contact

As mentioned in the first chapter, all of the multi-wall carbon-nanotubes are metallic. Single-wall CNTs can be either metallic or semiconducting, depending on which chirality the graphene sheet is rolled up as [39]. Most of the s-SWNTs are p-type due to exposure to oxygen and naturally doped in air environment [40]. Doping with donor material such as potassium or annealing in vacuum can transform p-type s-SWNTs to n-type [41], however, the transforming requires process that is more complex and the annealing is reversible. In our research, p-type s-SWNTs were used for all the simulations and experiments. In order to form Schottky and Ohmic contacts on each end of s-SWNT for THz sensing, metal selection should be considered carefully.

Single-walled semiconducting CNTs(s-SWNT) have the work function around 4.8-4.9eV [42], As shown above, for a p-type semiconductor, Φ_m-Φ_{ps} <0 is required to form a Schottky Contact, while for an Ohmic Contact, Φ_m-Φ_{ps} >0 is needed. According these two rules, we can choose metals and contact with each end of the CNT and form specific contacts. For Schottky Contacts, the most common used metals are silver (Ag), Aluminum (Al) and Titanium (Ti), whose work functions are lower than 4.9eV; for Ohmic contacts, Gold (Au), Palladium (Pd) and Platinum (Pt) are commonly selected. For the simulations, Schottky and Ohmic contacts are considered to be ideal. However, the interaction between the metal and s-SWNT is one important factor which influences the contact properties; this will be discussed in more detail in Chapter 3. For the work presented here, Pd (Φ=5.22~5.6eV) is chosen as Ohmic contact metal and Ti (Φ=4.33eV) for the Schottky contact.

2. Parameters for Detection

Many factors are examined in order to evaluate the quality and sensitivity of detectors. Researchers need to consider the minimum detectable signal, signal to noise ratio (SNR) and the bandwidth of the detectors. One important parameter which reflects the sensitivity and performance of the detector is the noise equivalent power (NEP).

2.1 Noise Equivalent Power (NEP)

The definitions of NEP are varied from each other in different literatures. This is because NEP has many meanings regarding to which parameter is important for one detector [43] [44]. The initial concept of NEP is the optical power which will yield a signal to noise ratio of 1. However, this definition only shows that NEP can be given in a specific bandwidth.

The most commonly used definition of NEP comes from the Federal Standard 1037C (telecom glossary 2000) of the United State Government. "*Noise-equivalent power (NEP) is the radiant power that produces a signal-to-noise ratio of unity at the output of a given optical detector at a given data-signaling rate or modulation frequency, operating wavelength, and effective noise bandwidth. Some manufacturers and authors define NEP as the minimum detectable power per square root bandwidth [$W/Hz^{1/2}$].*" [45]. Another form of NEP definition which is frequently used in industry is also valid [46]: the detector total noise power in a one Hertz bandwidth and it represents the minimum detectable signal power at a unity signal-to-noise ratio. From this point of view, NEP is the noise floor of a detector, normalized to a 1Hz bandwidth, and the smaller the NEP, the lower noise power, and the higher the sensitivity the detector has.

For broad band THz detection as we present here, NEP values of $1pW/Hz^{0.5}$ or better are desired, this is discussed in more detail below:

Figure 2.3 (upper left) shows the blackbody radiation at different temperatures. Radiation power peaks in optical region and is low in infrared and THz spectral regions. The total power in THz spectral region is approximately 100,000 times less than in infrared spectral region. For a given temperature, as shown in Figure 2.3 (upper right), the radiation power will decrease at low frequency region. For THz detectors, the operating frequency is from 0.1-10 THz, which is highlighted in blue color. In this region, the radiation power is almost linear as a function of frequency. During the imaging or detecting process, background noise such as temperature variance can disturb and reduce the sensitivity of the sensor (degrade Signal to Noise ratio, S/N). In Figure 2.3(bottom), the temperature noise is converted into noise equivalent temperature NEΔT for y axis. For broad bandwidth detection such as 100GHz, in order to keep NEΔT under 0.1K, NEP should less than 1pW/Hz$^{0.5}$ over a wide spectral region.

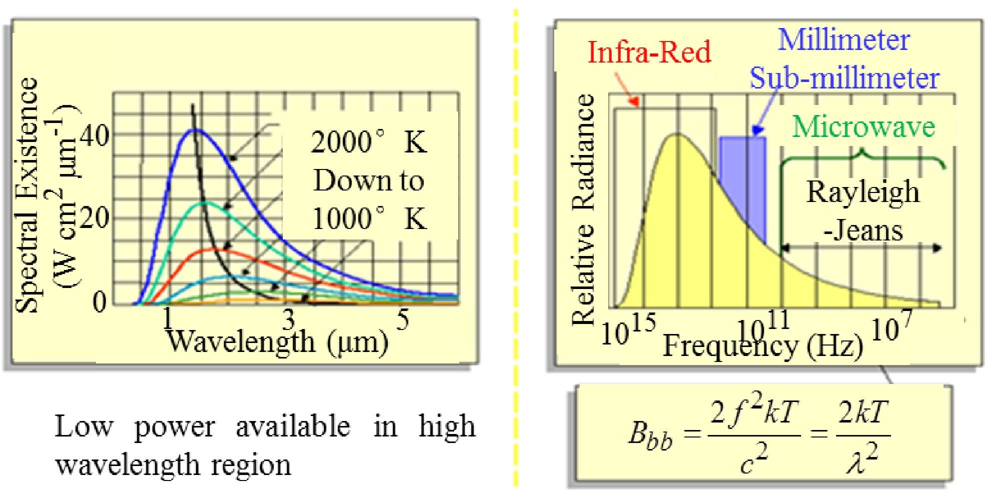

Figure 2.3 (upper left) Blackbody radiation at different temperature, (upper right) Relative Radiance vs. frequency; (bottom) Noise equivalent temperature vs. NEP at different bandwidth

Figure 2.3 (cont'd)

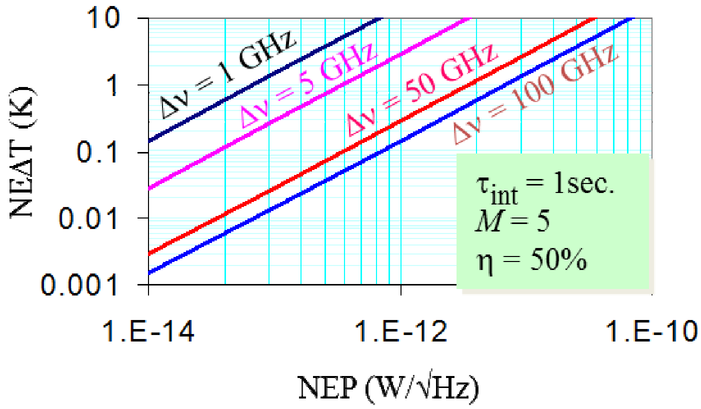

2.1.1 Mathematical Equations for NEP Prediction

Different detectors have different ways of calculating NEP and related parameters. For Schottky diode direct RF detectors, NEP can be calculated by applying the following equations [46]:

$$NEP = \frac{V_n + V_{1/F}}{\beta_V} \tag{2.3}$$

$$\beta_V = \frac{\gamma}{2} \frac{R_d\left(1 - |\Gamma|^2\right)}{\left(1 + R_s / R_d\right)^2 \left(1 + \left(f / f_{ci}\right)^2\right)} \tag{2.4}$$

$$f_{ci} \equiv \frac{\left(1 + R_s / R_d\right)^{1/2}}{2\pi C_j \left(R_s R_d\right)^{1/2}} \tag{2.5}$$

$$V_n = \left(4 k_b T_B \left(R_s + R_d\right)\right)^{1/2} \tag{2.6}$$

$$V_{1/F} = \left(\frac{A \times \left(R_s + R_d\right) V_{ds}{}^2}{F}\right)^{1/2} \tag{2.7}$$

According to equation 2.3, NEP is related to two parameters: detector's voltage noise (numerator) and voltage sensitivity (denominator), those other terms will be explained in the next section along with the small signal circuits.

In Schottky diode detectors, for example, there are several types of noise: thermal noise V_n, flicker noise $V_{1/F}$, and shot noise. Thermal noise is also called Johnson–Nyquist noise, which is generated by the thermal agitation of charge carriers inside the conductors and semiconductors, no matter whether there is a bias or not. Thermal noise can be calculated by using equation (2.6), for a certain Schottky diode with certain bias, the series and junction resistance (details will be explained in next section) has already set, and the thermal noise is approximately white, which means it remains constant through the whole frequency spectrum and cannot be ignored during the calculation. Flicker noise is a type of electronic noise which is also called *1/f* noise; the accurate function of flicker noise is $1/f^a$, where "a" is very close to 1. It is generated due to the imperfection of the electronic devices such as impurities, crystal defects and contaminations in the materials. The noise pre-factor or noise amplitude coefficient "A" in equation (2.7) for CNT Schottky Diode depends on the material as well as the quality of the contact and can range from 10^{-9} to 10^{-15} Ω^{-1} [47][48], for Ti-CNT contact, A is approximately equal to 10^{-15} Ω^{-1}[48], which is used in our simulation process. Note that at high modulating frequencies thermal noise dominates and flicker noise can be ignored. However, at low modulating frequencies (under several KHz), flicker noise is dominant in most devices [49]. Note, in equation given, the frequency F represents the modulation frequency (≈1 kHz) which is common for CMOS based devices, but not the signal frequency (THz frequency). Shot noise is usually generated due to the carriers going through the barrier. Although it is a wideband domain noise, while comparing with thermal and flicker noise as well as its equation, it is relatively small and can be ignored in the calculation of NEP values [49].

The intrinsic frequency or cut-off frequency f_{ci} represents the highest frequency that the sensor can detect. As shown in equation (2.5), the intrinsic frequency is related to the series and junction resistance as well as junction capacitance of the Schottky diode detector. The value of f_{ci} varies as a function of voltage since junction resistance is changing with the applied bias. I-V curve of Schottky diode shows that junction resistance decreases as the bias voltage increases. For some cases, junction resistance can be several factors lower than series resistance, which turns out that the junction resistance can be ignored in calculating f_{ci}, and equation (2.5) can be simplified to equation (2.8):

$$f_{ci} = \frac{1}{2\pi R_s C_j} \tag{2.8}$$

Equation 2.8 can only be used to find the maximum operation frequency of the detectors, and it cannot plugged into equation (2.4) or equation (2.3). One reason is that the junction resistance varies as a function of bias voltage, and it is larger than series resistance at low voltages.

Equation (2.4) provides a certain way of calculating voltage sensitivity β_V, which represents the detected voltage divided by the power absorbed in the diode. β_V is strongly dependent on the curvature coefficient γ, and mismatch losses ($1-|\Gamma|^2$) between antenna and the Schottky diode. The resistance of single-wall semiconducting CNT can range from hundreds of KΩ to a MΩ. Broad band antennas having such high impedance are not practical to design. Thus matching of CNT Schottky diodes to antenna elements is a challenge. The curvature coefficient γ is a measure of the nonlinearity of the diode current–voltage (I–V) characteristic and is given by the ratio of the second derivative of the diode I–V characteristics to its 1st derivative. For Schottky diodes,

$\gamma = q/nkT$, where k is the Boltzmann constant and T is the temperature (Kelvin). The maximum possible value of γ for Schottky diodes at room temperature is close to 40. To achieve maximum voltage sensitivity, apart from maximizing non-linearity, good impedance match between antenna and the Schottky Diode is needed. Typical impedance of the antenna can range between 25 to 100 Ohms. For direct impedance matching, the diode is required to have impedance in this range. As mentioned in the previous chapter, although semiconducting CNTs' resistance is high, reducing the resistance of CNT Schottky Diode by shortening the CNT length and connecting parallel CNTs are two promising ways to effectively reduce the impedance of the diode necessary for better impedance matching [42].

Furthermore, in order to minimize the NEP (improve sensitivity), one need to decrease the noise originating in the diode. The small signal circuits of CNTs Schottky Diode can assist to examine all of these parameters.

2.2 Small Signal Circuit

One way to determine all the parameters being used in equation (2.7) through (2.8) is using the small signal circuit of CNT Schottky diode THz detector (Figure 2.4). Note that this is a simplified diode equivalent model which only consists of junction resistance and junction capacitance. The inductance of CNTs is ignored since some literatures claim that the values of magnetic and kinetic inductance are around 1pH/μm and 1nH/μm [50] [51], and the length of CNT in our simulation is 500nm with 1~2nm for diameter, which means that the effective impedance of the inductor will be negligible in comparison to series and junction resistances.

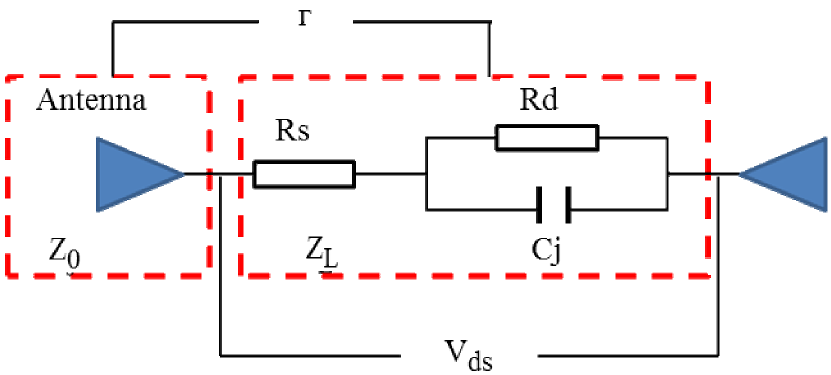

Figure 2.4 Small signal circuits for of CNT Schottky diode THz detector

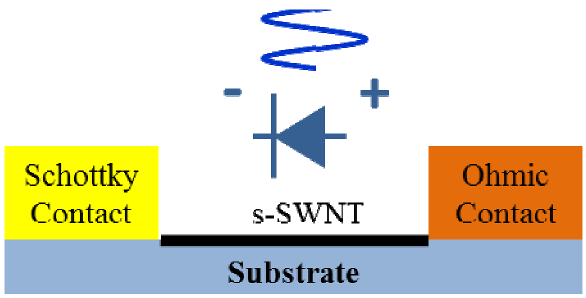

Figure 2.5 Schematic picture of a real CNT Schottky diode THz detector

2.2.1 Components

In order to obtain a better understanding of those parameters in the small signal circuit, a schematic of real device is shown in Figure 2.5 for comparison.

R_s is the series resistance of the CNTs Schottky diode. In conventional Schottky diodes, the lumped series resistance should include the resistance between the semiconductor and the substrate. However, in a CNT Schottky diode, majority carriers flow along the tube under certain bias, and negligible amount leaks into the substrate. Here the series resistance is equal to semiconducting CNT intrinsic resistance plus the Ohmic contact resistance:

$$R_s = R_{CNT} + R_{Ohmic} \tag{2.9}$$

In theory, CNTs are 1D material and their resistance has been proved to follow quantum mechanism, and only ballistic resistance exists for a short CNT [52]. In practice, however, CNTs have defects and impurities which introduce photon scattering and lead to increase in the resistance value [53]. For a 3μm long semiconducting CNT, the series resistance R_S is around 228kΩ, and for 6μm long semiconducting CNT, R_S is around 420 kΩ [54]. Using this information, the intrinsic resistance for 500nm s-SWNT is expected to be approximately 30 kΩ. This value will be used in further calculations as discussed ahead. Ohmic contact resistance depends upon the type of metal used and the quality of the contact. Details on the choice of metals for Schottky and Ohmic contacts were discussed in Chapter 1. Here we only use the lowest Ohmic contact resistance, which is R_{Ohmic}=12.9 kΩ (provided by contact with Palladium, see details in Chapter 1).

R_d is the Schottky contact junction resistance and it changes with the applied bias. This resistance is related to the barrier height at the contact interface. A forward bias lowers the Schottky barrier, leading to increase in current (by the terms of thermionic and tunneling current). Like R_{Ohmic}, junction resistance R_d also relies on the quality of the contact. A high quality contact will effectively reduce the junction resistance for an over a certain bias range. On the other hand, a low quality contact increases the junction resistance. In the calculations here, it is assumed that the Schottky contact is perfect and only the barrier height is the dominant factor contributing to junction resistance value.

The junction capacitance C_j of CNTs Schottky contact represents the electrostatic capacitance plus CNTs unique quantum capacitance. The electrostatic capacitance can be calculated through conventional Schottky contact junction capacitance by applying equation (2.10)

$$C_j = A\left[q\varepsilon N_A / 2\left(\phi_{bi} - V\right)\right]^{1/2} \quad 2.10$$

Where A is the contact area, ε is the dielectric constant of s-SWNT which is approximately equal to $5\varepsilon_0$, q is the electron charge 1.602×10^{-19} C, N_A is the holes concentration for p-type CNT, and □$_{bi}$ is the build in potential at the junction, V is the external bias. Some researchers have shown that the value for CNTs Schottky contact electrostatic capacitance is around 10aF/μm [42] [51], which is due to the small contact area between CNTs and metal. The quantum capacitance is calculated by means of the density of states of the semiconducting CNTs, which is connected in series with the electrostatic capacitance, and the value is around hundreds of aF/μm [51] . The minimum total junction capacitance measured is ~1aF [54] [55] and can vary from several 1aF to 15aF [51]. In this work, smallest junction capacitance given in literature was chosen to calculate the NEP values.

The mismatch loss is another important parameter which directly determines the voltage sensitivity and in turn improves the value of NEP. As shown in Figure 2.4, the mismatch is basically due to the huge resistance differences between source (antenna) and the diode. For most of the broadband antennas, the impedance Z_o ranges from 50Ω (BOW-TIE antenna) to ~180Ω (slot antenna). The impedance of CNT Schottky diode depends on junction and series resistance which typically have the value of tens of KΩ or more. By applying equation (2.11),

$$\Gamma = \frac{Z_{in} - Z_o}{Z_{in} + Z_o} \quad 2.11$$

Reflection coefficient Γ between the antenna and the diode can be calculated. By using the values for the antenna and diode impedance, it is clear that most of the power will be reflected back. This is especially true at lower bias voltages where the diode impedance is significantly high. At higher bias voltages the reflection coefficient decreases, but still remains large. One possible way of reducing the reflection is by reducing the effective impedance of the Schottky diode. This can be achieved by aligning multiple CNTs in parallel. However, the negative impact of this approach is that the effective junction capacitance increases. Our goal here is to find the optimal parameters which can provide a minimum value of NEP for CNT Schottky diode having multiple CNTs in a single device.

2.2.2 Parameters for simulation

Based on the discussion above, the parameters for simulation process can be determined. Table 2.2 shows those values for each of the parameters.

Table 2.2 Parameters used for calculation

L	R_{CNT}	R_{Ohmic}	$R_s = R_{CNT} + R_{Ohmic}$	R_d	C_j	Z_o	F	A	Γ
500nm	30kΩ	12.9 kΩ	42.9 kΩ	--	1aF	150Ω	1kHz	$10^{-15}\Omega^{-1}$	--

R_d and Γ are not given here since these two need to be determined by simulating the I-V curve of CNTs Schottky diode and the antenna impedance matching, and the I-V characteristic will be discussed in the following section.

3. I-V Characteristic of CNTs Schottky Diode

The I-V Characteristic of Schottky Diode is shown in Figure 2.1 and the current is based on the transport of majority carriers. Because of the existence of depletion region and barrier height at the junction, the I-V curve performs the rectification behavior. Although in Schottky Contact the carriers transport mechanism is different from that of p-n junction, they have the similar form for I-V relation expression (2.1), as well as the reverse saturation current (2.2). By studying and simulating these equations, junction resistance can be calculated. If looking into details of the derivation of these expressions, one will notice that they are based on the thermionic emission current theory [56]. Moreover, the thermionic emission current is not the only contribution to the total current and there are also other two types of current which can exist depending on certain conditions of the Schottky contact. One is diffusion current, the other is tunneling current. Before starting the simulation of NEP, some simulation work of those three types of current need to be carried out as to which is the dominant current in the I-V characteristics.

3.1 Thermionic Emission Current

As explained in [56], the thermionic emission theory is a semi-classical approach which describes the transport of carriers through a semiconductor-metal contact. Also, there are three assumptions are followed to deduct the equations. In this theory, only carriers which have the energy equal to or larger than the top of the Schottky Barrier Height φ_B can go across the Schottky barrier and form the current, as shown in Figure 2.6

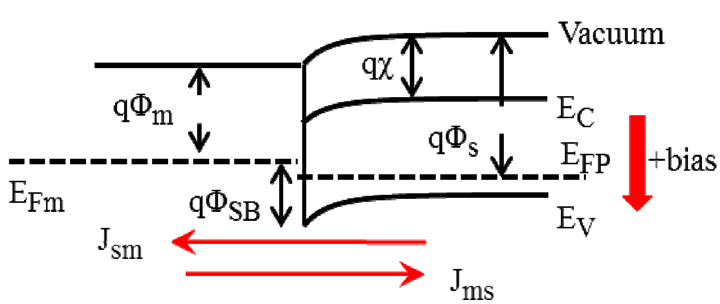

Figure 2.6 Simple diagram of the forming thermionic emission current

The Schottky Barrier Height for p-type semiconductor-metal contact is given by equation (2.12)

$$\varphi_{SB}=E_g/q+\chi-\varphi_m \qquad 2.12$$

where E_g is the bandgap of the semiconductor, χ is the electron affinity of semiconductor, and φ_m is the work function of the metal. Following the derivation process of thermionic emission current in [57], the I-V Characteristic can be expressed in equation (2.13)

$$J = J_{s\to m} + J_{m\to s} = A^{*}T^{2}e^{\frac{-q\phi_B}{nk_bT}}\left[e^{\frac{qV}{nk_bT}} - 1\right] \qquad 2.13$$

Where T is the temperature, φ_B is the barrier height, k_b is the Boltzmann constant, q is the electron charge, V is the applied bias, n is the ideality factor of the diode, which is between 1~2, and A^* is the effective Richardson constant and

$$A^{*} = \frac{4\pi q m^{*} k_b{}^{2}}{h^{3}} \qquad 2.14$$

where m^* is the effective carrier mass, h is the plank Constant. Comparing (2.13) with equation (2.1), it is obvious that the thermionic emission current is the dominant factor. Note that (2.14) can also be expressed in form of effective density of states in the conduction/ valence band.

3.2 Diffusion Current

Generally speaking, the thermionic emission current can be sorted into the diffusion –drift theory, and in [57], and it is claimed that the diffusion current and thermionic current have similar equation form. One difference between them to note is that the general diffusion theory requires the condition which depletion width is much larger than the carrier mean free path. For p-n junction, the depletion region is wide enough thus the diffusion equation can be applied. However, for Schottky Contact, the depletion width is smaller, so thermionic current starts to dominate. For CNTs Schottky Contact, due to the quantum properties of ballistic electron transport in CNTs and high carrier concentration, the depletion width is even much thinner than regular Schottky Contact. Thus, the diffusion theory which works for p-n junction doesn't fit this condition and only the thermionic is required. In the simulations, only the thermionic emission part instead of the whole diffusion-drift theory is considered.

3.3 Tunneling Current

Classic theory of tunneling current is based on three dimension (3D) materials, with highly doped semiconductor contact with metal, and the depletion region is thinner due to the high carrier concentration in the semiconductor part. Usually the tunneling happens when the depletion width is around 3nm, and the tunneling coefficient depends on the barrier height φ_B to the power of 1.5. Figure 2.7 shows the schematic of tunneling current in band diagram.

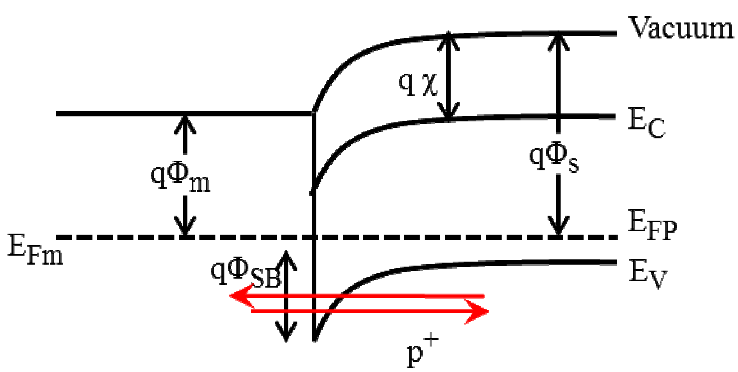

Figure 2.7 Simple diagram of the forming tunneling current

However, CNTs are 1D materials and the tunneling theory is based on the quantum analysis which is quite different from that of classic model. For calculating the tunneling current, the non-equilibrium Green's function, which solves Schrödinger equation under non-equilibrium conditions, is applied and the tunneling current can be given in Landauer–Buttiker Formula:

$$J = \frac{4e}{h}\int_{\phi_{bi}+V}^{\phi_B} T(E)\left[f_{sc}(E-V) - f_m(E)\right] \quad 2.15$$

Where φ_B is the Schottky barrier height, φ_{bi} is the build-in potential which is the different between metal work function and semiconductor valence band. f_{sc} and f_m are the Fermi distributions in semiconductor and metal, V is the applied voltage on the contact, and E represents the energy of the carrier which contributes to the current. The integration region is from the bottom of the conduction (valence) band to the top of the barrier height. *T(E)* is the transmission coefficient of carrier which tunneling through the barrier, and can be calculated by Wentzel–Kramers–Brillouin (WKB) approximation as given in equation (2.16)

$$T(E) = \exp\left(-2\int_{z_i}^{z_f} k_z(z)dz\right) \quad 2.16$$

Where z_i and z_f are the classical turing points, and $k_z(z)$ is the parallel momentum which is linked with the energy-k function. The classical turning points z_i=0, and z_f represents the point where carrier's energy is equal to the energy on the Schottky barrier potential curve. Following the derivation in [58], the transmission coefficient for CNT Schottky contact can be rewritten as equation (2.17), as well as its adhesion equations (2.18), (2.19) and (2.20)

$$T(E) = \exp\left(-\int_0^{z_f}\left(\frac{2E_g}{3dV_{pp\pi}}\times\sqrt{\left(\frac{3dV_{pp\pi}k_n}{E_g}\right)^2 - \left(\frac{E-qV(z)}{E_g/2}\right)^2}\right)dz\right) \quad 2.17$$

$$k_n = \frac{|3n-n+m|}{3R} \quad 2.18$$

$$E_g = \frac{V_{pp\pi}d}{R} \quad 2.19$$

$$R = \frac{d}{2\pi}\sqrt{3\left(n^2+m^2+nm\right)} \quad 2.20$$

E_g here is the bandgap of CNT, d=0.142nm is the C-C bond distance, $V_{pp\pi}$=2.97eV is the C-C bonding energy. R is the CNT's radius. $qV(z)$ is the Schottky barrier potential function, z_f is given by making $E=qV(z_f)$.n and m are CNTs chirality. The Schottky barrier potential function can be found by following the conventional Schottky barrier potential diagram calculation in [59]. Note that in [59] the zero potential is chosen at the valence band of the semiconductor. In order to simplify the simulation, the zero potential is chosen at metal Fermi level, which yield equation (2.21)

$$qV(z) = q\left\{-\frac{qN_A}{\varepsilon_r\varepsilon_0}\left[\frac{z^2}{2} - z\sqrt{\frac{2\varepsilon_r\varepsilon_0}{qN_A}\left(\phi_{bi} - V\right)}\right] - \phi_B\right\} \quad 2.21$$

Note that equation (2.17) is generated for electrons, in our case, the majority carriers are holes, and (2.21) is the potential function for p-type semiconductor-metal contact. In order to fit into equation (2.17), we simply reverse the sign in (2.21) and it becomes potential function for electrons, (2.22), this manipulation will not change the transmission coefficient since the mechanism is all the same.

$$qV(z) = q\left\{\frac{qN_A}{\varepsilon_r\varepsilon_0}\left[\frac{z^2}{2} - z\sqrt{\frac{2\varepsilon_r\varepsilon_0}{qN_A}\left(\phi_{bi} - V\right)}\right] + \phi_B\right\} \quad 2.22$$

N_A is the charge density of CNT and ε_r=5 is the dielectric constant of semiconducting single-wall CNTs. With those equations above, tunneling current through CNT Schottky Barrier can be calculated and then analyzed.

3.4 Comparison of Thermionic and Tunneling current

Based on different types of currents that can contribute to the I-V characteristic, we need to find which type is the most dominant current. Only focusing on and comparing those equations cannot give a quantitative analysis of each type of current, Thus, we need to set real and practical values for these equations and compare the I-V curve systematically.

3.4.1 I-V Curve of Thermionic Current

Table 2.3 gives real values of a CNT as well as Schottky contact barrier height that are needed to simulate the thermionic emission current:

Table 2.3 Values for simulating thermionic emission current

φ_B	n	T	m^*	q	k_b	h	m_0
0.85V	1.5	300K	$0.3m_0$	1.6×10^{-19}C	1.38×10^{-23}	6.626×10^{-34} J•s	9.1×10^{-31} kg

The CNTs metal contact area is another parameter that needs to be examined, and equation (2.13) only gives the current density of thermionic current. There are three typess of contacts between CNT and metals mentioned in Chapter 1: side contact, end contact and buried contact. Buried contact shows lower junction resistance than the other two. According to several literatures, the contact length ranges from 1~2μm. Here a length of 2μm for buried contact was chosen. This is also used to fit simulations of tunneling current in the next section. After plugging in those values in Table 2.3, the thermionic current simulation I-V relation is provided by equation (2.23), and I-V curve is generated and is shown in Figure 2.8

$$I=1.809\times10^{-13}\times\left(\exp(\frac{V_{sb}}{1.5\times0.026})\text{-}1\right) \qquad 2.23$$

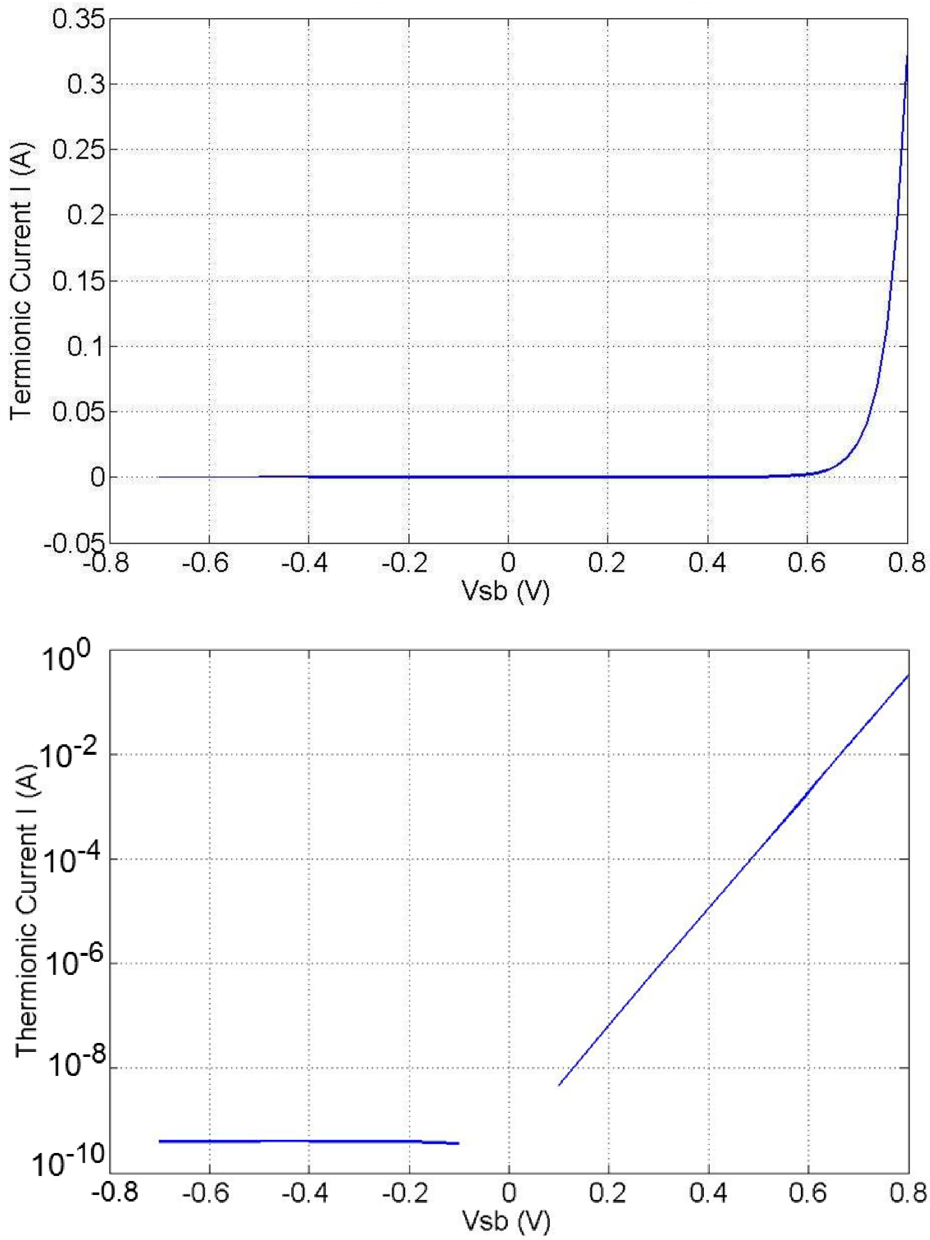

Figure 2.8 Simulation results for I-V characteristic of thermionic emission, lower figure illustrates current in semilog scale

Figure 2.8 shows the CNT Schottky diode has the rectification behavior. The current starts to increase rapidly after bias exceeds the value of build-in potential. It also shows the I-V curve in log scale (bottom), in which the reverse saturation current is clearly shown and is around 10^{-10}A.

3.4.2 I-V Curve of Tunneling Current

In order to make the tunneling current reasonable compared to the thermionic current, s-SWNT with chirality of (11, 6) is used. It has the most close holes effective mass [60], and the holes charge density [61]. Table 2.4 shows the parameters needed to simulate tunneling current.

Table 2.4 Values for simulating tunneling current

N_A	E_g	d	φ_B	ε_r
~$10^{16}cm^{-3}$	~0.61eV	~1.3nm	~0.85eV	5

Note that there is no precise I-V equation for the tunneling current, but Figure 2.9 show the I-V relation for tunneling theory.

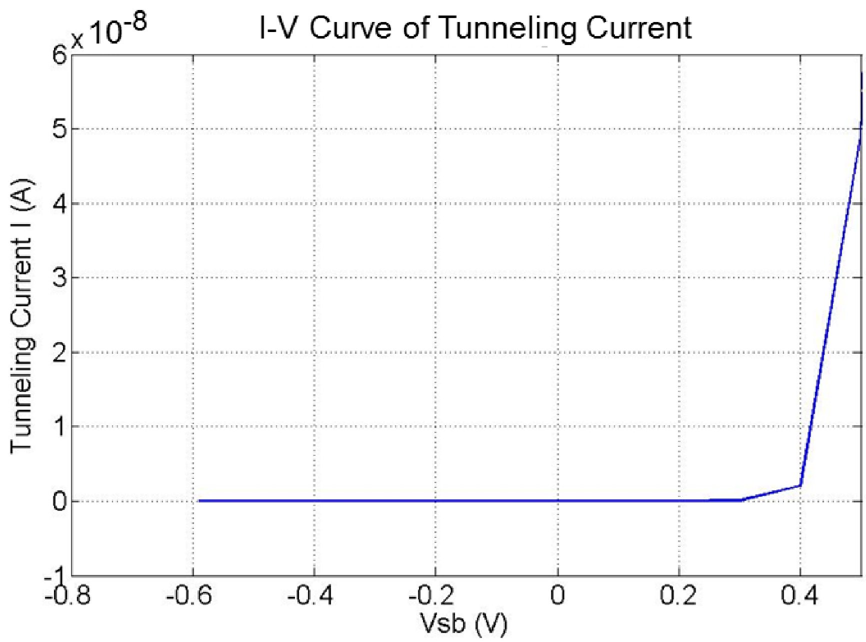

Figure 2.9 Simulation result of I-V characteristic of tunneling, lower figure illustrates the current in semilog scale

Figure 2.9 (cont'd)

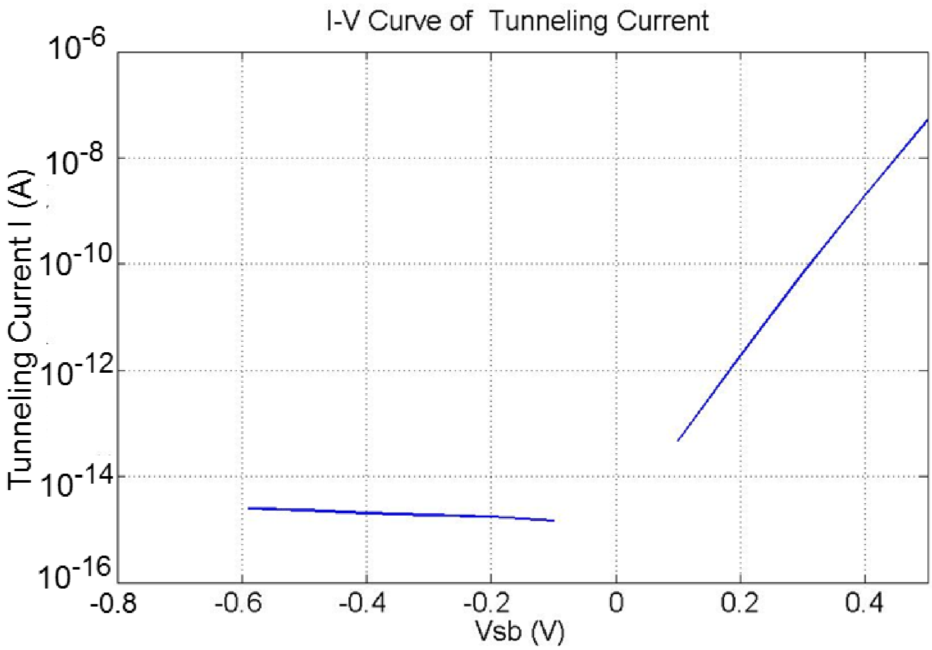

As shown in Figure 2.9, the tunneling current also performs the rectification behavior, and we can predict that if the value of barrier height decreases (also means there will be thinner depletion width), the I-V curve will tend to follow Ohm's law.

3.4.3 Comparison of Thermionic and Tunneling Current.

The thermionic and tunneling current in CNT Schottky can exit at the same time, it is possible that one of them is the dominant source for the total current and also both can be at the same weight to contribute the total current. Figure 2.10 shows that thermionic current and tunneling current I-V characteristics. Figure2.10 (a) shows that if the ideality factor n=1, although both type of current have the same shape and increasing trend, thermionic current is several factors smaller than tunneling current. However, for most of fabricated CNTs Schottky diodes in literatures, the ideality factor n ranges from 1.5-2 [42]. As shown in Figure 2.10 (b), when n=1.5, thermionic current becomes the dominant current and is several factors larger than tunneling current. Thus tunneling current can be ignored. This is only valid at low bias, but this is the proper range for efficiently operating the detector. At higher bias, although junction resistance is small, the current can burn down the semiconducting CNT. Also at higher bias currents the flicker noise is high (see equation (2.7)), and decrease the sensitivity of the detector. As mentioned above, the tunneling current will increase and follow the Ohm's law if the barrier is lower and thinner. This means that applying gate voltage through top or back gate electrodes, tunneling can be switch on and off. The higher the gate voltage, the larger the tunneling current will be [62]. Since there is no gate voltage applied on our CNT Schottky diode detector, the tunneling current can be treated as at the "turn off" mode. Thermionic current is the dominant current in our detector, and other parameters that are needed for calculation of NEP can be found through thermionic current I-V characteristic.

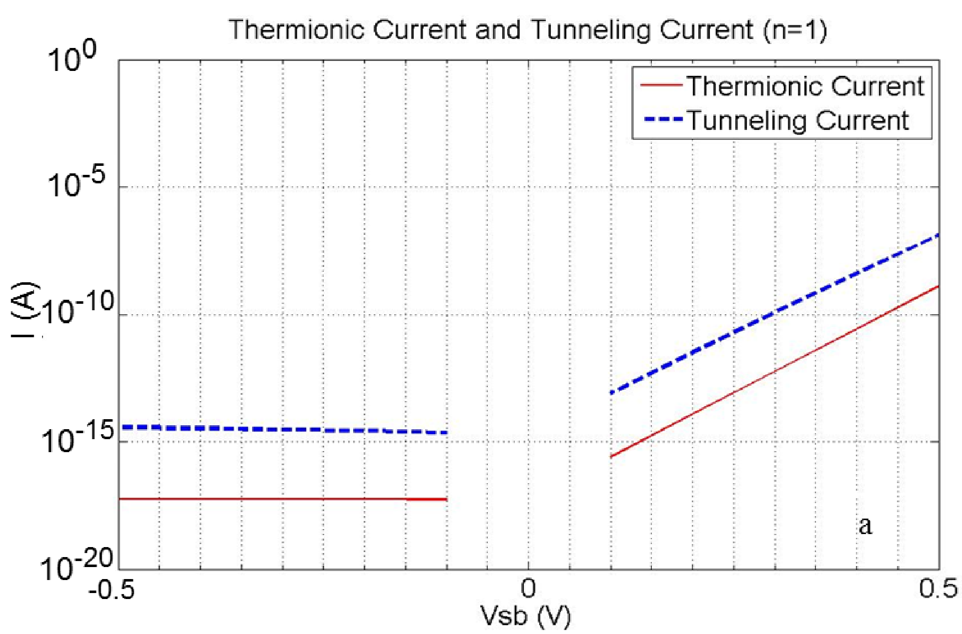

Figure 2.10 Comparison of thermionic emission I-V curve with tunneling I-V curve at n=1(a) and n=1.5(b)

Figure 2.10 (cont'd)

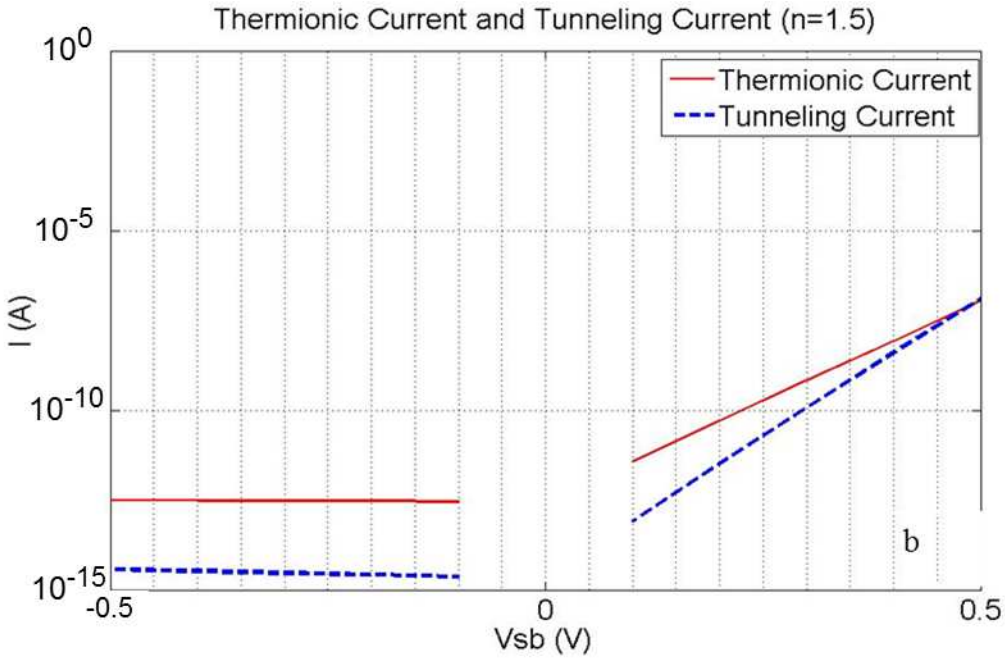

4. Simulation Results

The I-V characteristic of CNTs Schottky diode provides us the possibility of finding junction resistance of the Schottky Contact. Following the simulation process in the last section and plugging the parameters into equations for calculating NEP, one can easily get the results for the lowest NEP that the detector can reach.

Equation (2.3) for NEP calculation requires the noise part and the sensitivity part, and noise part plays an important role of determining NEP. In the first run, the simulation is focused on examining the thermal noise and the flicker noise. Following this, NEP with different parameters configurations will be studied one by one.

Note that in the last section the simulation results show that the thermionic emission current is the dominant part of the total current, especially there is no gate voltage and the ideality factor n=1.5~2. Thus, the I-V relation is only based on equation (2.13).

4.1 Simulation of Thermal and Flicker Noise

By applying equation (2.6) and (2.7) (in (2.7) the *F* is sweeping), and plugging the parameters from table 2.2 and the junction resistance at V_{DS} =0.3V with 1 CNT between the antenna, the thermal and flicker noise versus frequency are calculated, and plotted in Figure 2.11. In this figure, the thermal noise remains constant through the frequency spectrum, which follows the role of white noise. At low frequencies (1-5 kHz), flicker noise is more than one tenth of the thermal noise, which clearly means that it cannot be ignored as mentioned in [42]. For CMOS fabrication process based devices, the modulation frequency *F* is around 1 kHz, which thermal and flicker noise almost equals to each other. This again confirms that the flicker noise is an important factor.

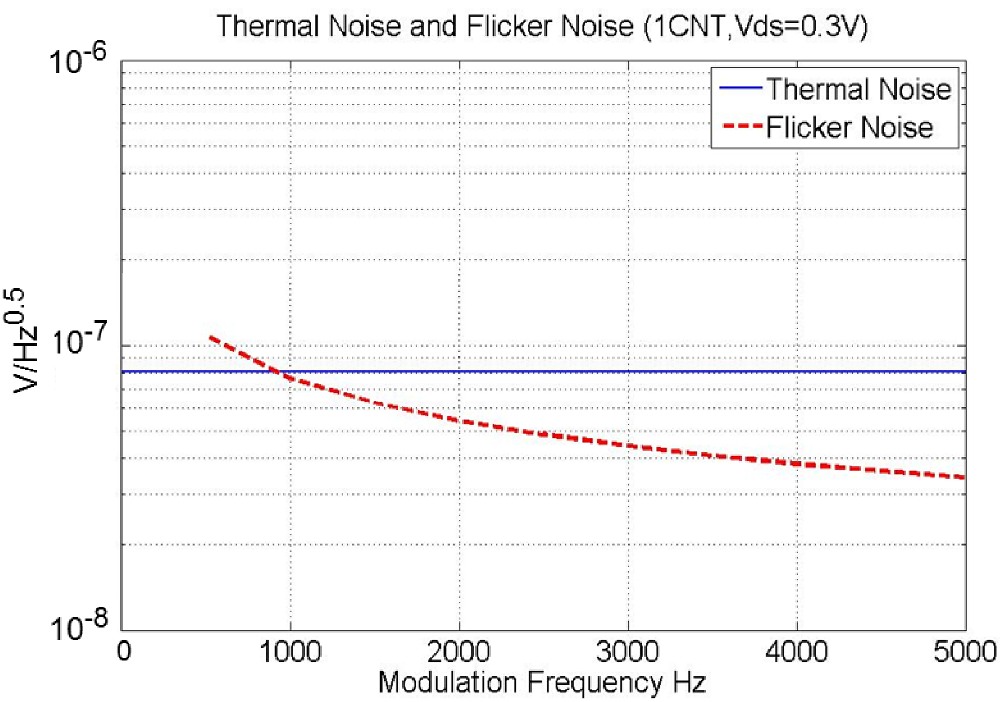

Figure 2.11 Thermal and flicker noise vs. modulation frequency

4.2 Simulation of NEP Changing with Frequency *f*

The goals of the detector is that it is broadband (0.1 – 1THz) and the NEP value is low over this frequency range. NEP with and without mismatch are both simulated and compared. For the first analysis, only one CNT is used in the device model.

4.2.1 Without Mismatch

Simulation for no mismatch is done by following equations (2.3) to (2.7), and other parameters such as R_S and C_j are also included into these equations. The only different is $1-|\Gamma|^2$ is removed from (2.4) in order to realize no mismatch calculation. Figure 2.12 shows the NEP changes with Frequency without mismatch. It is clear that at low frequency (0.1- 4THz), the NEP values are smaller than $1pW/Hz^{0.5}$, except that under higher applied bias (black line). There is also another phenomenon, NEP tends to decrease first and then increase almost through the whole frequency spectrum. This means there should is an optimal bias to achieve minimum NEP, this is probably because at higher bias, the flicker noise which depends on V_{DS} starts to dominate. However, although these results of low NEP is promising, this is not based on the practical, one need to consider the mismatch with antenna, especially for large series and junction resistance of CNTs Schottky diode detector.

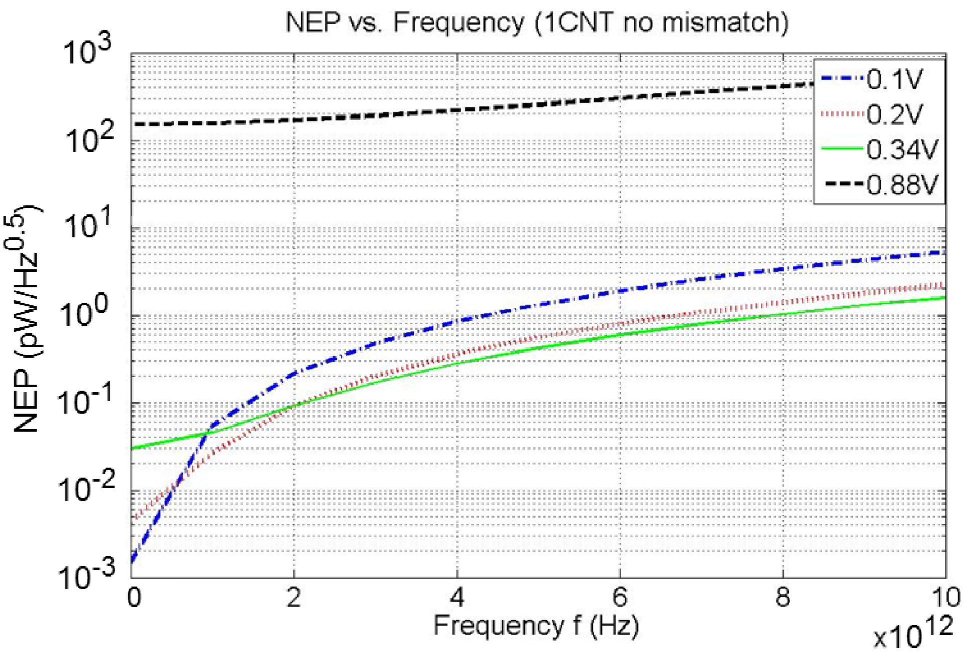

Figure 2.12 NEP changing with frequency without mismatch

4.2.2 Incorporation of Mismatch

Taking the mismatch between antenna and the diode is more practical and useful. According to equation (2.11), the reflection coefficient Γ can be found and $1\text{-}|\Gamma|^2$ is the power going into the diode. Figure 2.13 plots the NEP vs. frequency with the existence of mismatch. At low frequency (0.1-2 THz) NEP is lower than100pW/Hz$^{0.5}$, except that under higher bias. Also, there is a trend for NEP decreasing at first and then increases, which again proves that there should be an optimal bias for the lower NEP at certain frequency. From the simulation results, lowest NEP at 1 THz is approximately 20 pW/Hz$^{0.5}$, when V_{DS}=0.34V. Although this result is better compared to most of other THz detectors, this can still be further reduced, by decreasing the series and junction resistance by increasing the number of CNTs connected in parallel.

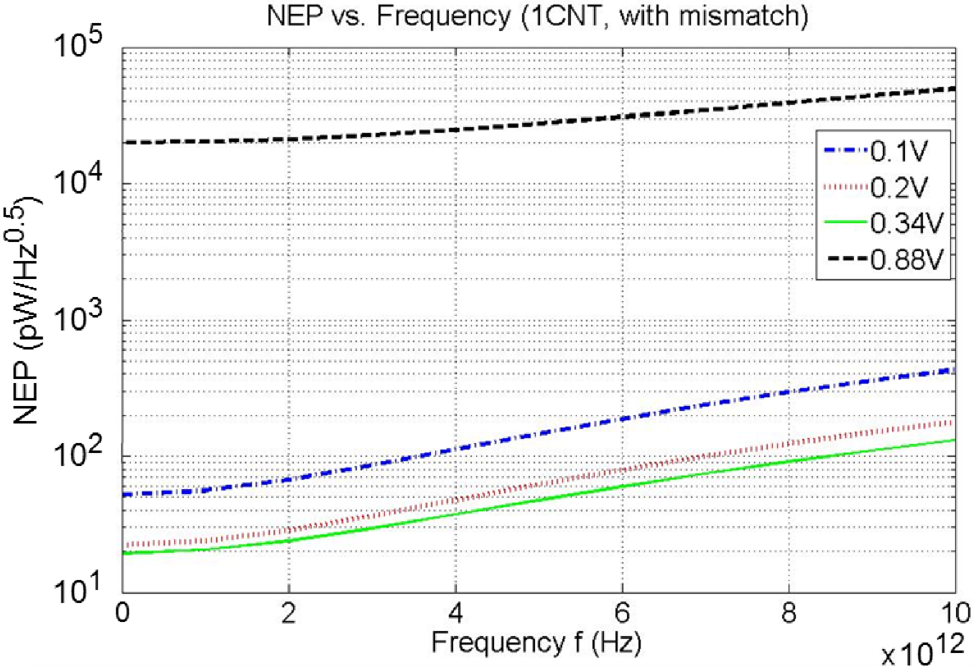

Figure 2.13 NEP changing with frequency with mismatch

4.3 Simulation of NEP Changing with Applied Voltage

As be observed from Figure 2.12 and 2.13, with an increase in applied bias, NEP first decreases and then increases, an optimal voltage should give out the lowest NEP at certain frequency. In order to analyze this hypothesis, NEP is simulated again at fixed frequency 1THz, while changing the applied bias, the result is shown in Figure 2.14. It is clear that NEP in both cases (w/wo mismatch) have the same trend of decreasing then increases. The difference between minimum and maximum NEP is a factor of 3X. Also, the applied voltage for minimum NEP with mismatch is approximately 0.25-0.35V. In the follow on sections, multiple numbers of CNTs connected in parallel between electrodes is discussed.

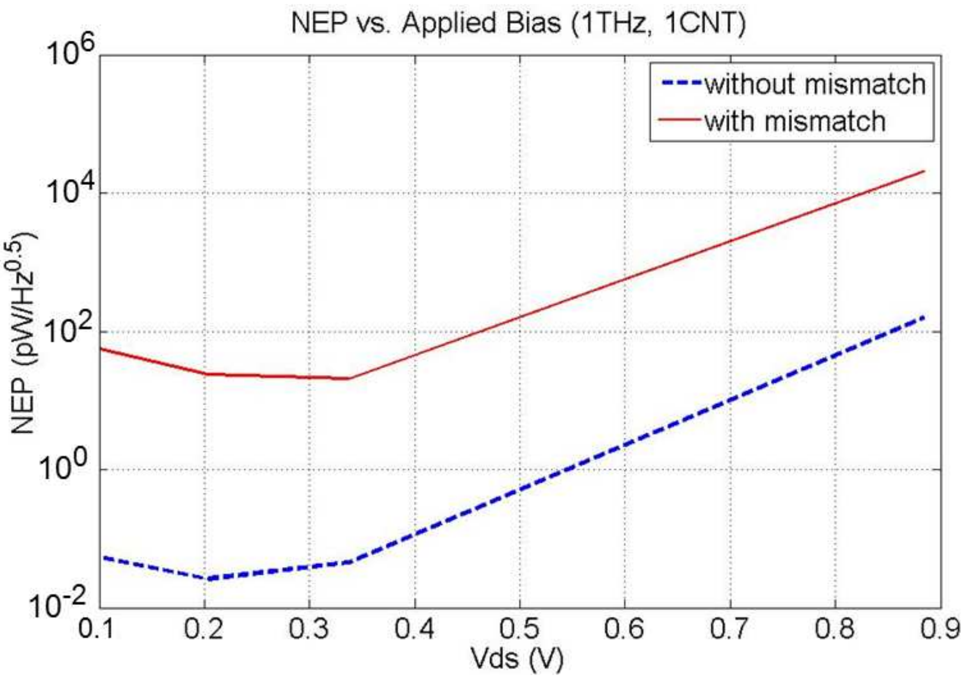

Figure 2.14 NEP vs. applied bias at 1THz with 1CNT

4.4 NEP vs. No. of CNTs Connected in parallel

The way of connecting multiple numbers of CNTs in parallel between electrodes is shown in Figure 2.15 (left) (the metals connecting with CNTs are not restricted to Pd and Al). Figure 2.15 (right) shows the small signal circuit and diode impedance for multiple CNTs. First the simulations are focus on roughly changing the numbers of CNTs, as shown in Figure 2.16. The NEP values in each group have the same trend to increase when frequency is increasing, and each configuration has an optimal voltage which provides the minimum NEP, and this voltage V_{DS} is equal to 0.3V, which is the same optimal value for 1 CNT. Moreover, when the numbers of CNTs are increasing, NEP values under each applied bias are decreasing through the whole frequency spectrum. In addition, the black line which has larger NEP value is shifting down dramatically while CNTs numbers is increasing. This is because the series and junction resistances are decreasing, which in fact improves the mismatch between antenna and the diode and decrease the thermal noise as well as flicker noise. Secondly, NEP for different numbers of CNTs are studied under the optimal bias, it has the same trend of decreasing through whole frequency spectrum. Figure 2.17 shows this result clearly, in which the applied voltage is at optimal value V_{DS}=0.3V. Also, at a certain detection frequency such as 1THz, the NEP for each numbers of CNTs is shown in Figure 2.18, it is shown that the NEP is decreasing quite fast when increasing the numbers of CNTs. Although aligning multiple CNTs will increase the junction capacitance, the reduction of resistances is much faster than the increment of small capacitance (10^{-18}F). From this point of view, the hypothesis that reducing the diode resistance by increasing numbers of CNTs can increase NEP is proved to be correct. However, it is not wise that increasing numbers of CNTs to a huge number, one reason is that CNTs are tend to entangle with each other, and perform metallic property, another reason is more practical, the sharp tips of these antennas which are using to align CNTs cannot hold that many CNTs, especially for Bow-Tie antenna, also the alignment process will not be that accurate to align them parallel, there will be cross points along the CNTs, and this will definitely change the property of the detector.

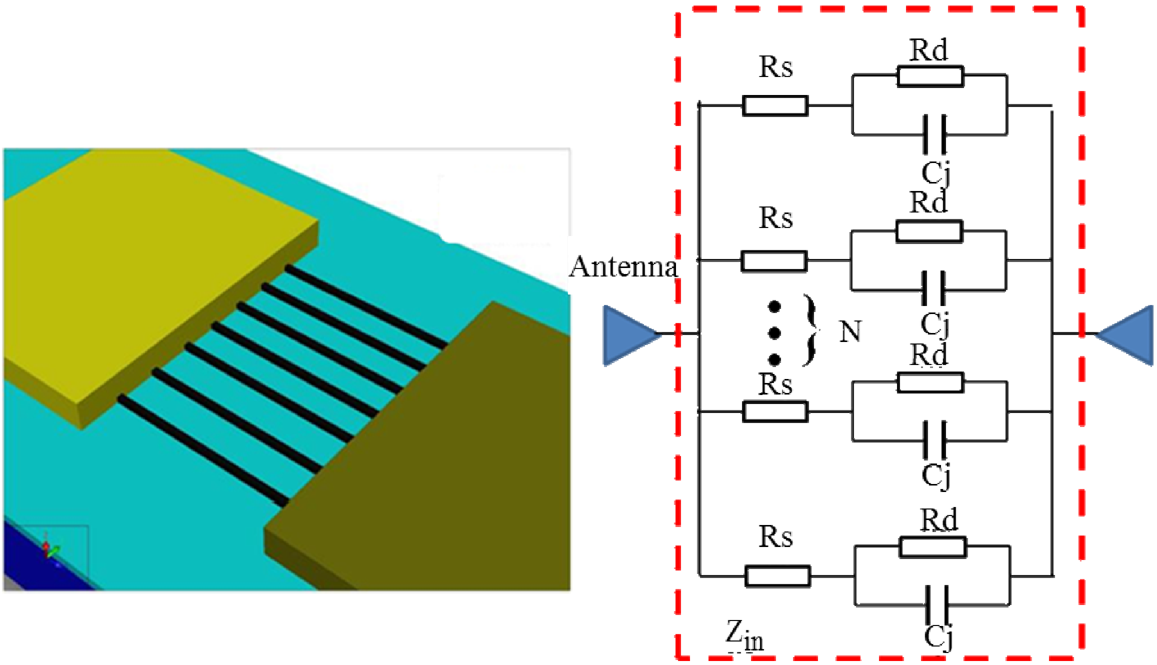

Figure 2.15 Multi number of CNTs connecting the electrodes (left); small signal circuits for the connecting numbers of CNTs (right)

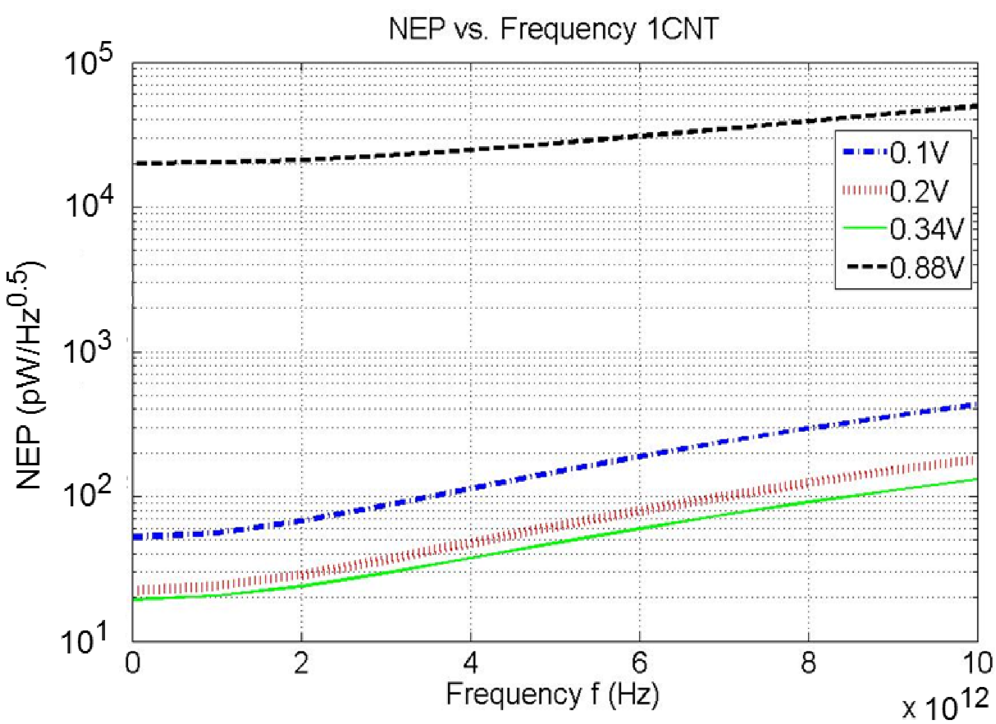

Figure 2.16 NEP vs. frequency with 1CNT (top), 4CNTs (middle) and 16CNTs (bottom)

Figure 2.16 (cont'd)

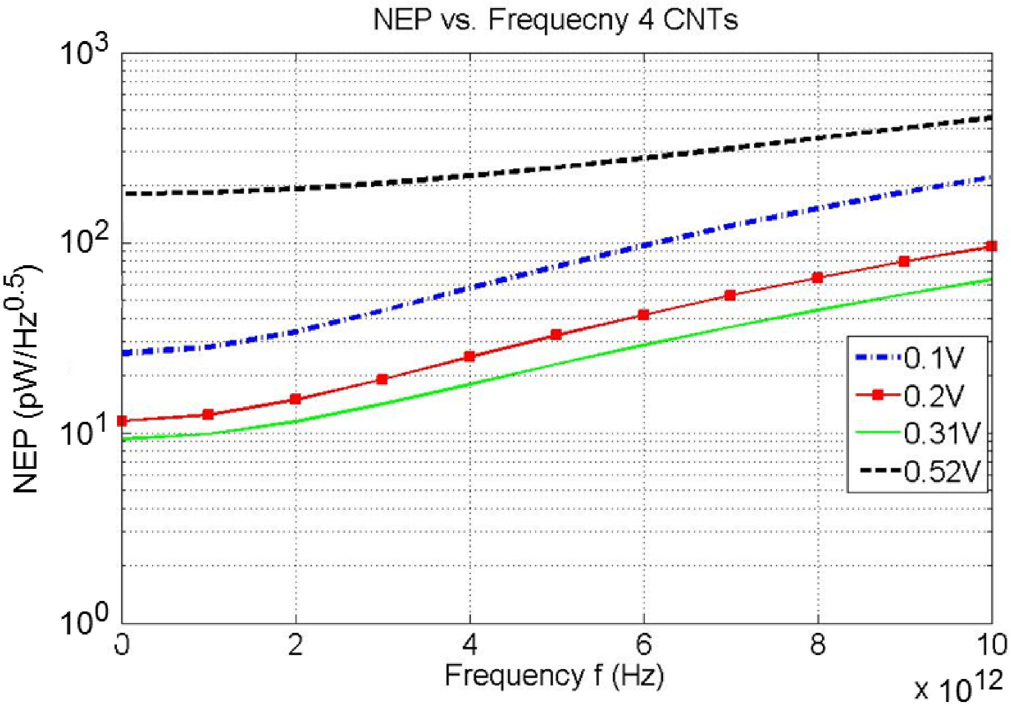

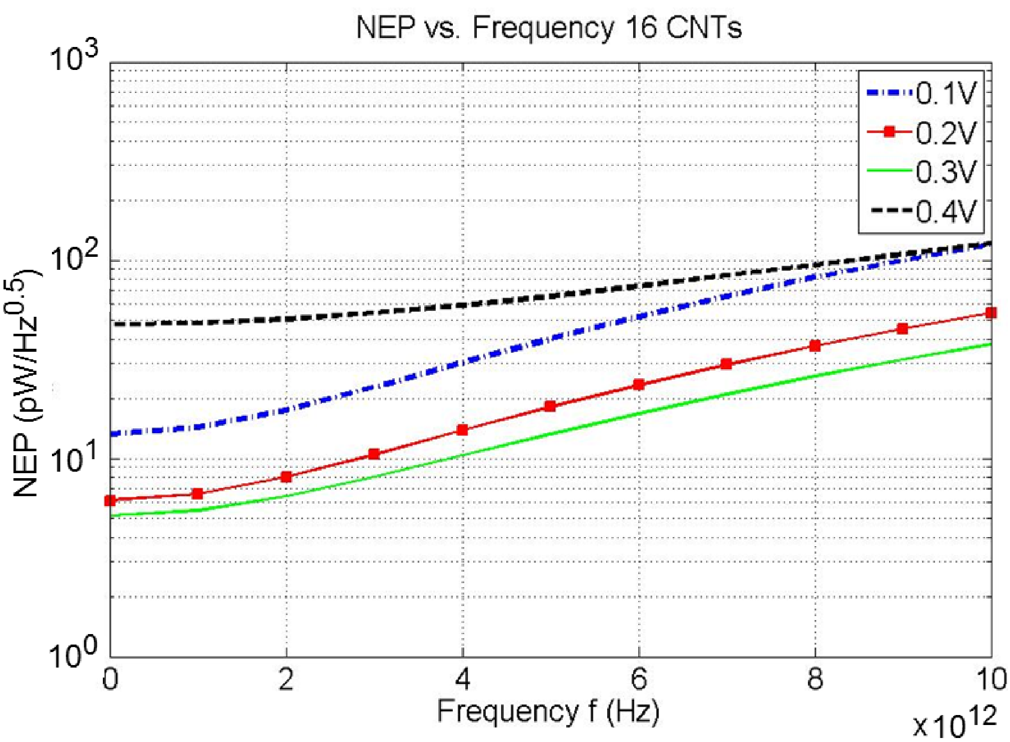

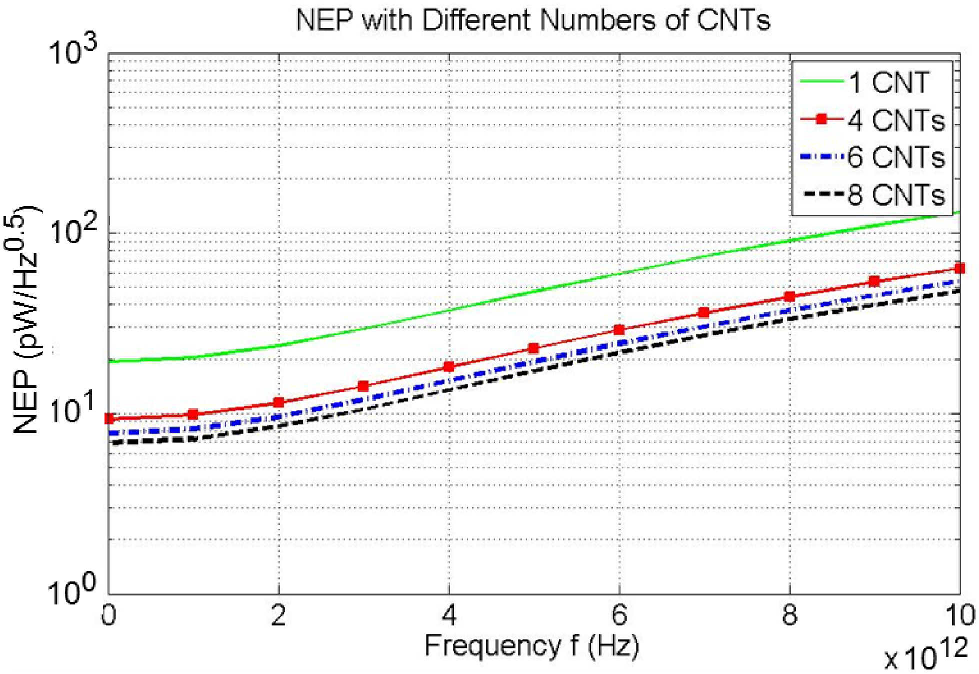

Figure 2.17 NEP vs. frequency at optimal V_{DS}=0.3V with different numbers of CNTs

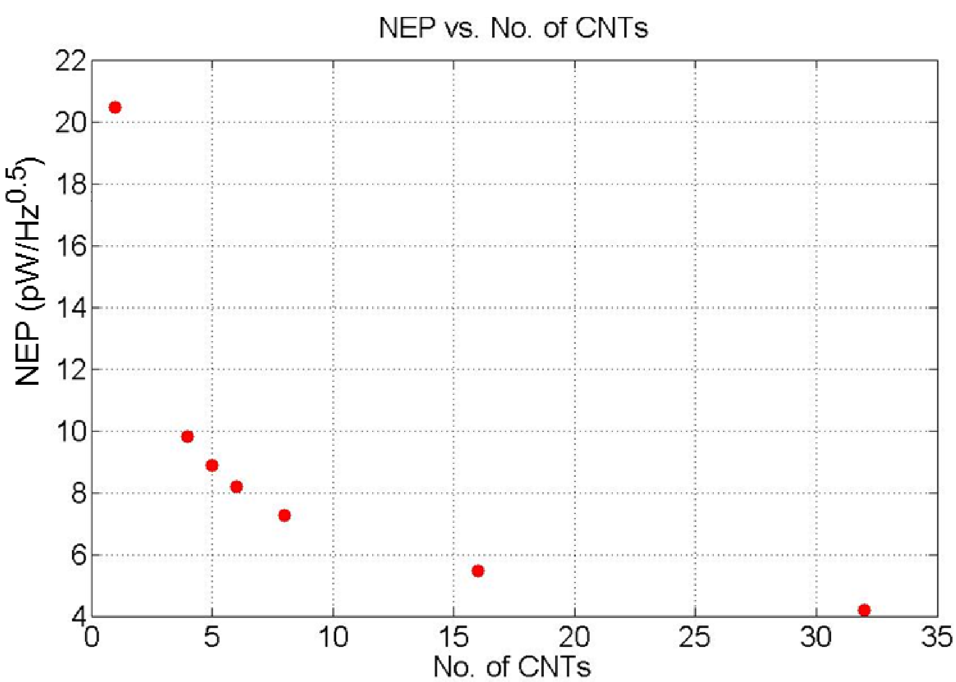

Figure 2.18 NEP vs. numbers of CNTs at 1THz

Basing on the simulation results, the minimum NEP with mismatch at 1 THz can be around

5.5pW/Hz$^{0.5}$, with an optimum bias voltage between 0.25-0.35V and 16 CNTs parallel aligned in the gap. The metal for Schottky contact is Ti and Pd for Ohmic contact, which means that the barrier height is fixed during this simulation. This value can be changed by switching to alternate metals such as Al, Ag and Cr. This NEP value is very close to that of GaAs Schootky diode THz detector, which results in a promising device that provides good sensitivity. The fabrication process of the devices will be discussed in the following chapter.

Chapter 3 Fabrication Process of CNTs Schottky Diode THz Detector

1. Fabrication Introduction

Nowadays, microfabrication process becomes more complicated and the devices feature tends to shrink into nanometer level. Micro electromagnetic wave detectors such as inferred sensors and THz detectors require low loss and large area substrate for high sensitivity and large area imaging. As mentioned in Chapter 1, Sapphire and quartz can be low loss but high cost for large area; glass and SiO_2 are also low loss but require certain semiconductor fabrication process, which increase the cost, too. PET can be a good candidate for large area and low cost, and it is compatible with conventional CMOS fabrication. The CNT Schottky diode THz detectors in this research are fabricated on PET substrate, by depositing and aligning semiconducting CNTs connecting with asymmetric metals, they can be low cost, large area imaging with high sensitivity, and operate at room temperature.

2. Fabrication Process

The fabrication process for the CNT Schottky diode detector can be divided into three separate sub processes: antenna fabrication (lift off process), CNT alignment and contact metal deposition. Each of these sub processes carried out one by one has its own specific role of fabricating the devices. Although these processes have been applied widely in fabrication realm, they need to be adjusted in order to compatible with each other for a certain device. CNT alignment method, for example, has many parameters such as frequency and solution concentration need to be adjusted and due to different geometry of different types of CNTs, those parameters from other research cannot be simply applied to our fabrication. Furthermore, one of the goals needs to be achieved is to make a low cost detector with high sensitivity, and PET substrate helps us to realize the first step. However, because of the small feature size of CNTs as well as the gaps between asymmetric contact metals, e-beam lithography seems to be the only possible method to reach nanoscale feature. It is not a low cost process comparing with lift off or etching and is not large area compatible. In order to overcome this challenge, a novel fabrication process which avoids high cost e-beam lithography is presented. It is based on self-alignment lift-off process. Each of the process steps are discussed in detail in the following sections.

2.1 Antenna Design and Fabrication

2.1.1 Antenna Design

As discussed earlier, wide band antenna with high impedance is desirable. One candidate is the log periodic microstrip antenna, which has also been used in another research for detecting THz based upon CNT bolometer detection approach [74]. Note that our devices are designed to work at THz range, it seems that high frequency antenna are more desirable, such as spiral antenna, however, one need to notice that such antenna are only workable at THz, which in another word limiting the operating frequency range, also, such antenna are always tiny so that the arms between two spirals are too close, and the CNT suspension droplet for aligning CNTs are too big comparing to the antenna. This will result in some CNTs and contaminations such as amorphous carbon aligned between arms and influence the performance of the devices.

The designation of our log periodic micro strip is based on Ref [75], which is the first publication for designing microstrip log periodic antenna. Figure 3.1 shows the geometry of one pair microstrip log-periodic antenna [75]. The ratio between R_{n+1} and R_n here generally influence the performance of E-field of the EM wave and the smaller the value is, the higher power the M-field will be provided. Here we simply let R_{n+1} /R_n=0.5, which makes the layout designation more easily but not harm the performance of the antenna.

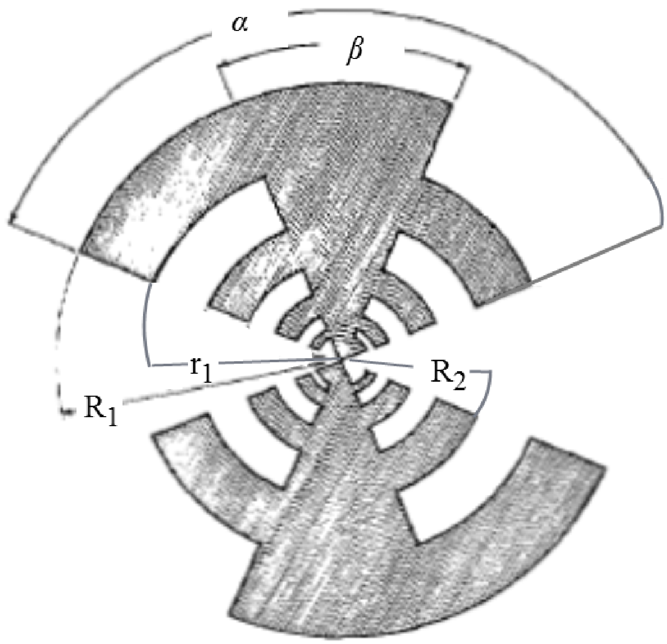

$$\gamma = \frac{R_{N+1}}{R_N} \qquad \sigma = \frac{r_N}{R_N}$$

$$\alpha = 135° \qquad \beta = 135°$$

Figure 3.1 Geometry of one pair of log periodic antenna

2.1.2 Antenna fabrication

The fabrication process for all of the antenna designs is the same. Here we just show the general lift off process for fabricating BOW-TIE antenna as an example. The size of the BOW-TIE antenna depends on the minimum and maximum frequency that it is required for detection. For the detector here, the minimum frequency is 0.1 GHz, which can be used to determine the maximum size (length) of the BOW-TIE antenna as well as the distance between the neighbor antennas. The maximum frequency is up to THz and it depends on the distance between two tips. It is usually several micrometers which are adequate for frequency up to a THz. Figure 3.2 shows the structure of 2 pairs of BOW-TIE antennas.

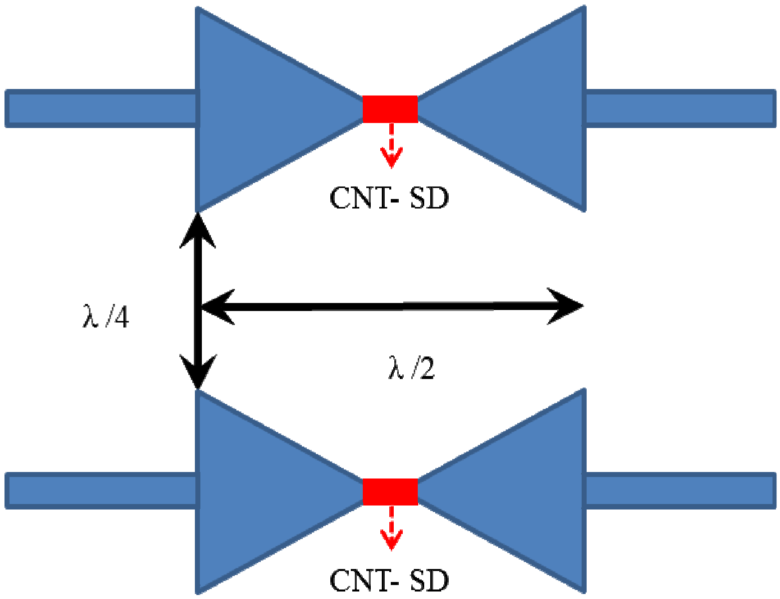

Figure 3.2 Structure of 2 pairs of BOW-TIE antennas

The length of the antenna and the minimum distance between two antennas is λ/2 and λ/4, respectively. The wavelength λ for the wave propagates in the antenna can be calculated by applying Equation (3.1)

$$\lambda = \sqrt{\frac{c_0^{\,2}}{\varepsilon_{eff}\, f^{\,2}}} \qquad 3.1$$

Where c_0 is the velocity of electromagnetic wave in free space, f is the detector's minimum detectable frequency; ε_{eff} is the effective dielectric constant of the antenna, which can approximately calculated by Equation (3.2)

$$\varepsilon_{eff} = \frac{\varepsilon_r + 1}{2} \qquad 3.2$$

Where ε_r=2.4 is the dielectric constant of PET substrate and for air it is 1. Note that the total length of the antenna includes the distance of the gap between the tips, if this gap changes, the size of two equilateral triangles need to be adjusted to meet the requirement of the total length.

Figure 3.3 shows the schematics (cross-section view) of fabrication process flows for antenna fabrication based on the lift off process. PET film with thickness of 0.05 inch was purchased from North American Color. Inc. It was cut into the round shape with diameter of 4 inches in order to fit into the mask aligner in the cleanroom. Thinner films can also be used, however they were difficult to handle during the process. After finishing the regular cleaning process for the PET substrate, photoresist S1813 was spinn coated on PET at 4500rpm for 30 seconds. Patterns were generated by exposing the whole substrate under UV light for 1.25 minutes. 3000A thin film of titanium is deposited on top of patterned photoresist by using e-beam evaporation deposition system. Titanium has better adhesion to most of the surface including PET and no additional adhesion layer is needed. For using other metals such as aluminum, silver or copper as the antenna, titanium is used as the adhesion layer. Lift-off was carried out by immersing the substrate in acetone that dissolves the photoresist. Figure 3.4 shows the antenna structure after the lift off process. The dark area is Ti and the other side is gold.

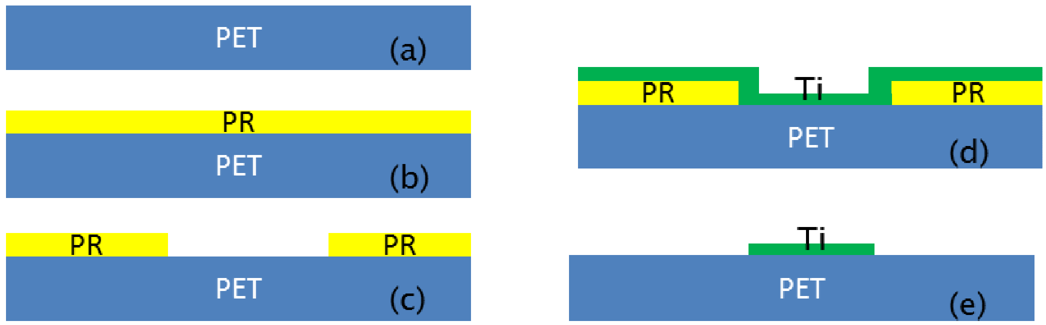

Figure 3.3 Process flow of fabricating antenna structure

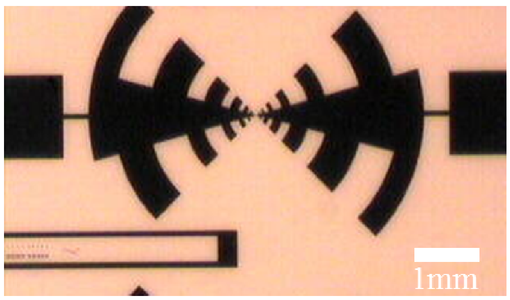

Figure 3.4 Fabricated LPA structure, with Ti as the metal layer

2.2 Alignment of Semiconducting Carbon Nanotubes

2.2.1 Methods of Alignment

Several Methods of aligning CNTs have already been developed during the past few years [63]. These methods can be generally divided into two major techniques, growth of aligned CNTs and post-growth of alignment CNTs. The former technique requires high density catalyst particles for CNTs depositing on the substrate and applying Chemical Vapor Deposition (CVD) or Thermal Deposition to grow CNTs with the assist of the catalysts. The growth direction of the CNTs can be controlled to be either vertical or horizon, depending on the recipes of the precursor gas and the configuration of the CVD system. One advantage of this method is the density of grown CNTs could be extremely high and the length of them can be modified by controlling the growth time, maximum length can reach several millimeters. By applying this method, some devices such as CNT capacitors can be fabricated. Also, if those CNTs are controlled to grow horizontally with high density, large area with low cost CNTFET array can be created. This method has also been applied for fabricating THZ detectors in [66], which also provides a better contact between CNTs and metal electrodes. However, although growing CNTs before other processes could provide a time saving method for fabrication, the quality and the properties of grown CNTs are hard to control. One knows that for one batch of CNT product, 1/3 among which is metallic CNTs, those rests are semiconducting CNTs, although specific catalyst such as CoMoCAT can provide more semiconducting CNTs[64], it still cannot avoid metallic ones, which are not suitable for CNT based microwave or high frequency EM wave detectors. On the other hand, CNT which applied as interconnects should have the metallic property, thus semiconducting CNTs are not preferred, since they will decrease the conductivity of CNT interconnection. Another problem should be addressed is that catalysts and other contaminating residues are not easy to remove without keeping CNTs untouched, these contaminates will more or less influence the quality of the devices. Post-growth of alignment CNT method are using grown CNTs and isolating them from the substrates, then disperses them in certain solutions, and applied the CNTs suspension to the proposed positions for alignment with external forces. Such external forces could be electric force (DEP) [65], magnetic force [66], capillary force [67] and force generated by surface tension [68]. In this research project, CNTs are aligned by dielectrophoresis (DEP), not only because the setup of the system is simpler comparing to others, but also this theory has been widely studied and applied due to relatively better aligning results.

2.2.2 Dielectrophoresis (DEP)

Dielectrophoresis is a phenomenon which a force is exerted on a dielectric particle when it is subjected to a non-uniform electric field. Comparing to the electrophoresis force, which is generated by a DC electric field, the pre-requisite is that the field should be non-uniform. The motion of the particles in electrophoresis phenomenon is depending to the sign of the field; however, the motion of a particle in a non-uniform, for example, AC electric field, is independent to the sign of the field, and determined by the difference of the dielectric constants between the particle and the media. Figure 3.5 and 3.6 [69] show the force exerted on a sphere particle in a uniform electric field (electrophoresis) and non-uniform electric field (dielectrophoresis).

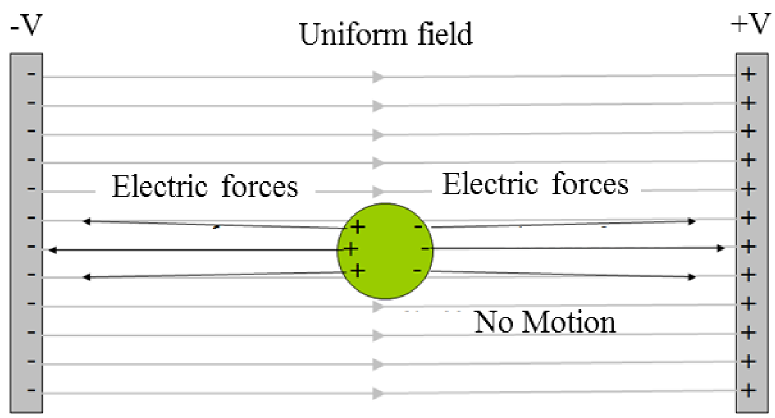

Figure 3.5 One sphere particle is subjected to electrophoresis force in a uniform electric field

Sphere particles or homogeneous objects are usually considered as the targets in certain researches where dielectrophoresis force is applied. Some researches applied this for trapping human blood cells onto the electrodes [70]; even smaller molecules such as bacteria could be manipulated and trapped to the desiring places [71]. People are also using dielectrophoresis to realize separation of molecules with different dielectric constants. Quantitative analysis has been studied by Pohl [72], and the equation 3.3 shows the relationship of dielectrophoresis force with other parameters in this phenomenon, note that this equation only applied for homogeneous sphere particles and for other shape objects, more equations and calculations are required to do the analysis.

$$F_{DEP} = 2\pi\varepsilon_0 r^3 [\, f_{CM} \,] \nabla |E|^2 \qquad 3.3$$

Where ε_0 is the dielectric constant in free space, r is the particles radius, E is the root mean square value of the electric field, f_{CM} here is called the Clausius Mossotti factor which can be calculated by equation 3.4 below:

$$f_{CM} = \frac{\varepsilon^*{}_p - \varepsilon^*{}_m}{\varepsilon^*{}_p + 2\varepsilon^*{}_m} \qquad 3.4$$

Where $\varepsilon^*{}_p$ and $\varepsilon^*{}_m$ are the dielectric constants of the particle and the media. According to this

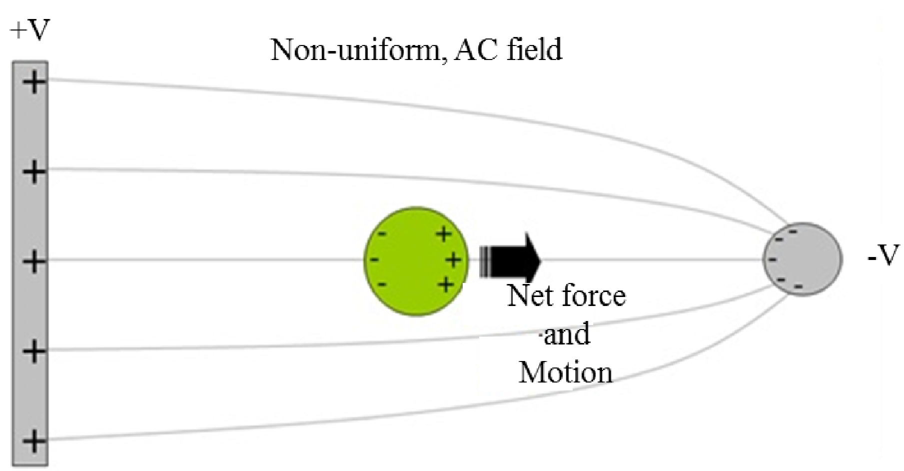

Figure 3.6 Motion of one particle in a non-uniform AC electric field with different directions

Figure 3.6 (cont'd)

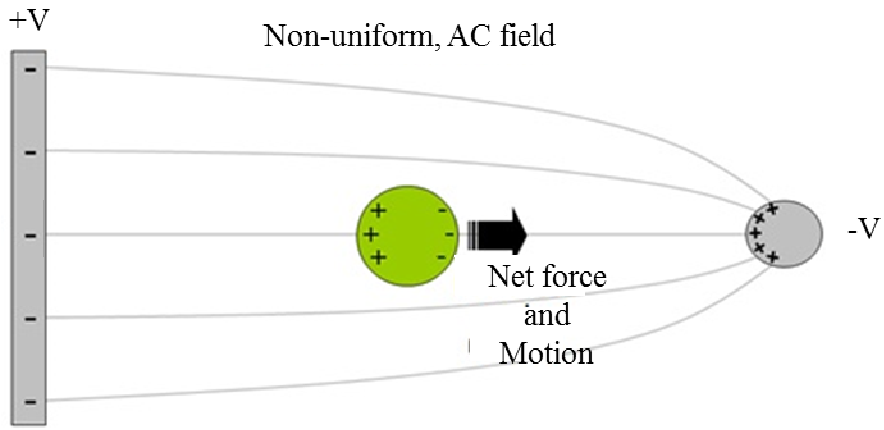

Clausius Mossotti factor, one can clearly tell that the motion of a sphere particle will be along with the direction of transition electric field if the permittivity of particle is larger than that of the media, or against that of the transition electric field. From this point of view, particles with large dielectric constant will have smaller DEP force and perform suspending in the solution; those particles with lower dielectric constant will move to certain direction in the media.

CNTs are long tubes which can be considered as prolate (ciga-shape) particles. The calculation of DEP force subjecting on those tubes are slightly different from that of sphere objects. A simplified CNT model in media has been set up and basing on certain calculation, equations are carried out and given in [73]. Moreover, since CNTs are not spherical particles that have homogeneous shape, another force which is called dielectrophoresis torque is also influencing the movement of CNTs, and calculations for this is based on the model shown in figure 3.7 and 3.8. The DEP force subjects on CNT can be calculated by equation 3.5. In Figure 3.8, CNT is modeled as a prolate ellipsoid with homogeneous dielectric properties. Those x,y,z directions represent the coordinate of the dielelctrophoresis system, 1,2 and 3 represents the axis of the ellipsoid, and angle between the electric field and the longest axis 1 is θ. In this model, CNT only has an angle with E in the x,y plane, so the direction of the torque is along the z direction and pointing out the paper.

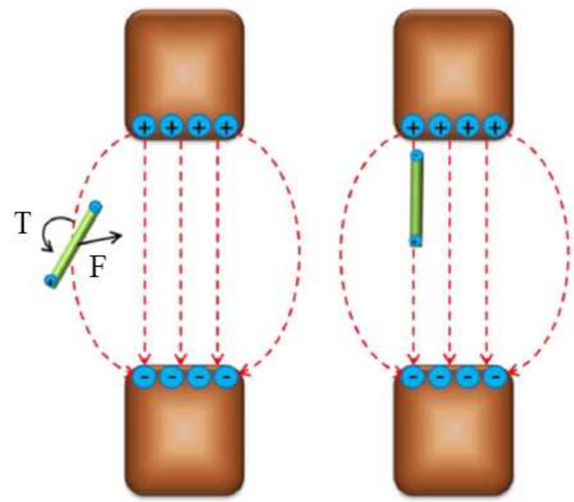

Figure 3.7 DEP force and DEP torque subject on the tube shape CNT in the media

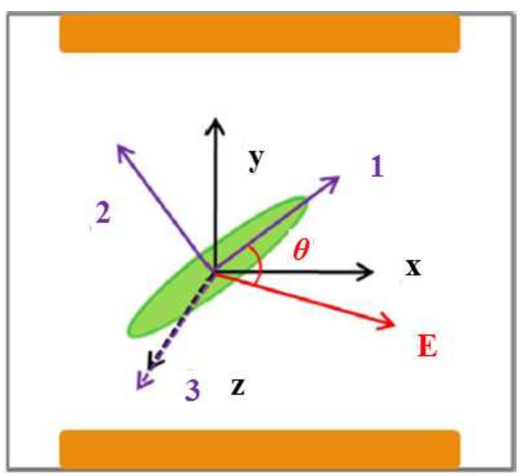

Figure 3.8 An elliptical model for calculating DEP torque on one CNT

$$F_{DEP} = \frac{3}{2}\pi r^2 l \varepsilon_m \operatorname{Re}\left[\tilde{K}_1\right]\nabla|E|^2 \quad 3.5$$

where r and l are the radius and length of the CNT, ε_m is the permittivity of the media, E is the root mean square of the electric field, $\tilde{K}_1$ represents the complex frequency dependent factor similar to the Clausius–Mossotti factor along the "1" direction in figure 3.7, and can be calculated by equation 3.6 for the nth direction:

$$\tilde{K}_n = \frac{\tilde{\varepsilon}_p - \tilde{\varepsilon}_m}{3\left(L_n\left(\tilde{\varepsilon}_p - \tilde{\varepsilon}_m\right) + \tilde{\varepsilon}_m\right)} \quad 3.6$$

In which $\tilde{\varepsilon}_m$ and $\tilde{\varepsilon}_p$ are the complex permittivity of the media and CNT, respectively. L_n here is the depolarization factor which can be calculated by elliptical factor. The torque that subjecting on CNT can be calculated by equation 3.7, since θ is only in x,y plane, only direction "3" has the torque value.

$$\left\langle \overrightarrow{T_3} \right\rangle = \frac{9}{2}\pi r^2 l \varepsilon_m \left(L_2 - L_1\right)\overrightarrow{E_1}\overrightarrow{E_2}\,\mathrm{Re}\left(\tilde{K}_1 \cdot \tilde{K}_2\right) \quad 3.7$$

After putting $\tilde{K}_1$ and $\tilde{K}_2$ and other parameters inside, the torque along the "3" direction can be derived from equation 3.8

$$\left\langle \overrightarrow{T_3} \right\rangle = \frac{1}{2}\pi r^2 l \varepsilon_m \sin\theta\,\mathrm{Re}\left(\frac{\left(\tilde{\varepsilon}_p - \tilde{\varepsilon}_m\right)^2}{\tilde{\varepsilon}_m\left(\tilde{\varepsilon}_p + \tilde{\varepsilon}_m\right)}\right) \quad 3.8$$

One also need to notice that besides the DEP force and DEP torque, CNTs also have the drag force subjected on generated by the motion against the media, which is related to the viscosity of the media μ , size of the particles r and the velocity that the particles are travelling v_{DEP}, shown in equation 3.9

$$F_{drag} = r\mu v_{DEP} \quad 3.9$$

Although those calculations are simplified and some of other parameters such as the defects on the CNTs, interaction between two particles and external force disturbing are not taken in to consideration, both simulations and practical experiments have been carried out and showed that most CNTs more or less followed the roles calculated above. However, other parameters are still very critical for CNT alignment. It is shown in Ref [65] that the concentration of CNT suspension, AC frequency and amplitude, gap size between electrodes, and the CNT types also influences the alignment results. It is a common sense that the higher the concentration the CNT suspension, the large number CNTs will stay in between the gap. Moreover, higher frequency operations are more likely push CNTs away from the electrodes and leaving less in between. Applying DC offset will results CNT bundles separation and “sucking” CNTs toward one electrode.

However, one cannot simply apply those results from experiments carried out by other researchers, there are many uncontrollable varieties and the experimental set up as well as the electrode shapes is totally different. The applied AC voltage should be controlled in a certain range above a certain value to generate enough electric field for alignment but lower than a level in order to avoid creating strong electric field which could burn down CNTs. This is quite critical since CNTs are long tube over 2μm, smaller bias will not be able to move them efficiently. The CNT suspension are required ultrasonicate so that CNTs bundles are open and the whole suspension is uniform. However, the time for untrasonicating also varies due to different types of CNTs. Those CNTs with surfactant are more easily to separate but it will influence the conductivity for the further measurements. For our research, we carried out our own parameters and results for doing a better alignment for our devices.

2.2.3 CNTs alignment for Schottky diode THz detector.

The theoretical analysis above provides the basic concepts and calculating methods for the DEP force subjecting on CNTs, it just shows the general information how DEP works for CNT alignment. In any particular sets of CNT aligning experiments, the parameters such as frequencies, p-p AC voltages, and CNT concentrations should be adjusted in order to satisfy the length and diameter of CNTs, the length of the gaps as well as the alignment criteria, which depends on the requirement of the devices.

In some of the CNT researches such as building CNT-FET and CNT-based mechanical structures, only one semiconducting SWNT or metallic CNT is required to be aligned in between the electrodes[76][77]. However, one of goal of this research, which has been also proved by simulation, is to increase the sensitivity of the CNT based THz detector by increasing the current go through the devices and multiple numbers of CNTs should be connected between the electrodes. To this point, aligning one CNT is not necessary, and larger CNT suspension droplet can be applied to the desired area in order to dense the number of CNTs. The AC voltage applied in each experiment is different due to the gap length. In [76], the V_{p-p} is 4V for a 300nm gap with frequency about 12MHz; in [78], V_{p-p} is 1.5V for 1 to 3μm gap with frequency about 1kHz. Since high voltage will burn down the CNT and destroy the devices, the density of electric field in [78] is set to be the reference and the AC voltage is determined by the ratio of the length of gaps: take 1μm gap from [78] and maximum density of electric field is 0.75V/μm, in this research, the gap is around 6μm so the maximum voltage is 4.5V and the V_{p-p} is determined as 9V. The frequency also ranges from several KHz to tens of MHz in different research papers [76] [78] [79]. Note that in [78], it is said that frequency higher than 1MHz will create a negative DEP force which can push semiconducting SWNT away from the electrodes, but attract metallic ones. But this phenomenon was not obvious for the CNT alignment in this research, even decrease the current when lowering the frequency to several KHz. Thus we follow [79], which also aligned semiconducting SWNT successfully at the frequency around 10MHz.

As most of the DEP process for aligning CNTs, semiconducting SWNT suspension is prepared by mixing CNT powder and IPA (2-propanol) solvent and ultra-sonication is also applied to the suspension for 30mins. A micro syringe is used to deposit CNT suspension droplet on the gap of the device, which is sitting on the plate of the probe station. Again, since high density CNTs are required, larger droplet through wide syringe tip around 1μL can be placed. But this requires high purity of semiconducting SWNT powder, otherwise because of the existence of large amount of metallic CNTs, the semiconducting properties will be compromised and Schottky contact will be difficult to form. For this reason, the CNTs used in this research have 95% of semiconducting SWNT in the powder. At the same time, AC voltage of $V_{p\text{-}p}$=9V is applied through the probes contacting with the electrode pads on each side. During the evaporation of IPA in about 1 min, CNTs are aligned between the electrodes. The setup of the DEP system is built upon the probe station as shown in Figure 3.9. The AC power is wired to the probes which contact the electrodes. In order to observe the influence of the concentration of CNT suspension, three different concentrations of 2.5μg/ml, 5μg/ml and 10μg/ml suspensions, as shown in Figure 3.10, were applied to the samples, and Figure 3.11 shows the alignment results basing on those concentrations with parameters of $V_{p\text{-}p}$=9V, f=10MHz. It is shown that 10μg/ml has the best alignment result among the three, most of the CNTs tend to align along the electric field lines in the gap. Alignment can also be measured by simply measuring I-V characteristics between the pads. Details of this will be discussed in Chapter 4.

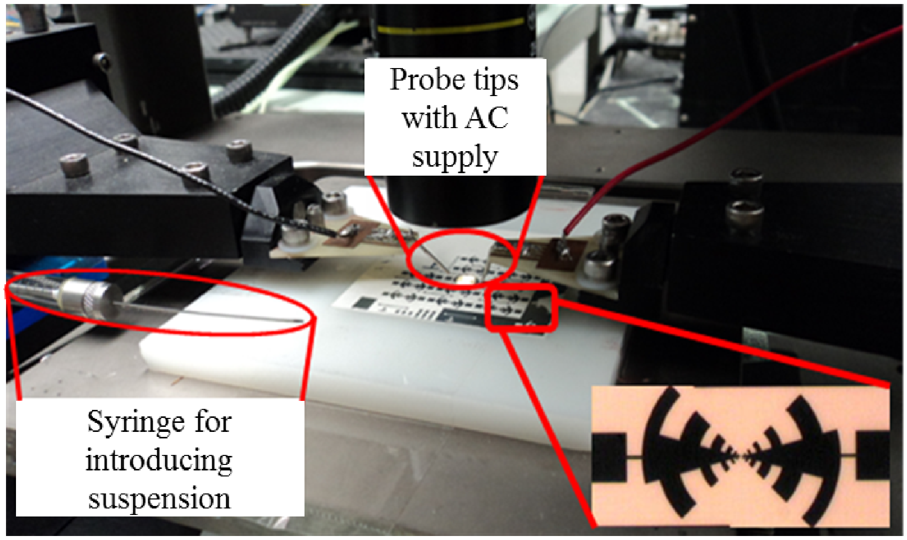

Figure 3.9 DEP system setup basing on the probe station

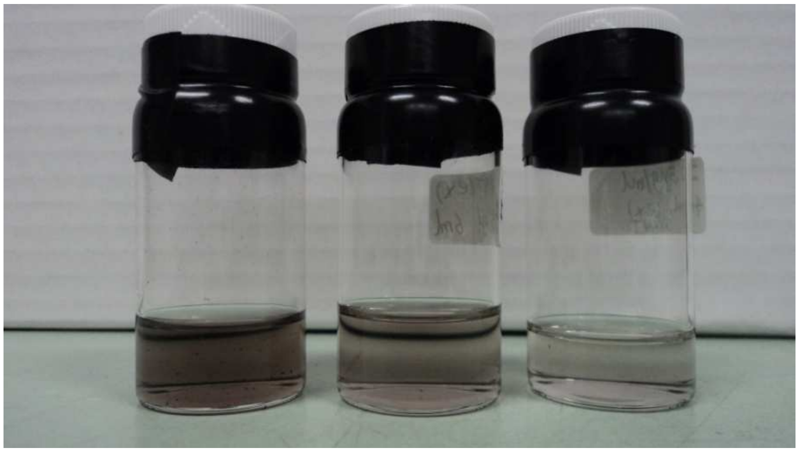

Figure 3.10 Semiconducting SWNT suspensions with concentration of 10μg/ml, 5μg/ml and 2.5μg/ml, from left to right

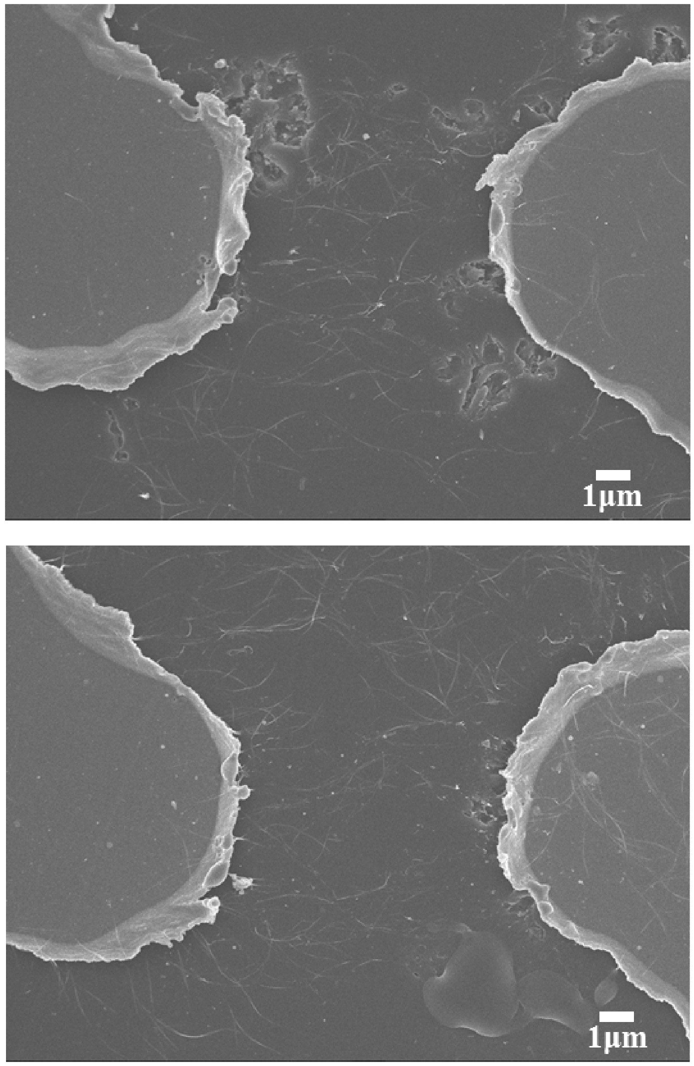

Figure 3.11 Multi-CNT alignment results for 2.5μg/ml, 5μg/ml and 10μg/ml, from top to bottom

(V_{p-p}=9V, *f*=10MHz)

Figure 3.11 (cont'd)

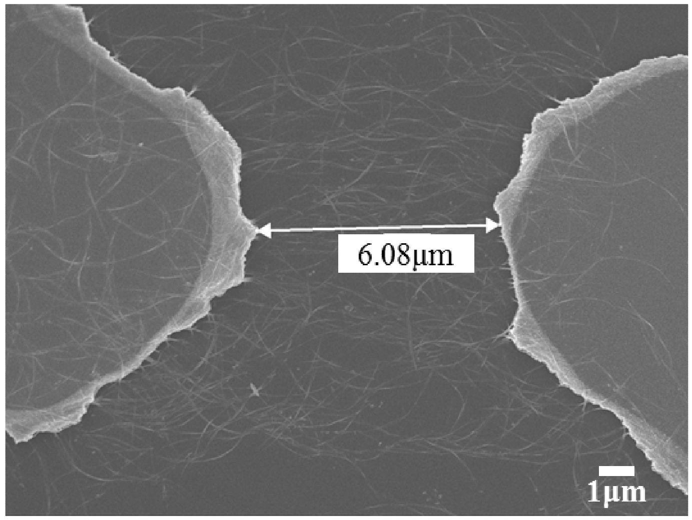

2.3 Fabrication of Schottky and Ohmic Contacts

As mentioned at the beginning of this chapter, large-area, and low cost features are desired for realizing high resolution and sensitivity THz sensors. Since CNT based THz detectors usually have small features around 1~2μm or even downsizing to hundreds of nm, high resolution photolithography, e-beam lithography, is inevitable. However, although this method could successfully create nano level structures, the cost for fabricating single device is high and time consuming, let alone large area detector array, which always have hundreds of devices. The advanced UV photolithography machines claim that 2μm feature can be created, but not all fabrication labs in universities and research institutes have such expensive equipment, and one will come back to e-beam for features smaller than 1μm. In order to achieve goals of large-area and low cost, batch fabrication should also be utilized, meanwhile keeping the process reproducible. A novel fabrication process has been developed for the THz detector in this research. Patterns with 1μm or smaller gaps can easily be fabricated using this approach. This process is based on the principle of isotropic metal wet etching which can create the undercut under the photoresist masking layer. The undercut size is basically determined by the thickness of the metal layer underneath. Details of this are discussed below.

Etching process in micro fabrication is used to remove certain part of the layer and create the pattern on the wafer. Both wet and dry etching methods could be used according to the requirement of the structure. Dry etching such as RIE and DRIE, usually performs selectively anisotropic etching and can create vertical side wall underneath the mask layer. This method is frequency used since the structures after etching have almost the same sizes as designed, showing in Figure 3.12 (a). On the other hand, wet etching is seldom used since it etches at same velocity in all directions, which is also called isotropic etching, and large bias can be created when etching thick film away, also showing in Figure 3.12 (b). The bias length is almost equal to the thickness of the film. If the film is thin and undercut is not a critical problem for the devices, both dry and wet etching methods are suitable, however, once the undercut becomes influencing the devices performance, only dry etching is desired. Since the length of the undercut is determined by the thickness of the film, nano level undercut is able to form if the film thickness is in nano range. What's more, wet etching can be done by immersing the whole wafer in a bath of the etchant, which allows realizing the goal of batch fabrication. The idea of the novel fabrication process originated from the information above.

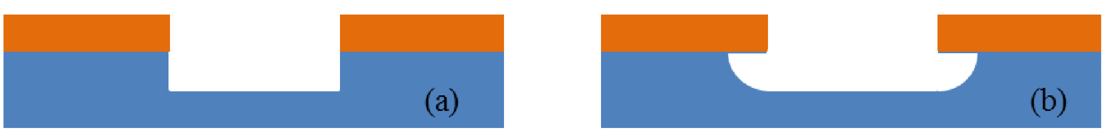

Figure 3.12 (a) Anisotropic Etching (most dry etching); (b) Isotropic etching (wet etching)

The fabrication process flow diagram is illustrated in Figure 3.13, which provides a cross-section view of the device of creating the undercut and realize self-alignment in the range of nanometers, through (a) to (h)

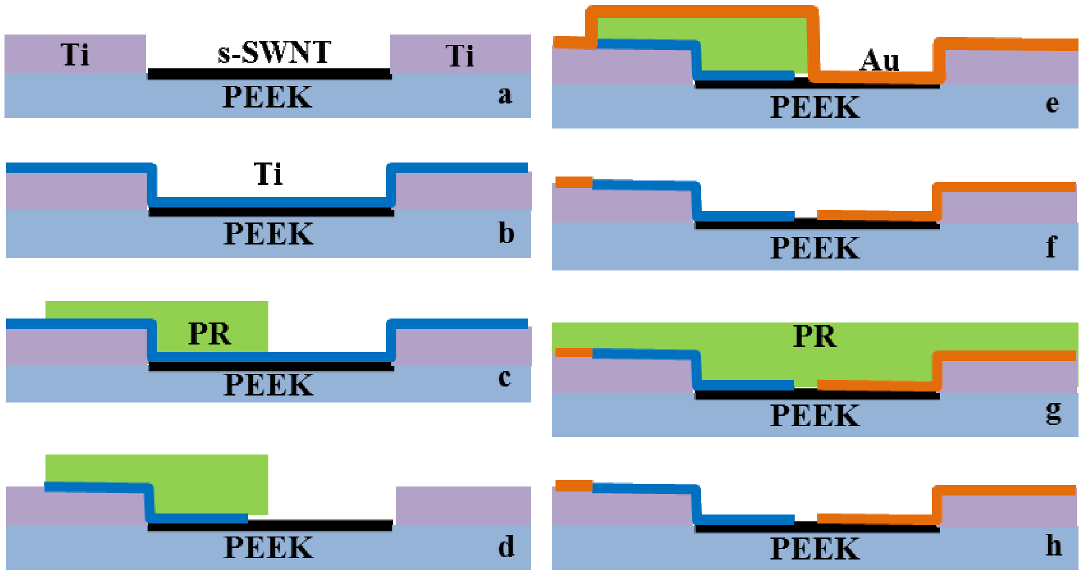

Figure 3.13 Fabrication process flow diagram of creating undercut structure and self-aligning approach

Semiconducting SWNTs are aligned between Ti antenna tips, which are created by lift off process, showing in (a), note that CNTs which lie in the middle of the gap also overlap on each other, since they are relatively small comparing to the electrodes, the overlap height can be omitted, but in order to show the aligned CNTs, they are not drew in scale. Then a 150nm of another Ti layer is deposited by e-beam evaporation to create the Schottky contact between CNTs and Ti, which corresponded to step b. As explained in Chapter 1, metals such as Ti (4.3eV), Al (4.06-4.26eV) and Ag (4.5eV), whose work function is smaller than that of semiconducting CNTs (4.8-4.9eV), can be used for Schottky contact. Following spin coating and patterning of positive resist (step-c), Ti is selectively etched, and the only remaining area of this Ti layer is that on one side of the previous antenna pad. During this step, the undercut is controlled by the type of etchant use and by the thickness of the Ti layer. The depth of undercut determines the length of the CNTs which will be exposed of the finished Schottky diode THz detector and the parameters (intrinsic resistance) of the small-signal model. Undercut of step-d was carried out using HF: H_2O_2:H_2O=1:1:200 etchant. Intermediate measurements of I-V characteristics show that CNTs were found to be inert to this etchant and remain semiconducting. Due the fragile free standing photoresist above the undercut region, the sample was washed and blew dry very gently before continuing for further steps. After this undercut, as shown in step e, gold (Au) is blanket deposited on the wafer using e-beam evaporation again. The overhanging positive resist above the CNTs acts as a shadow mask. Again, metals such as Au (5.1-5.47eV), Pd (5.22-5.6eV) and Pt (5.12-5.93eV) whose work function is larger than that of semiconducting CNTs can be applied as Ohmic contact metals. This is followed by photoresist lift-off of Au layer. At this step, second layer of Ti on the antenna pad is exposed as well as the CNT undercut region. Although the photoresist is a protection of CNT and undercut region, it must be removed since another layer of photoresist will be spin coated and bubbles could be generated between two layers of photoresist during soft baking.

Patterning of this Au layer is carried out using another photoresist layer (step-g), by using a safer etchant than Aqua Regia, a mixture of KI, I_2 and H_2O. The antenna structures, coplanar structures, and probe-pads are formed during this step. Figure 3.14 (a) shows an example of fabricated Schottky diode THz detector, which has Au and Ti on different sides. Figure 3.14 (b and c) also shows the Atomic Force Microscopy (AFM) pictures of the small gap formed using undercut/self-alignment process, which has metal thickness (Ti or Au) of 500nm. This gap defines the effective length of the Schottky diodes. It is shown in the figure that the gap is around 1μm, but this value doesn't in consist with the 500nm metal thickness, this is because over etching was happened during wet etching. However, over etching sometimes is useful, which could prevent two antenna pad contacting each other due to the thin residue layer remained at the bottom of the undercut region. This length can be reduced through precise control of etching rate through well controlled concentration, temperature, resist bake conditions, and uniformity of the metallization layer. AFM pictures also show there are approximately 20 CNTs aligned between the Au- and Ti-pads, this number of CNTs satisfies the simulation results carried out in the second chapter.

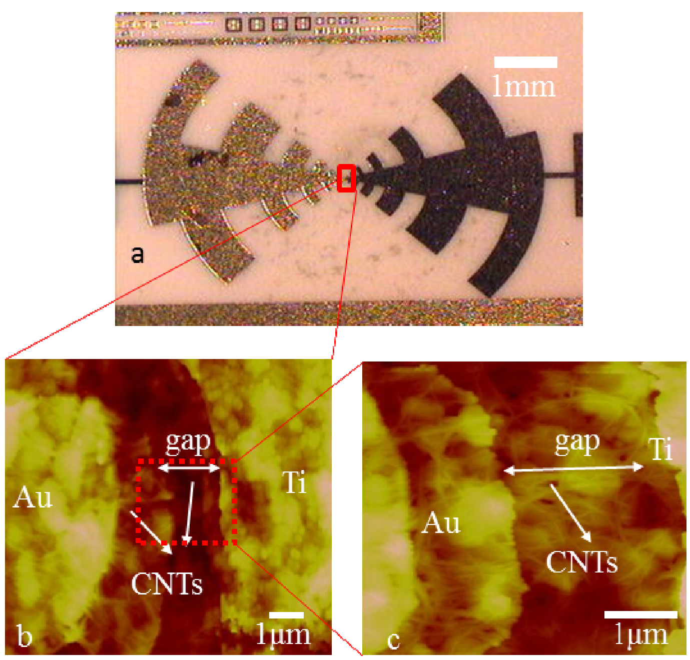

Figure 3.14 (a) fabricated CNT Schottky diode THz detector, (b) AFM picture of the gap area, (c) closer look at the gap by AFM

Above all, each of the fabrication process is discussed in details, which provide a clear view of how the device is created. Note that those procedures are not completely well defined, modifications are always carried out in order to improve the results measured in chapter 4, for example, the metal used for originally designed antenna pads are Ti, which could reduce the conductivity due to the oxidation in the air, so an intermediate layer of copper is deposited between two Ti layer to increase the conductivity and absorb more RF power from the horn antenna. Another unexpected issue occurred during the etching of Ti to create the undercut. Since the deposition layer is not uniform, etchant etched away thinner area first and started to attack the antenna pad layer and even etch this layer away. For solving this problem, Chromium (Cr) is deposit as the top of the antenna layer, and Ti etchant does not attack Cr. Cr is a protection layer for antenna. The measurement results will be discussed in the following chapter.

Chapter 4 Measurements and Results of CNTs Schottky Diode THz Detector

Several characteristics of the device were measured, including DC and RF at room temperature. Measured rectified signals (current and voltage) were in the nano-scale range. For this reason, the setup was optimized to reduce ambient noise from the environment by shielding and through the use of low-loss coax cables. The device itself also has inherent noise. Apart from the thermal and the flicker noise, noise originates from CNT-CNT contact and from the metal-CNT contacts. CNT-CNT contact is a weak joint and not stable. This leads to changes in current characteristics due to thermal variations and mechanical vibrations. For the measurements, device having low noise and desired I-V characteristics were chosen. This chapter first discusses the I-V characteristic of the device, and then presents the detectors sensitivity measurements.

1. I-V characteristics of CNT Schottky diode THz detector

1.1 I-V Characteristics

Current-Voltage characteristics of the devices were measured using a Semiconductor Parameter Analyzer (SPA) over a voltage range of -1 to 1V. Higher voltages would burn the CNTs and also results in breakdown of the devices, and thus not measured. The devices were probed using a wafer probe station and DC probes coupled with the SPA. The probe station is placed inside a Faraday cage to filter out the ambient noise. The SPA is controlled by a LabView program and the I-V data is then transferred to MATLAB for further analysis.

Figure 4.1 shows the I-V characteristics of several samples made from different CNT suspension concentrations. It clearly shows that most of the samples (Sample 1 to 5) provide a strong non-linear behavior, which indicates the novel fabrication for CNT Schottky diode is promising and repeatable. The devices with higher CNT concentrations (multiple CNTs in parallel) allow flow of higher current for the applied bias. As discussed in chapter 2, tunneling current can be ignored at low bias voltages where the thermionic current dominates. However, at higher bias voltages (> 0.3V), tunneling current is also involved in the contribution to the total current. This value is smaller than 0.5V predicted in Figure 2.10. This may be due to a composite effect of multiple CNT devices placed in parallel with each other. There are no two identical CNTs (and associated devices), each of them have their own properties due to defects and geometries which may be contributing to this effect.

Here the reverse current has similar shape as the forward current, but slightly lower current flow. This indicates that the diode is operating as a back-to-back Schottky diode. Schottky effect can only be attributed to CNT making contact to the Ti metal in the fabrication process of this research. The Ohmic contact region may be touching the first Ti-layer. The first Ti layer was used for the alignment of CNTs using electrophoresis. In the follow on devices, during fabrication it was ensured that the Schottky contact alignment was moved further away from the Ti-layer. Also, thicker gold contact was implemented. The measured I–V curve indicates non-linear behavior as required for RF detection. Furthermore, it shows that different concentrations of CNTs can be used in fabricating devices having different I-V characteristics. In other words, devices having different impedance characteristics can be fabricated.

With further increase in concentration of CNT for device fabrication, entangling of CNT begins to occur during alignment. Sample fabricated from high concentrations shows an Ohmic or resistive behavior (sample 6). Such devices make poor THz sensors. In order to minimize this effect, the suspension was improved by the use of ultrasonication. After this step, the samples were allowed to sit for 15 minutes to allow sedimentation of heavier CNT-bundles leaving the individual CNT suspension on the top layer of the liquid. Above all, a right concentration balance has to be reached to design an optimum diode for detector applications and this process step requires further detailed study and is beyond the scope of the proposed work.

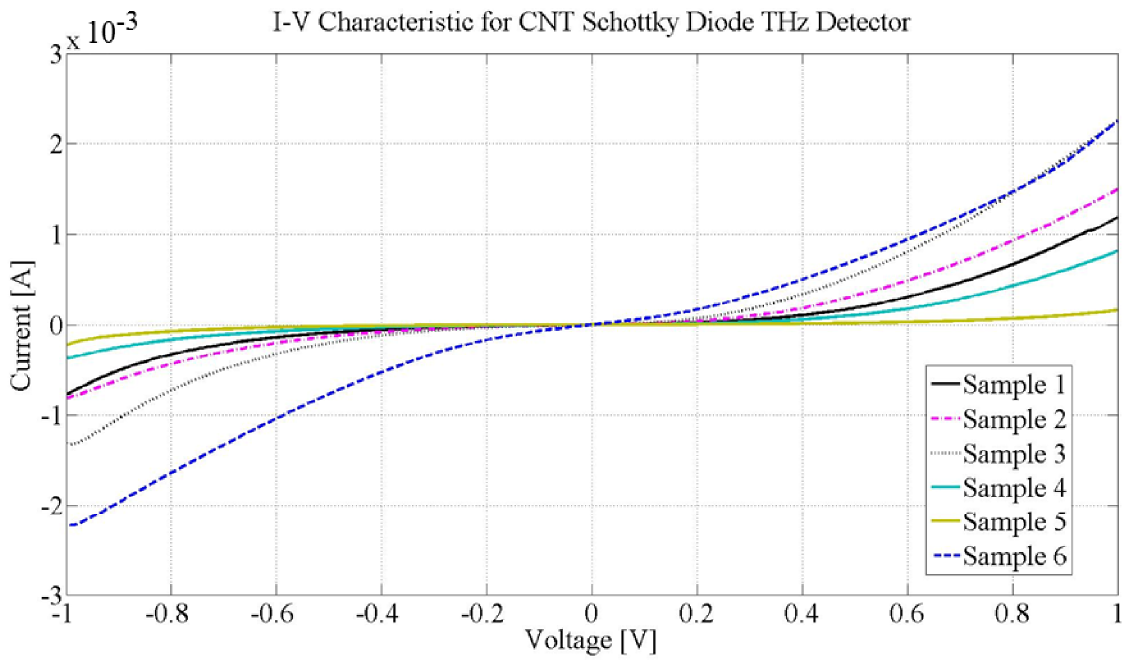

Figure 4.1 I-V characteristics of several samples with different CNT suspension concentrations

Upon optimizing the CNT concentration and metal contact alignment, samples that have typical Schottky diode characteristics with strong non-linear I-V curve were attained. An example measured I-V characteristic is shown in Figure 4.2 and 4.3 for the logarithmic absolute current value. The effective resistance (series plus junction resistance) of the device is also shown in the same figure for illustrating the variation of impedance as a function of applied bias. It is clear to see that the I-V curve has stronger non-linear behavior than those in Figure 4.1, and the reverse current is about 10 times smaller than forward current, which shows that an improved Ohmic contact is formed. The reverse breakdown of the device is near -1V. The effective resistance curve, Figure 4.2, reaches maximum value of approximately 10 MΩ at zero bias and decreases when bias increases on both the positive and the negative sides. The convexity of resistance curve around 0.3V is due to some reasons such as recombination mechanism, but the general trend of rapidly decreasing continues. As the positive bias increases, current starts to increase with strong non-linearity near 1V. In the non-linear region the diode resistance decreases. Beyond point where there is a sudden change in current probably due to the unexpected carrier recombination. As discussed in chapter 2, biasing of the diode will provide the optimum impedance matching with the antenna. According to the value in the plot, the minimum effective resistance (R_s+R_d) is equal to 12KΩ, which can be used in the equations in chapter 2 and calculate the voltage sensitivity β_V and NEP.

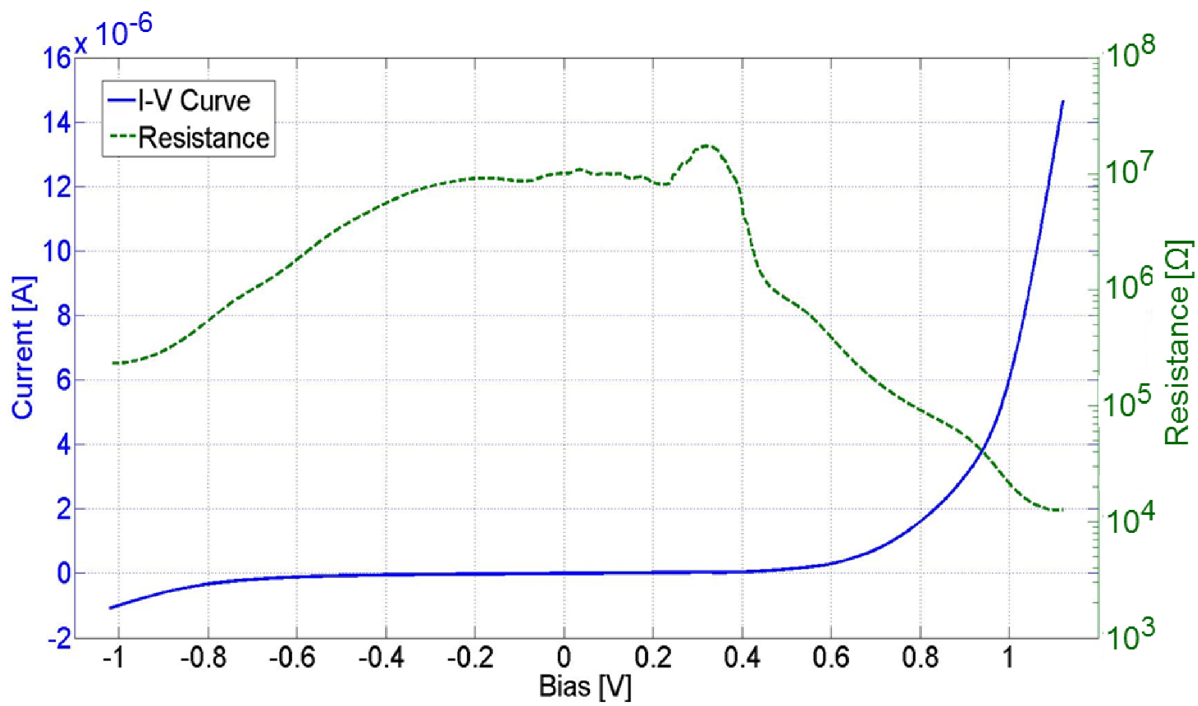

Figure 4.2 Strong non-linear I-V characteristics and total resistance of one device

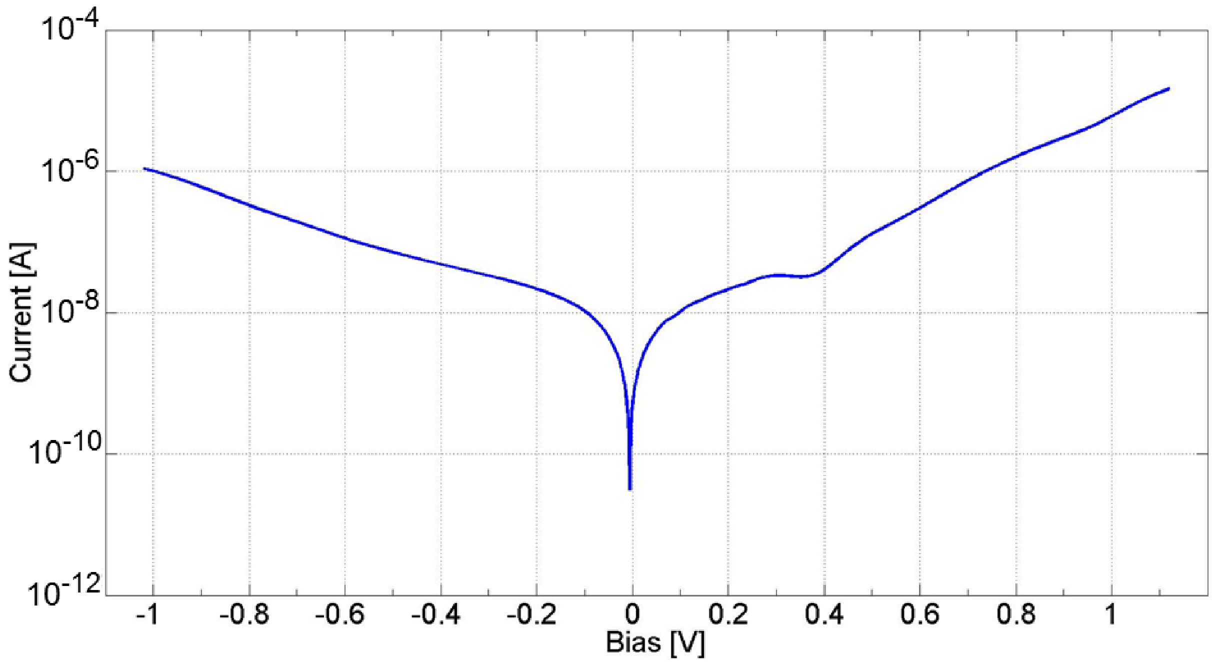

Figure 4.3 Semi-logarithmic I-V characteristics for the device in figure 4.2

In Figure 4.3, which shows the semi-log I-V characteristics of the CNT Schottky diode detector, there is a tiny current valley around 0.3~0.4V, which is in consistent with a sudden change in effective resistance. The zero bias current is approximately 5.6×10^{-10}A. Note that this value is different from each device since CNTs are not identical and the contacts between CNTs and metal are also not the same.

1.2 Ideality Factor

In chapter 2, it is concluded that thermionic emission current is the dominant part that contributes to the total current. The tunneling current only exceeds thermionic current at larger bias (>0.5V). According to the simulation results, the optimal bias for getting high sensitivity is 0.34V, which stays within the thermionic current effective region. Although from real devices, more genuine data such as I-V curve and resistance are obtained than from simulation, it is also meaningful to look in detail about which current is dominant for the total current. Chapter 2 also proves that the ideality factor lies between 1 and 2 in the thermionic current region, which is due to the recombination mechanism. Simulation results show that a typical semiconducting SWNT with carrier concentration of $N_A=10^{16}$ cm^{-3} (this equivalent value has been transformed from 1D material value) has smaller tunneling current than thermionic current. However, some researchers have concluded that it is possible to have larger tunneling current than thermionic current in nano-Schottky diodes with high carrier concentration above $10^{18}cm^{-3}$ [80] [81] [82]. Comparing the I-V curve shapes of both thermionic and tunneling currents in Figure 2.10, general diode equation also fits for tunneling current, except the differences at the constant parts. These results are similar to the ones reported in [83].

According to the literature again, the ideality factor in the equation, which includes tunneling current, is way larger than 2 and depends on the device itself. So for this device, the I-V data are then taken for curve fitted in order to find the ideality factor. Note that here the fitted curve would be the combination of thermionic and tunneling currents since they have the same equation form, the ideality factor would determine which is dominant. In the simulation chapter, the ideality factor in thermionic current equation only represents the rate of combination of carrier for thermionic current. Original data and fitted curve are shown in Figure 4.4, in which the reverse current $I_0=4.23\times10^{-9}$A, and ideality factor n=5.3, which is similar to a value shown in [84]. This ideality factor value is larger than 2, which illustrates that tunneling current is dominant through the whole bias region especially above 0.6V. The linear plot shows the curve fitted well, but in semi-log plot, at low bias from 0-0.2V, there is a divergence between measured data and fitted curve. Figure 4.5 plots the variation of ideality factor n respect to the changing of applied voltage. The calculations of n bases on a simplified equation 4.1 derived from general diode equation

$$n = \frac{q}{kT}\left(\frac{\partial \ln(I)}{\partial V}\right)^{-1} \qquad 4.1$$

Due to the noise disturbance during measurement, the n value is fluctuating through the whole bias region, and its shape is also in consisting with the concave on the I-V curve. But it is clear to see that the trend of n value increases and mostly stays between 4 and 6. At lower bias from 0 to 0.1V, n is small because equation 4.1 is not applicable since the current is so small and requires full term of the diode equation. A better fitted curve for this 0-0.2V low bias area is shown in Figure 4.6, in which I_0=1.09×10^{-8}A, and ideality factor n=5.98.

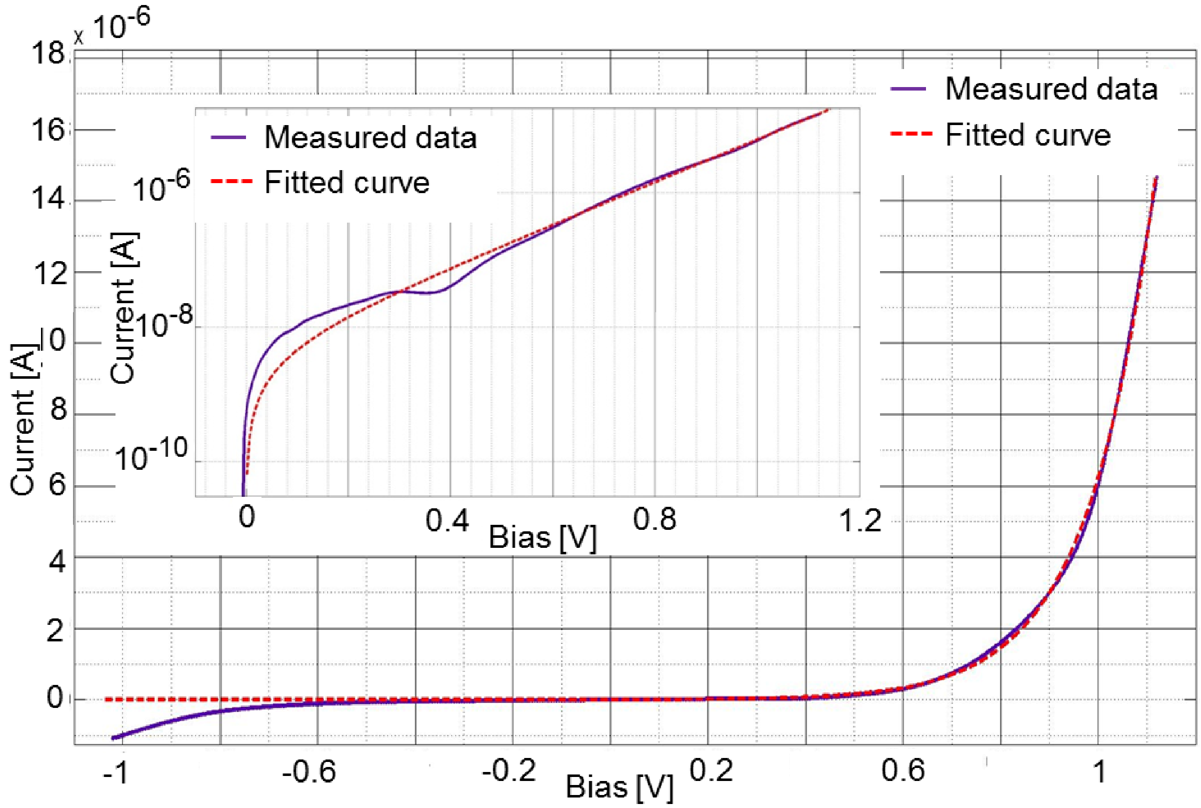

Figure 4.4 Curve fitting for CNT Schottky diode basing on general schottky diode equation, in which I0=4.23×10^{-9}A, n=5.3. Inset figure shows same data in a semi-log plot

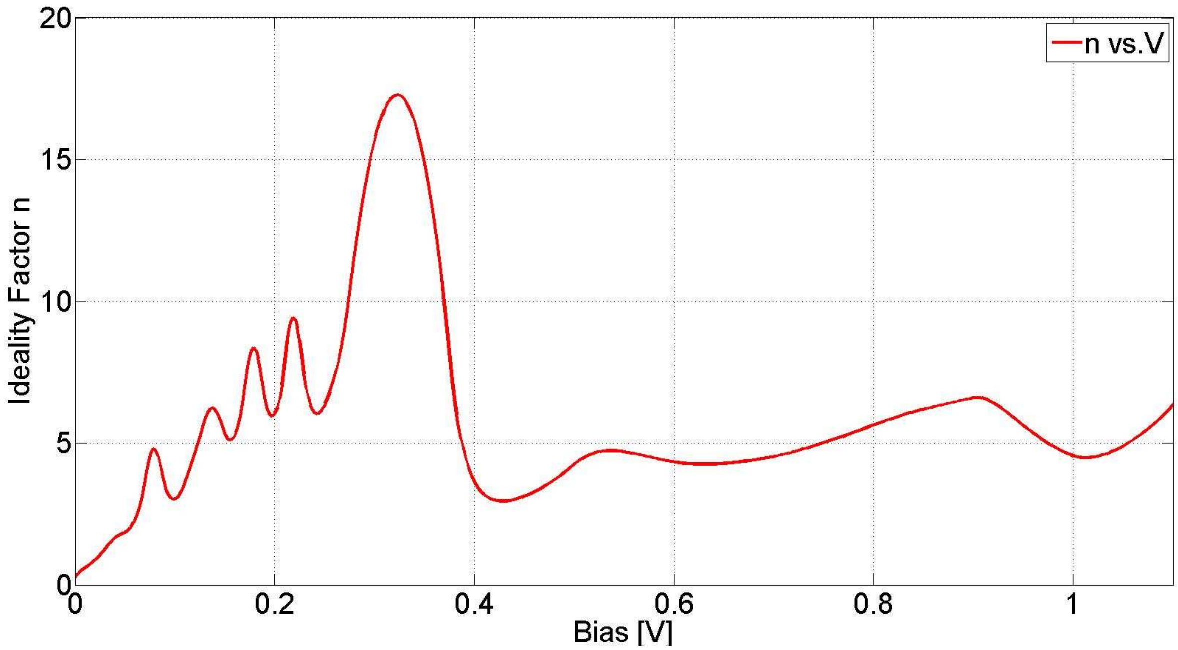

Figure 4.5 Ideality factor n vs. applied voltage

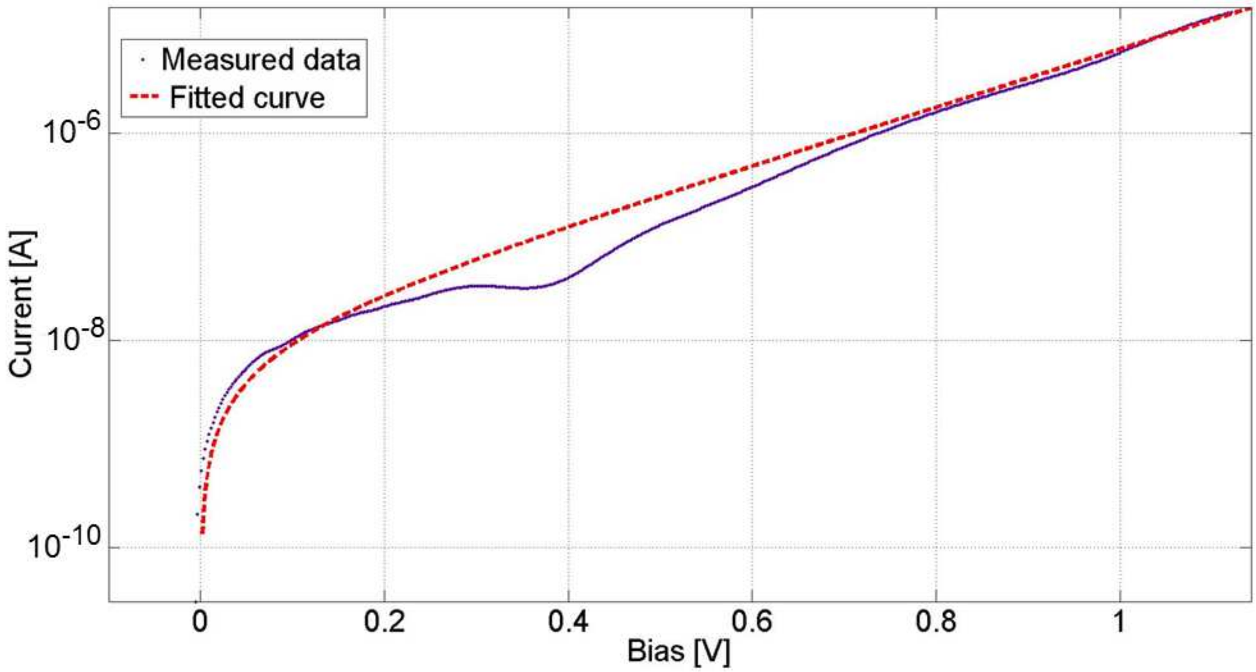

Figure 4.6 A better curve fitting for low bias 0-0.2V, in which $I_0=1.09\times10^{-8}$A, and ideality factor n=5.98

This proves that at low bias, tunneling current contributes dominantly to the total current. Note that this is different from the conclusion reached in Chapter 2. This does not in any way indicate the simulations approach is incorrect. The simulations are based on a certain set of parameters which are based one type of SNWTs with low carrier concentration (10^{16}cm^{-3}) and relatively large bandgap (0.61eV). In an actual device, those the carrier concentration and bandgap can vary over a large range (N_A and E_g could be around 10^{18}cm^{-3} and smaller than 0.61eV due to the small CNT diameter). Simulation results do however provides a starting point of the experimental results. Based upon the measured results, simulations will be improved.

2. Preliminary Microwave Measurements

After measuring the I-V characteristic, the device is then setup for microwave measurements. RF source generator provides the microwave signal and it is connected to a horn antenna which is vertically facing to the LPA of the devices. In order to get enough power coupling from the horn antenna to the on-chip antenna, the distance between the front-end of the horn antenna and the device was set to about 2-3cm. Upon RF illumination, the rectified voltage is expected across the probe pads two electrodes. In the first experiments, no signal was detected across the diodes. This was determined that the Ti metallization used for the fabrication of antenna element was thin and also got oxidized leading to a high resistance metal layer. This meant that the power could not efficiently couple to the diode element. Two possible solutions can help to overcome this problem: one is depositing a more conductive layer metal such as Cu underneath the top Ti layer, which could help improve the power transmission of the RF signal; another way is by using a coplanar probe directly contact with the antenna pads and send the RF power to the device. The second method is simpler to apply since the existing fabricated devices could be used. For the new devices, thicker metals using Cu electrodes are being implemented. Furthermore, alternate to Ti metallization is being studied.

2.1 RF detection at zero bias

The device is first measured at 18GHz under zero bias conditions. The reasons for choosing zero bias is to test whether the detector can work as a passive device with good rectification. This also avoided damaging of devices due to basing. 18GHz is first used for the preliminary tests. Figure 4.7 illustrated the detection results with respect to the incident power onto the device under such condition. These measured results show that the detector has a good sensitivity. The sensitivity is expected to be higher for higher conductive antenna metallization as the RF power drop will be less. Furthermore, the sensitivity will improve for higher concentration of semiconducting SWNTs applied in the device fabrication.

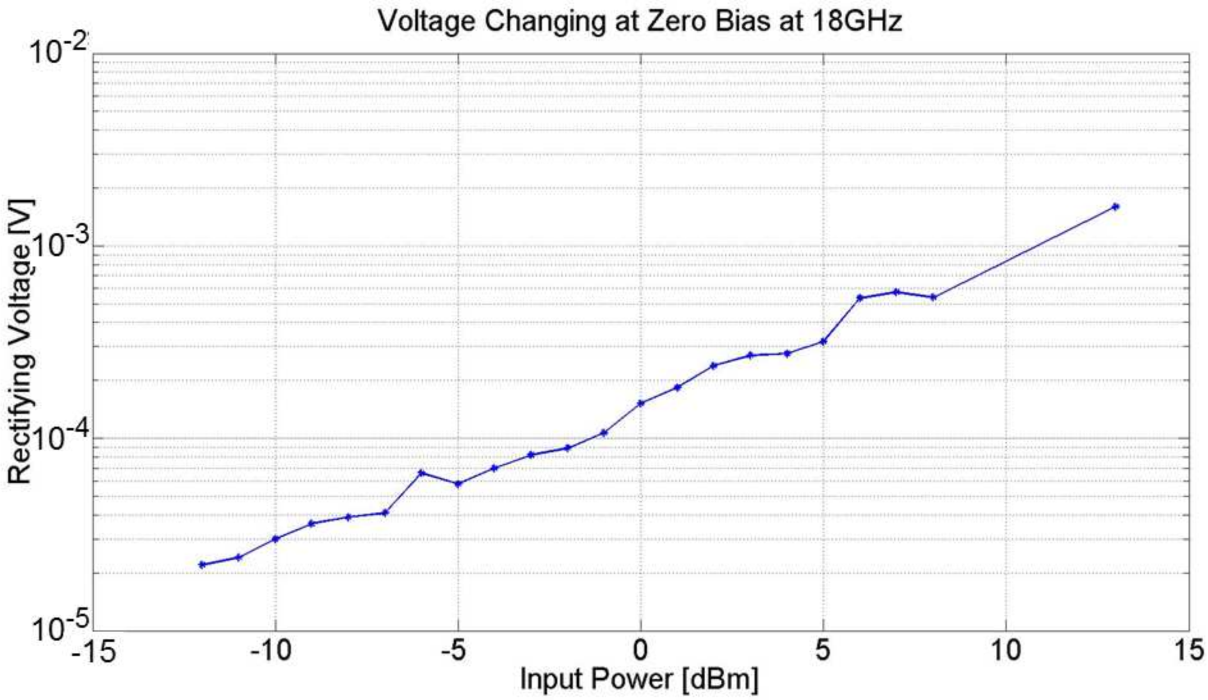

Figure 4.7 Voltage detection vs. Input Power at 18GHz at zero bias

2.2 RF detection with applied DC bias

As discussed earlier, the sensitivity of the diodes will improve at higher bias voltages. This is related to higher non-linearity and also improved impedance matching. Figure 4.8 shows the measured results for a Schottky diode probed using an RF probe at 18 GHz with incident power of 13dB at the probe tip.

A ground-signal (GS) probe was used to in characterizing the detector. A signal generator coupled to the probe through a bias-T was used for the measurement setup. The rectified voltage was measured using the bias-T. Also, the bias was implemented using the bias-T and a

T-connector. A 1MΩ resistor was used in series with the bias supply in order to prevent voltage spiking and also the voltage was measured across this resistor to determine the voltage drop across the diode. To get better and reliable results, high power of 13dBm at a fixed with frequency of 18GHz. Measured results are shown in Figure 4.8

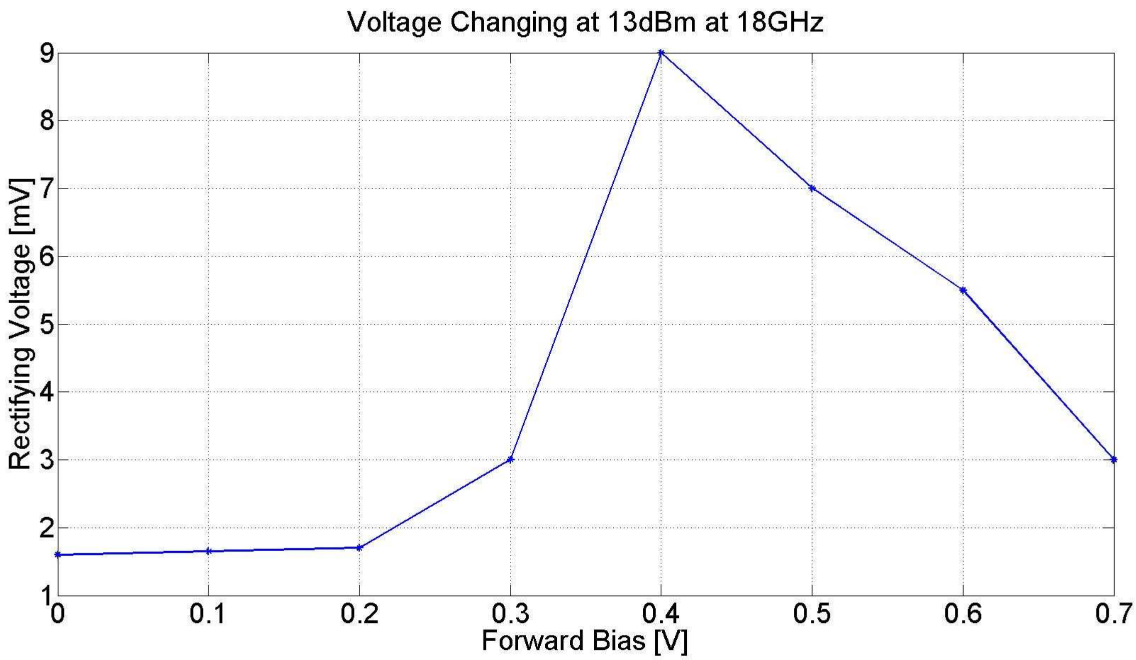

Figure 4.8 Voltage detection vs. applied DC bias at 18GHz with incident power of 13 dBm

It shows that the sensitivity increases as a function of DC bias and is maximum near 0.4 V. Bias voltage above 0.7V was not studied in order to avoid damaging the device. Also, note that the bias voltage of 0.4V where the sensitivity is high is lower than the predicted voltages. This is because under strong RF power, the device is self-basing and thus inducing small voltage across the diode. Thus the effective bias voltage is 0.4V plus the self-biasing voltage.

3. Calculations of Parameters for Sensitivity

3.1 Calculation of NEP and voltage sensitivity at Microwave frequency

After acquiring the voltage detection signal, it is also necessary to obtain the NEP value and voltage sensitivity β_V in order to determine the sensitivity of the device at measured 18GHz and higher frequencies. Based on the equations from 2.3 to 2.7 in chapter 2 and the information such as resistance from the measured I-V curve, sensitivity related parameters could be derived.

One of the critical values to calculate NEP and β_V is the series resistance R_S, which is included in the effective resistance (R_S+R_d) shown in Figure 4.2. This series resistance R_S includes CNT intrinsic resistance R_{CNT} and the junction resistance of Ohmic contact between CNT and Au R_{Ohmic}, and it seldom changes respected to the applied bias. However, the diode resistance effectively decreases as a function of voltage. According to Figure 4.2, at the end of the effective resistance curve, it starts to saturate which also means Schottky junction resistance reaches it minimum, and the resistance value in this region is equals to R_S, which is about 12KΩ. Also, according to the analysis of series resistance in chapter 2, for 1μm (which is also the gap size in the fabricated device) long semiconducting SWNT, R_S=72.9 KΩ, which indicates effectively 6 CNTs are connected between the electrodes (numbers could be more since CNTs have defects and the contact is not perfect). In Chapter 2 it was pointed out that the junction capacitance is around 1aF per CNT, so the total junction capacitance C_j is around 6aF for this device. The ideality factor was calculated previously and is around 5. By using these values in the equations 2.3 to 2.7 as well as the mismatch coefficient equation, NEP and β_V are easily determined. The measurements are also based on 18GHz as preliminary tests. Figure 4.9 shows the calculated NEP and β_V as a function of applied bias without mismatch. Figure 4.10 illustrates the NEP and β_V with mismatch using the above parameters.

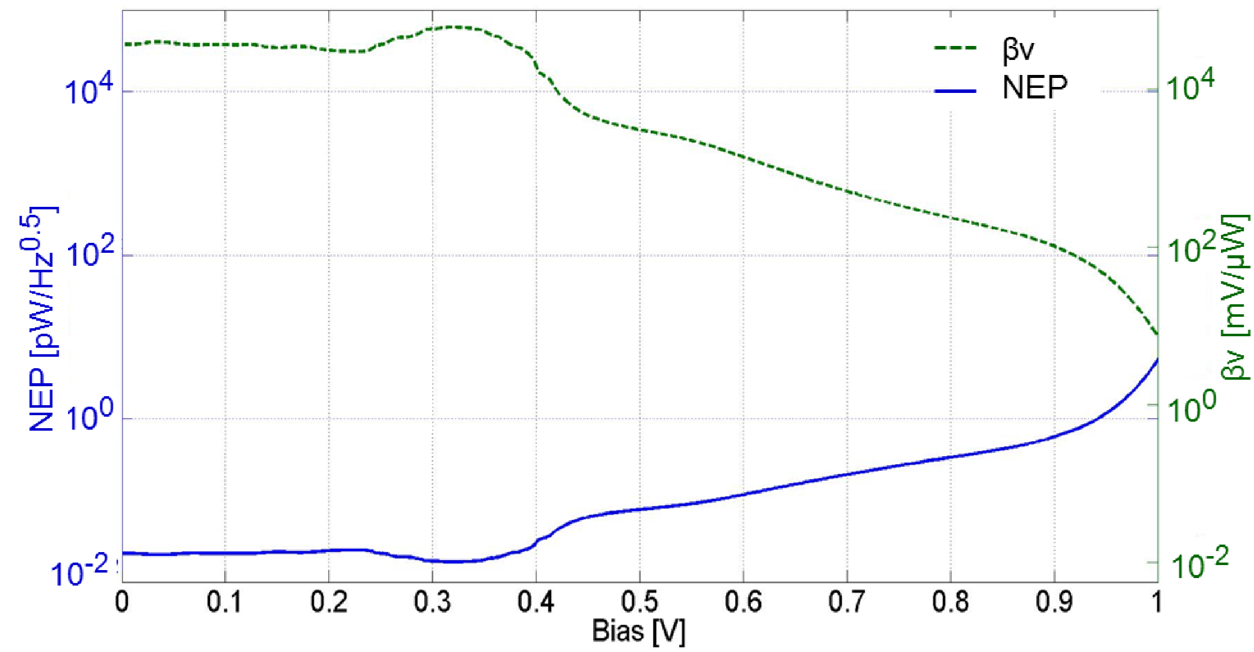

Figure 4.9 NEP and β_V vs. voltage at 18GHz without mismatch

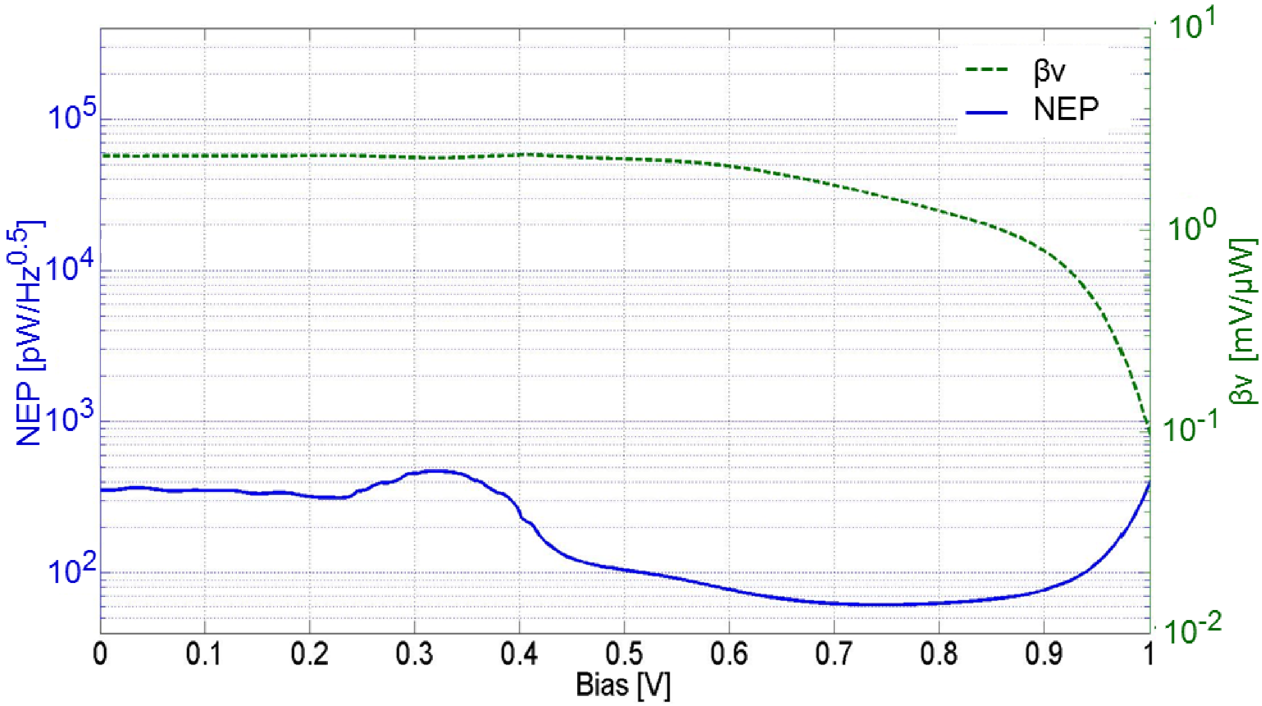

Figure 4.10 NEP and βv vs. voltage at 18GHz under unmatched condition

Figure 4.9 shows that the NEP value is extremely small at lower bias and gradually increases to

8pW/Hz$^{0.5}$ around 1V, and the voltage sensitivity β_V decreases from above 10^4 to 10mV/μW. This shows that a CNT based RF detector can be made using this approach. However, for this device, the impedance mismatch is significantly large due to the high resistance of the CNT devices. The affect of impedance mismatch is incorporated in the calculation of NEP and βv values and this is shown in Figure 4.10. These values are typically what will be measured in an actual system. In Figure 4.10, β_V is smaller in comparison to values in Figure 4.9. It remains stable around 4mV/μW through a wide region of applied bias and then decreases due to less obvious non-linear behavior. The NEP performance first decreases to a certain value at a certain bias, and then increases again. This means that the device has an optimal bias that provides smallest NEP, which is consistent with projections in the simulation chapter. The minimum value of 61.3pW/Hz$^{0.5}$ occurs around 0.75V, at which the bias is greater than having maximum voltage detection in Figure 4.8. This bias lowering occurs due to self-biasing and effective delta shift in bias voltage. The minimum NEP is larger than the simulated results at 1THz. Again, this difference between real device and simulation is due to the dissimilar of the CNTs and the large series resistance which results from CNT defects, imperfect Ohmic contacts and less conductive Ti antenna layer. However, this proves that a good CNT Schottky diode detector can be fabricated by applying novel fabrication process.

3.2 Cut-off frequency and High Frequency Calculations

One of the intrinsic properties of high frequency application for Schottky diode is the cut-off frequency. Once the measured frequency exceeds this value, the carriers at the junction cannot react as fast as the changing of the frequency and the device fails to operate. In other words, the diode capacitance shunts the diode resistance and thus no power drop across the diode non-linear resistor In order to determine the cut-off frequency of the CNT Schottky diode detector, equation 2.5 is used, with the resistance value derived from above analysis, it is plotted in Figure 4.11 as a function of applied bias.

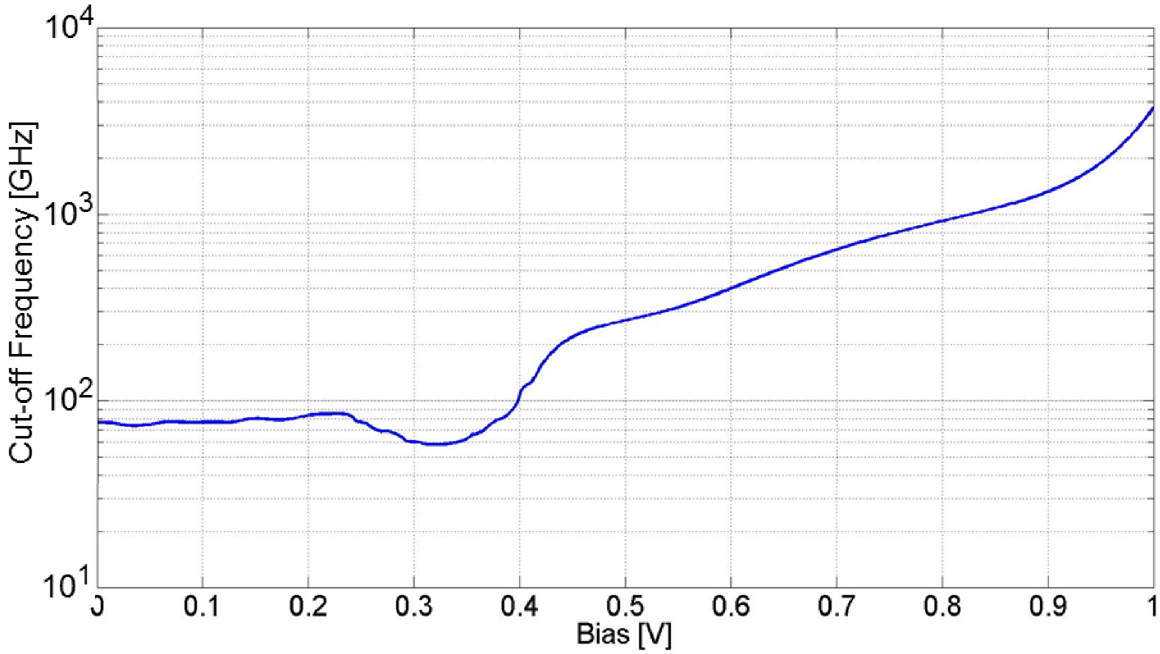

Figure 4.11 Cut-off frequency as a function of applied bias

It is obvious that the cut-off frequency increases with an increase in the bias voltage. This is due to the fact that the junction resistance decreases with increase in bias voltage. Figure 4.11 also shows that at zero bias, the cut-off frequency is only 80GHz. To achieve cut-off frequency of 1THz, the device has to be biased near 0.83V. To increase the cut-off frequency at a certain bias or detect higher frequency at low bias, the device should have more numbers of CNTs connected in parallel. Figure 4.12 plots the NEP value at different detectable frequencies with respect to the applied bias. The frequencies used are also shown in the legend in Figure 4.12. This figure shows the detector works at higher frequencies at higher bias voltages. This is because at low voltages, the cut-off frequency is low. The trend for different frequencies is similar, except limited by the cut-off frequency.

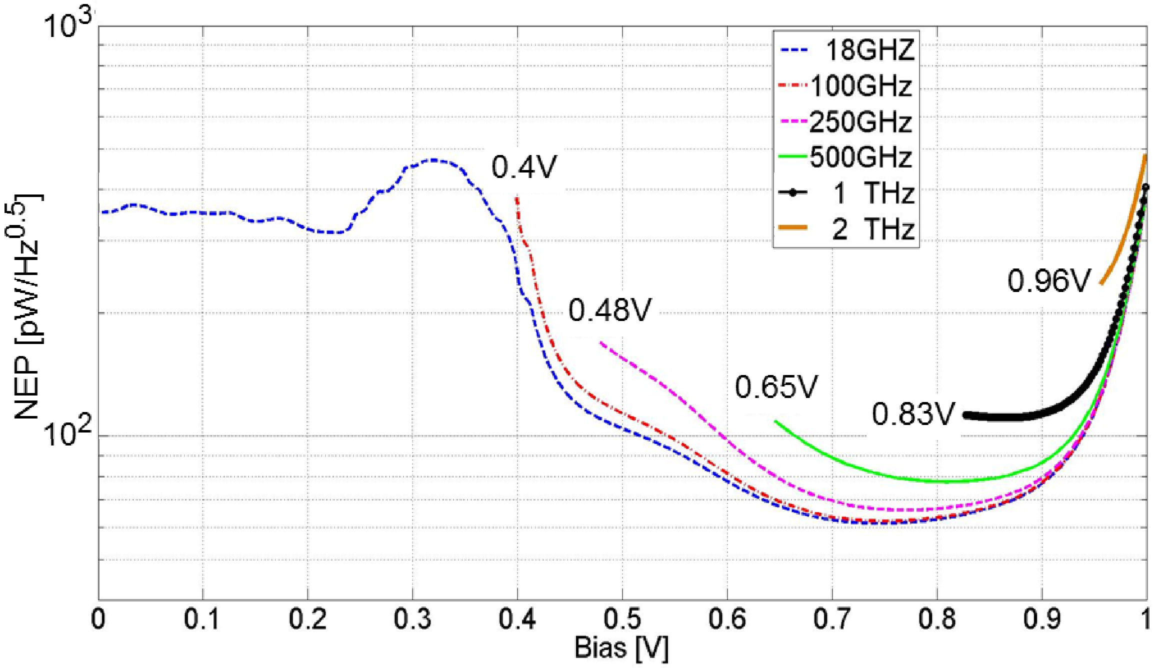

Figure 4.12 NEP vs. bias at different frequencies, the value besides each curve is the minimum voltage required to avoid frequency cut off

The minimum NEP achievable at 18 GHz is 61.3pW/Hz$^{0.5}$, and this value becomes larger for higher frequencies, which means the sensitivity decreases. Again, for detecting 1THz signal, the minimum NEP is 111pW/Hz$^{0.5}$, which is 20 times of that value from simulation. This difference may be due to imperfect contacts and defects in the CNTs which increase the intrinsic resistance, also due to the tunneling current dominance, the ideality factor is 5 which is larger than that used in simulation (n=1.5). Furthermore, the number of CNTs in this measured device may not be optimum. All of these parameters affect the value of NEP. Aligning more semiconducting CNTs is a simpler approach to solve this problem. If increasing up the numbers of CNTs from 6 to 16 by ratio, which was simulated in chapter 2, and reduces tunneling effect at the Schottky diode, which decreasing the ideality factor, the NEP will be 12.5pW/Hz$^{0.5}$, which is closer to 5.5 pW/Hz$^{0.5}$ from the simulation. However, aligning a high density of CNTs in parallel is a challenge. Further studies needs to be carried out to develop a robust aligning process where the concentration of CNTs per device could easily be tailored to desired numbers per device.

Conclusions

In this research, a novel structured CNT Schottky diode THz detector is demonstrated with simulation and fabrication. The designation of the unique fabrication of the device realizes the possibility of manufacturing low cost, larger area detector array with high sensitivity. Comparing with other CNT based and conventional Schottky diode detectors in literatures, it has multi-number semiconducting CNTs parallel connected in the gap, which helps decrease the diode impedance and provides improved impedance matching with the antenna element over a broad frequency range. The detailed simulations considered more critical parameters such as series resistance, flicker noise and mismatch coefficient than other research and shows that with optimal number of CNTs, the minimum noise equivalent power, NEP, which represents the highest sensitivity of the RF detector, has a value around 5.6pW/Hz$^{0.5}$, by applying 16 numbers of CNTs. This value is better than those in some of the literatures and the novel fabrication process elevates this topic to a more promising standing.

This unique fabrication is done on polymer wafer which allows reducing cost but increasing area at the same time. Undercut self-alignment fabrication process for CNT Schottky diode uses conventional microlithography approaches while achieving very small feature size down to hundred nanometers. The avoidance of e-beam lithography helps to realize batch fabrication for larger area but lower cost detector array.

Such a CNT Schottky diode detector was fabricated and characterized at 18 GHz using a coplanar structure. The strong non-linear I-V characteristic indicated such novel fabrication process for CNT Schottky diode was repeatable. It also showed that NEP value of $61.3pW/Hz^{0.5}$ at room temperature can be achieved. At higher frequency such as 1THz, this NEP value is around $111pW/Hz^{0.5}$, which is larger than that of simulation since CNTs are dissimilar with defects and other factors such as contact quality is imperfect. But it is possible to minimize this difference by aligning more semiconducting SWNTs in the gap to further reduce the resistance and provides a better impedance matching to the antenna. The calculation also showed that less than 1 $pW/Hz^{0.5}$ can be reached if the expected impedance matching is achieved, this value would be better than the best THz detector in the literature.

Device optimizing for a better impedance matching and further measurements are being carried out at higher operating frequencies. The results of this research will have significant impact on the development of large area compatible low-cost nano-electronic devices for high frequency applications. Furthermore, the processing approach demonstrated here can be applied in the heterogeneous integration of CNT devices with other semiconductor technologies.

References

References

[1]. http://thz.phys.rpi.edu/about.html

[2]. Kimmitt, M.F., Terahertz research - the first thirty years (1895-1924), Infrared and Millimeter Waves, 2004 and 12th International Conference on Terahertz Electronics, 2004., 27 Sept.-1 Oct. 2004, pp69-70

[3]. P. Mukherjee, B. Gupta, Terahertz (THz) Frequency Sources and Antennas - A Brief Review, Int J Infrared Milli Waves ,2008, 29, pp1091–1102

[4]. Harnessing Terahertz Technology

[5]. AG Davies, EH Linfield and M B Johnston, The development of terahertz sources and their applications, Phys. Med. Biol., 2002, 47, pp3679–3689

[6]. M. Mukherjee, N. Mazumder, S. K. Roy, and K. Goswami, GaN IMPATT Diode: a Photo-Sensitive High Power Terahertz Source, Semiconductor Science and Technology, 2007, 10, 22(12), pp1258–1267

[7]. New T-Ray Source Could Improve Airport Security, Cancer Detection, ScienceDaily (Nov. 27, 2007)

[8]. Peeling adhesive tape emits electromagnetic radiation at terahertz frequencies, www.opticsinfobase.org, 6 August 2009

[9]. Mike Kemp, Terahertz Sensors for Explosives Detection and other Security Applications, SENSORS FOR SECURITY, JRC Ispra, June 2004 pp14-15.

[10]. F. Sizov, A.Rogalski, Review: THz detectors, Progress in Quantum Electronics, 2010, 34, pp278–347

[11]. Paul Muralt, Micromachined infrared detectors based on pyroelectric thin films, Rep. Prog. Phys. ,64 (2001) ,pp1339–1388

[12]. John Byrd, THz Detectors, Accelerator-Based Sources of Coherent Terahertz Radiation – UCSC, Santa Rosa CA, January 21-25, 2008

[13]. Iijima, Sumio, Helical microtubules of graphitic carbon, Nature 354, (7 November 1991) pp56–58

[14]. Graphene oxide gets green, LabSpaces, Friday, July 23, 2010

[15]. Shoushan Fan, Michael G. Chapline, Nathan R. Franklin, Thomas W. Tombler, Alan M. Cassell, and Hongjie Dai, Self-Oriented Regular Arrays of Carbon Nanotubes and Their Field Emission Properties, Science, 1999, 283, pp512-514

[16]. L.X. Zheng, et al., Ultralong Single-wall Carbon Nanotubes Nat. Mater., 2004, 3, pp673-676

[17]. Francois Leonard, The physics of carbon nanotube devices, Library of Congress Cataloging-in-Publication Data, ISBN: 978-0-8155-1573-9

[18]. M. Popov et al., Superhard phase composed of single-wall carbon nanotubes, Phys. Rev. B 65: 033408

[19]. MIT Institute for Soldier Nanotechnologies, http://web.mit.edu/isn/. Retrieved 2010-02-26

[20]. A. Subramanian, L. X. Dong, B. J. Nelson, Batch Fabrication of Carbon Nanotube Bearings, Nanotechnology, 2007, Vol. 18, 075703

[21]. CNTbands simulation at Nanohub, https://nanohub.org/tools/cntbands-ext/

[22]. V. Derycke,, R. Martel,, J. Appenzeller, and, Ph. Avouris, Carbon Nanotube Inter- and Intramolecular Logic Gates, Nano Letters 2001 1 (9), 453-456

[23]. Ali Javey, Qian Wang, Ant Ural, Yiming Li, and Hongjie Dai, Carbon Nanotube Transistor Arrays for Multistage Complementary Logic and Ring Oscillators, Nano Letters, 2002 Vol. 2, No. 9 929-932

[24]. Antonis Andriotis, Madhu Menon and Heather Gibson, Realistic nanotube-metal contact configuration for molecular electronics applications, IEEE Sensors Journal, June 2008,Vol. 8, No. 6,

[25]. Quoc Ngo, et al., Electron Transport through Metal–Multiwall Carbon Nanotube Interfaces, IEEE Transactions On Nanotechnology, June 2004, Vol. 3, No. 2

[26]. Chun Lan, et al., Measurement of metal/carbon nanotube contact resistance by adjusting contact length using laser ablation, Nanotechnology 19 (2008) 125703 (7pp)

[27]. Bin Shan, Kyeongjae Cho, Ab initio study of Schottky barriers at metal-nanotube contacts, Physical Review B, 2004, 70, 233405

[28]. J. J. Palacios, et al., Metal Contacts in Carbon Nanotube Field Effect Transistors: Beyond the Schottky barrier paradigm, Physical Review B, 2008, 77, 113403

[29]. W. Choi, W. Park, E. Bae, D. kang, E. Lee, B. Cheong, J. Ko, "Carbon nanotube for nanoelectronics", IEEE-Nano 2003, August 12-14 2003 SanFrancisco, CA

[30]. Yunsung Woo, Georg S Duesberg and Siegmar Roth, Reduced contact resistance between an individual single-walled carbon nanotube and a metal electrode by a local point annealing, Nanotechnology, 18, 2007, 095203

[31]. http://en.wikipedia.org/wiki/Polymer

[32]. Mark A. Eddings, Michael A. Johnson and Bruce K. Gale, Determining the optimal PDMS–PDMS bonding technique for microfluidic devices, J. Micromech. Microeng., 2008,18 , 067001

[33]. Winnie Wing Yin Chow, et al., Microfluidic channel fabrication by PDMS-interface bonding, Smart Mater. Struct., 2006,15, pp112–116

[34]. Archit B. Sanghvi, Kiley P -H Miller, Angela M. Belcher and Christine E. Schmidt, Biomaterials functionalization using a novel peptide that selectively binds to a conducting polymer, Nature Materials, 2005, 4, pp496 - 502

[35]. J. Hejase, P. Paladhi, and P. Chahal, "Terahertz Characterization of Dielectric Subsrates for Components Design and Non-destructive Evaluation of Packages", IEEE Trans. On Advanced Packaging [in review]

[36]. Harish M. Manohara, et al. Carbon Nanotube Schottky Diodes Using Ti-Schottky and Pt-Ohmic Contacts for High Frequency Applications, Nano Letters, 2005, Vol. 5, No. 7 pp1469-1474

[37]. http://en.wikipedia.org/wiki/Polyethylene_terephthalate, http://en.wikipedia.org/wiki/PEEK, http://en.wikipedia.org/wiki/Polyimide

[38]. Mauricio Terrones, Science and Technology of The Twenty-first Century: Synthesis, Properties, and Applications of Carbon Nanotubes, Annu. Rev. Mater.Res., 2003, 33, pp419–501

[39]. Francois Leonard, The Physics of Carbon Nanotube Devices, William Andrew Inc., 2008

[40]. Philip G. Collins, et al., Extreme Oxygen Sensitivity of Electronic Properties of Carbon

Nanotubes, Science, 2000, 287, 1801

[41].Kyoung-Yong Chun and Cheol Jin Lee, Potassium Doping in the Double-Walled Carbon Nanotubes at Room Temperature, J. Phys. Chem. C 2008, 112, pp4492-4497.

[42].Harish M. Manohara, et al. Carbon Nanotube Schottky Diodes Using Ti-Schottky and Pt-Ohmic Contacts for High Frequency Applications, Nano Letters 2005 Vol. 5, No. 7 pp1469-1474

[43].Samuel Leclercq, Discussion about Noise Equivalent Power and its use for photon noise calculation.2007-03-02

[44].http://optical-technologies.info/?tag=noise-equivalent-power

[45].http://www.its.bldrdoc.gov/fs-1037/fs-1037c.htm

[46].Prem Chahal, Frank Morris, and Gary Frazier, Zero Bias Resonant Tunnel Schottky Contact Diode for Wide-Band Direct Detection, IEEE Electron Device Letters, 2005, Vol. 26, No. 12, pp894-896

[47].Philip G. Collins, M. S. Fuhrer, and A. Zettl, 1/f noise in carbon nanotubes, Applied Physics Letters, 2000, Vol76, No. 7, pp894-896

[48].Yu-Ming Lin, Joerg Appenzeller, Zhihong Chen, Phaedon Avouris, Electrical transport and 1/f noise in semiconducting carbon nanotubes, Physica E, 2007, 37, pp72–77

[49].Noise Tutorial, RF, RFIC, Microwave Theory, Design, http://www.rfic.co.uk

[50].Raychowdhury, A., Roy, K., A circuit model for carbon nanotube interconnects: comparative study with Cu interconnects for scaled technologies, Computer Aided Design, 2004. ICCAD-2004. IEEE/ACM International Conference, pp. 237- 240, 7-11 Nov. 2004

[51].Mark Budnik, Arijit Raychowdhury, Aditya Bansal and Kaushik Roy, A High Density, Carbon Nanotube Capacitor for Decoupling Applications, Automation Conference, 2006 43rd ACM/IEEE, pp.935-938

[52].Joerg Appenzeller (2003), Electronic Transport in Semi-conducting Carbon Nanotube Transistor Devices, http://nanohub.org/resources/147.

[53].Chun Lan, Pornsak Srisungsitthisunti, Placidus B. Amama, Timothy S. Fisher, Xianfan Xu and Ronald G. Reifenberger, Measurement of metal/carbon nanotube contact resistance by

adjusting contact length using laser ablation, Nanotechnology, 2008, 19, 125703

[54]. Enrique Cobas and Michael S. Fuhrer, Microwave Rectification by a Carbon Nanotube Schottky Diode, Appl. Phys. Lett. 93, 2008, 043120

[55]. Yu-Chih Tsenga and Jeffrey Bokor, Characterization of the junction capacitance of metal-semiconductor carbon nanotube Schottky contacts, Applied Physics Letters, 96, 013103

[56]. Manijeh Razeghi, Fundamentals of Solid State Engineering, 2nd Edition, Springer Science+Business Media, Inc. 2006.

[57]. Bart Van Zeghbroeck, Principles of Semiconductor Devices 2004, University of Colorado, Boulder, http://ece-www.colorado.edu/~bart/book/

[58]. S. Roche, et al, A simple drain current model for Schottky-barrier carbon nanotube field effect transistors, Nanotechnology, 2007, 18, 025201

[59]. Peter Stallinga, Theory of electrical characterization of (organic) semiconductors, Universidade do Algarve, http://ceot.ualg.pt/OptoEl/theory/2terminal/

[60]. Karim El Shabrawy, Koushik Maharatna, Darren Bagnall and Bashir Al-Hashimi Modeling SWCNT Band-gap and Effective Mass Variation using a Monte Carlo Approach, Nanotechnology, IEEE Transactions on , vol.9, no.2, pp184-193, March 2010

[61]. Jose M. Marulanda, and Ashok Srivastava, Carrier density and effective mass calculations in carbon nanotubes, phys. stat. sol. (b), 2008, 245, No. 11, pp2558–2562

[62]. J. Appenzeller, M. Radosavljevic, J. Knoch, and Ph. Avouris, TunnelingVersus Thermionic Emission in One-Dimensional Semiconductors, Phys. Rev. Lett., 2004, 92, 048301

[63]. Konstantin Iakoubovskii, Techniques of aligning carbon nanotubes, Cent. Eur. J. Phys., 2009,7(4), pp645-653

[64]. Yongqiang Tan and Daniel E. Resasco, Dispersion of Single-Walled Carbon Nanotubes of Narrow Diameter Distribution, J. Phys. Chem. B, 2005, 109, pp14454-14460

[65]. Subramanian, A.; Vikramaditya, B.; Nelson, B.J.; Bell, D. and Lixin Dong, Dielectrophoretic micro/nanoassembly with microtweezers and nanoelectrodes, Advanced Robotics, 2005. ICAR '05. Proceedings., pp208-215, 18-20 July 2005

[66]. B K Jang, Y Sakka and S K Woo, Alignment of carbon nanotubes by magnetic fields and aqueous dispersion, Journal of Physics: Conference Series, 2009, 156, 012005

[67]. Yeji Kim, Nobutsugu Minami, Weihong Zhu, Said Kazaoui, Reiko Azumi and Mutsuyoshi Matsumoto, Langmuir–Blodgett Films of Single-Wall Carbon Nanotubes: Layer-by-layer Deposition and In-plane Orientation of Tubes, Jpn. J. Appl. Phys., 2003, Vol. 42, pp7629–7634

[68]. Guihua Yu, Anyuan Cao and Charles M. Lieber, Large-area blown bubble films of aligned nanowires and carbon nanotubes, Nature Nanotechnology, 2007, 2, pp372 - 377

[69]. http://en.wikipedia.org/wiki/Dielectrophoresis

[70]. Chunxiang Xu, Yan Wang, Ming Cao, Zuhong Lu, Dielectrophoresis of human red cells in microchips, Electrophoresis 1999, 20, pp1829-1831

[71]. Michael Pycraft Hughes and Kai Friedrich Hoettges, Bacterial Concentration, Separation and Analysis by Dielectrophoresis, Principles of Bacterial Detection: Biosensors, Recognition Receptors and Microsystems, 2008, IV, pp895-907

[72]. Pohl, H. A., 1978. Dielectrophoresis the behavior of neutral matter in nonuniform electric fields. Cambridge University Press. Cambridge

[73]. Didi Xu, Arunkumar Subramanian, Lixin Dong, Shaping Nanoelectrodes for High-Precision Dielectrophoretic Assembly of Carbon Nanotubes, IEEE Transactions On Nanotechnology, Vol. 8, No. 4, July 2009

[74]. K. Fu, R. Zannoni, C. Chan, S. H. Adams, J. Nicholson, E. Polizzi, and K. S. Yngvesson, Terahertz detection in single wall carbon nanotubes, Applied Physics Letters, 2008, 92, 033105

[75]. DuHamel, R. and Ore, F. Logarithmically Periodic Antenna Designs, IRE International Convention Record, pp139 – 151, Mar 1958

[76]. A. Subramanian, B. Vikramaditya, L. X. Dong, D. J. Bell, and B. J. Nelson, Micro and Nanorobotic Assembly Using Dielectrophoresis, Robotics: Science and Systems, 2005, I, pp327-334

[77]. Hongzhi Chen, Ning Xi, King W. C. Lai, Carmen Kar Man Fung and Ruiguo Yang, Development of High Performance Infrared Detector Using Carbon Nanotube Field Effect Transistors, IEEE Transactions on Nanotechnology, 2010, Vol. 9, No. 5, pp582-589

[78]. K. W. C. Lai, N. Xi, and U. C. Wejinya, Automated process for selection of carbon nanotube by electronic property using dielectrophoretic manipulation, J. Micro-Nano Mechatron., 2008, Vol. 4, No. 1–2, pp37–48

[79]. Jingqi Li , Qing Zhang, Dajiang Yang, Jingze Tian, Fabrication of carbon nanotube field effect transistors by AC dielectrophoresis method, Carbon, Vol.42, pp2263–2267

[80]. G. D. J. Smit, S. Rogge, and T. M. Klapwijk, Scaling of nano-Schottky-diodes, Applied Physics Letters, 2002, Vol. 81, No.20, pp 3852-3854

[81]. Chanoh Hwang, Jung-Hwan Hyung, Seung-Yong Lee,Chan-Oh Jang, Tae-Hong Kim, Pyung Choi and Sang-Kwon Lee, The formation and characterization of electrical contacts (Schottky and Ohmic) on gallium nitride nanowires, J. Phys. D: Appl. Phys., 2008, 41,pp105103-105107

[82]. G. D. J. Smit, S. Rogge, and T. M. Klapwijk, Enhanced tunneling across nanometer-scale metal–semiconductor interfaces, Applied Physics Letters, Vol 80, 14, 2002, pp 2568-2570

[83]. S. M. Sze and Kwok K. Ng, Physics of Semiconductor Devices, Third Edition, John Wiley & Sons, Inc., 2007, pp164

[84]. P. J. de Pablo, E. Graugnard, B. Walsh, R. P. Andres, S. Datta, R. Reifenberger, A simple, reliable technique for making electrical contact to multiwalled carbon nanotubes, Applied Physics Letters, 1999, Vol. 74, No.2, pp323-325